DIRECTED TRANSPORT-ENABLED IMPROVED BIOSENSING AND BIOANALYSIS ON PLASMONIC NANOSTRUCTURED SUBSTRATES

A THESIS
SUBMITTED TO THE FACULTY OF
UNIVERSITY OF MINNESOTA
BY

SHAILABH KUMAR

IN PARTIAL FULFILLMENT OF THE REQUIREMENTS
FOR THE DEGREE OF
DOCTOR OF PHILOSOPHY

SANG-HYUN OH, ADVISOR

DECEMBER 2015

Acknowledgements

I would like to thank Prof. Sang-Hyun Oh for his guidance, trust and encouragement, which helped me progress through my doctoral research. Thanks to all the lab members, from whom I have learned a lot. I would specially like to mention Nathan Wittenberg, Hyungsoon Im, Sean Lee, Luke Jordan and Nathan Lindquist for guiding me, when I arrived as a new student in the group. I am thankful to Sudhir Cherukulappurath, Tim Johnson, Lauren Otto, and Jonah Shaver for several collaborative experimental efforts and fruitful discussions. Also sincere thanks to all the other group members I have had a chance to interact with and learn from: Avijit Barik, Jincy Jose, Daehan Yoo, Hyeong-Ryeol Park, Xiaoshu Chen, Yong Sang Ryu, Stephen Olson, Seon Namgung, Daniel Klemme, Daniel Mohr and Christopher Ertsgaard. I wish them the best of luck with their current and future endeavors.

I would like to thank the staff at the Minnesota Nano Center and the characterization facility for their kind assistance. I will also acknowledge Greg Wolken, Prof. Edgar Arriaga, Tao Qu, Prof. Randall Victora, Jasmine Sze, Prof. Joshua Edel, Juliane Junesch and Prof. Andreas Dahlin for various interesting collaborative projects.

To the several friends I made in Minneapolis, thanks for your company and making this city feel like home. I would like to acknowledge Alka, my fiancée for her love and support. Finally, I would like to acknowledge the efforts of my parents, for their love, support and sacrifices which form the basis of my personal and educational progress.

Dedication

This thesis is dedicated to my parents.

Directed transport-enabled improved biosensing and bioanalysis on plasmonic nanostructured substrates

by Shailabh Kumar

Abstract

Analytical sensors are widely useful for advances in drug discovery, disease diagnosis and study of biological systems. Metallic nanostructures can utilize unique optical detection techniques through efficient coupling of light with free electrons in the metal layer. However, the performance of these devices is limited by diffusion-limited transport of molecules to nanoscale sensing sites. In this dissertation, nanostructured biosensing substrates are discussed which can spontaneously direct the flow of molecules in solution directly towards themselves. These devices show improved detection sensitivity, while minimizing the limitations and complexity imposed upon the system. Furthermore, they show an ability to trap biological particles such as organelles and liposomes on the sensor surface, facilitating their on-chip analysis with single particle resolution. The work presented in this dissertation can give rise to novel portable sensing platforms with improved performance and diverse applications.

Table of Contents

List of Figures

List of commonly used abbreviations

4-MP	4-Mercaptopyridine
BZT	Benzenethiol
EOT	Extraordinary Optical Transmission
FIB	Focused Ion Beam
NIL	Nanoimprint Lithography
SAM	Self-Assembled Monolayer
SEM	Scanning Electron Microscopy
SERS	Surface-Enhanced Raman Scattering
SPP	Surface Plasmon Polariton
SPR	Surface Plasmon Resonance

Chapter 1

Introduction

Biosensors are analytical devices that are used to identify, quantify or study the properties of target biomolecules, also referred to as analytes. These devices have seen widespread application in various fields such as drug discovery, disease diagnostics, pathogen detection and environmental monitoring. The presence or properties of target molecules can be revealed through independent use or combined application of various techniques including optical, acoustic, electrochemical and electrical methods. The home pregnancy test kit remains a very popular and successful example of an optical assay, where presence of a pregnancy-induced hormone in the body is indicated by a color change.[1, 2] Alcohol breathalyzer, which detects for presence of alcohol in drivers' breath,[3] and blood glucose sensors, critical for diabetes management,[4] are devices which rely on oxidation of target analytes to generate electrical signal. More recently, next generation sequencing of DNA through nanopores has been realized,[5] which relies on changes in ionic resistance of the solution as different nucleotides are transported through the pore. This has revolutionized the field allowing whole genome sequencing in diverse environments with minimal limitations. Ongoing developments towards manufacturing of inexpensive devices that will allow diagnostics in low-resource settings and integration of biosensors with personal devices such as smartphones allowing personal health monitoring indicate the scope for future progress in this area.

This dissertation focuses on methods to improve the performance and expand the scope of optical biosensors, which rely on interaction of light with analytes to obtain the detection signal. Optical signal can be obtained from analyte molecules in various forms

such as light emission (fluorescence or luminescence) or molecular vibrational information (Raman spectra). Specifically, this dissertation focuses on metallic nanostructured biosensors, containing nanoscale features such as holes or sharp tips fabricated in thin metal films. The significance of using metallic nanostructures as optical sensors is that they can confine electromagnetic fields in extremely tight spots at the metal surface. This uses the principles of plasmonics, which deals with the interaction of electromagnetic fields with free electrons in a metal, and has two important implications. One, when the analyte molecules bind close to the sensor surface, the optical (emission or vibrational) signal can be enhanced by many orders of magnitude improving our detection capabilities. Secondly, even minute changes in the refractive-index close to the metal-surface caused by binding or unbinding of molecules can be measured, by monitoring the spectra of light interacting with the sensor. These measurements can be used to identify these molecules, quantify their amount and study the binding interactions between two molecules of interest after one of them has been coated on the sensor surface. The study of protein-protein binding is a crucial part of drug discovery as many drug molecules have to interact with proteins embedded in cell membranes to reach their biological target and function effectively. In collaboration with scientists at the Mayo clinic, nanohole array biosensors are being used for identification and characterization of proteins (antibodies) which can be used for treatment of Multiple Sclerosis.[6]

One of the major problems suffered by these nanoscale sensors is that a very small proportion of analyte molecules reach the sensing site as their transport is limited

by the random diffusive motion of molecules in solution.[7] This slow and inefficient transport results in waste of analyte molecules and limits the detection abilities of the sensor. Poor device sensitivity can be a problem for disease diagnosis where very low concentrations of biomarkers are exhibited, especially in the early stages. Furthermore, slower binding of analytes lengthens the detection time. New techniques that can direct the delivery of analytes to the sensor surface are therefore needed. Techniques proposed to overcome these limitations include applying a pressure gradient or electric field to create conditions that direct the flow of solution to the most sensitive regions on the device.[8, 9] However, many of these methods require external connections and power supply, which necessitate additional requirements such as solution conductivity limitations thereby preventing widespread application of the setup for biological analysis. This dissertation focuses on platforms where the nanostructures themselves initiate localized trapping and concentration of target molecules. Simple and self-propelling designs for biosensors will result in fewer operational constraints and will in turn encourage integration of technology with a wide variety of biologically or physiologically relevant problems.

Furthermore, integration of fluidic systems with nanostructures can enable controlled assembly of biological particles such as cells, liposomes or organelles on the sensor substrate. Once the particles are trapped, they can be subjected to desired environmental stimulus and be analyzed individually or in parallel using analytical techniques supported by these platforms. Assembly of particles on nanostructured

devices can be also utilized to study the effect of material composition and geometry on bioparticle behavior, revealing details about their function.[10]

The chapters in this dissertation discuss these limitations, novel ideas and devices in detail and have been outlined as follows:

Chapter 2 provides background information about nanostructured plasmonic sensors, current limitations, and the scope for further improvements.

Chapter 3 discusses a method for evaporation-driven directed transport of analytes using nanohole array substrates.

Chapter 4 discusses application of this evaporation-based platform for on-chip assembly and analysis of complex organelles such as mammalian mitochondria with single particle resolution.

Chapter 5 discusses fabrication and application of plasmonic nanohole array substrates which can utilize surface-tension for driving flow of solution towards them.

Chapter 6 discusses the fabrication and application of plasmonic substrates where magnetic forces can be used for directed localization and detection of analytes.

Chapter 7 summarizes the potential impact of techniques presented in this thesis and discusses future applications.

Chapter 2

Background

Analytical biosensors are tools used for detection and analysis of analytes such as disease biomarkers, environmental pollutants, and antibodies. This thesis describes work done to improve the efficacy and performance of a subclass of optical biosensors, known as plasmonic sensors. Optical biosensors in general do not suffer from issues such as sample conductivity requirements or electromagnetic interferences, offer a wide dynamic range and are non-destructive towards the sample. Hence, they can be used for the analysis of wide-range of biological samples and are expected to see widespread application with continued advancements in miniaturization, performance and availability of detectors such as cameras.

2.1 Plasmonic sensors

Conduction electrons in metals are free to move around under the influence of disturbances such as external electromagnetic fields. However the displacement of electrons also results in a balancing force by the fixed positive ions in the metal. This interaction between displacement of electrons and the restoring attractive force can result in collective oscillations of these electrons. These collective oscillations of free electrons are known as plasmons.[11] If all the free electrons in the material are undergoing longitudinal oscillations, they are known as volume plasmons. If the oscillation of electrons is limited to a surface, such as that of a semi-infinite (thin) metal film placed adjacent to a dielectric medium (for example air or water), they are called surface plasmons.[12] Resonant oscillations of these electrons can be created by impinging these materials with photons, provided the momentum of incoming photons matches with the

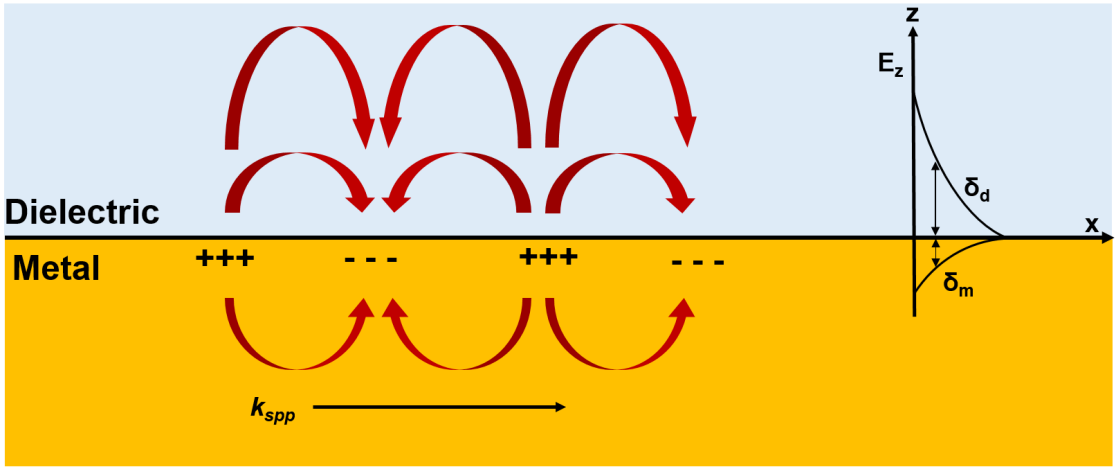

Figure 2.1: Schematic showing a surface plasmon polariton wave propagating along a metal-dielectric interface. The wavevevtor k_{spp} indicates the direction of travelling wave. The exponential decay of electric field intensity E_z away from the metal-dielectric interface is also shown. δ_d and δ_m represent the decay length of the evanescent field into the dielectric and metal respectively.

oscillating electrons. This is known as surface plasmon resonance (SPR) and for flat metal films, results in generation of waves of surface plasmons propagating along the metal surface. These waves created by coupling of surface plasmons with photons are also known as surface plasmon polaritons (SPP) and result in tight confinement of optical (electromagnetic) energy near the metal surface. Propagating SPPs lose energy to the metal by absorption or through scattering into free space. The intensity of the evanescent electric field (E_z) decreases exponentially away from the metal-dielectric interface as shown in Figure 2.1. The decay length (δ) is defined as the distance where the evanescent field intensity is 1/e times that on the surface, and for flat metal films is on the order of 100 nanometers. Hence these SPP waves are extremely sensitive to changes at the metal-dielectric interface and can be applied towards the detection and analysis of molecules

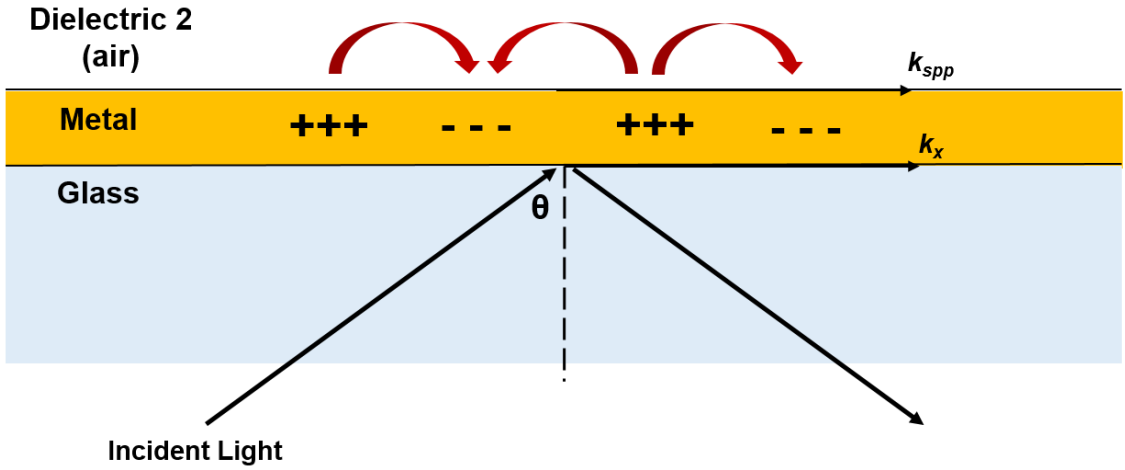

Figure 2.2: Schematic showing a Kretschmann prism-coupling configuration. A thin layer of metal is placed between a glass and a second dielectric layer such as air. Light is incident at an angle through the glass layer or prism and undergoes total internal reflection. Horizontal component of the wave vector of incident light (k_x) can excite surface plasmon polaritons on metal-dielectric 2 interface at certain values of the incidence angle θ. The wave vector k_{spp} indicates the direction of travelling SPP wave.

close to this interface.

As mentioned earlier, the generation of surface plasmon waves requires that momentum of incoming photons match that of oscillating surface plasmons. For flat metal surfaces, it is not possible to achieve this condition using free-space light. Additional steps such as allowing light to pass through a prism before hitting the metal surface, or using grating structures on the metal surface are needed to satisfy momentum-matching conditions. An example of a prism-coupling setup has been shown in Figure 2.2, where a metal layer is sandwiched between two dielectrics, a glass prism and air. In this case, horizontal component of the incident light can match the momentum of surface plasmons oscillating on the interface of metal and second dielectric layer, at

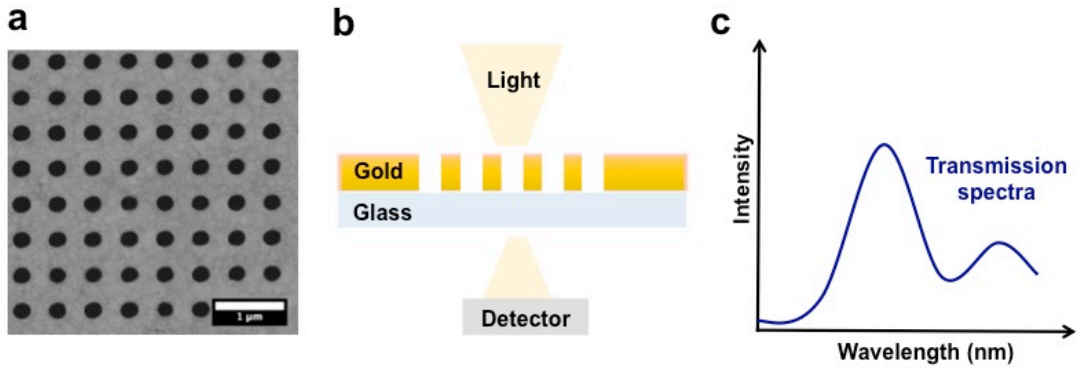

Figure 2.3: Nanohole array-based plasmonic substrates. (a) Scanning electron micrograph (SEM) shows a region on a chip with arrays of nanoholes. Hole diameter is 200 nm and periodicity is 500 nm. (b) Light hitting the nanohole array substrate undergoes extraordinary transmission due to plasmon resonance and generated SPP waves. (c) The collected spectra reflects the wavelengths corresponding to plasmon resonance-mediated enhanced transmission as peaks. This spectra is very sensitive to changes in refractive index near the nanohole array surface.

certain incidence angles. This enables the generation of SPP waves at the interface of metal and dielectric 2, which can be used for sensing of molecules. This setup is known as the Kretschmann configuration and has been extensively used for real-time analysis of protein-protein binding including in commercial instruments such as the Biacore™ system.[13, 14]

Alternatively, gratings on the surface of a flat metal film such as holes, grooves or bumps can be used to modulate the momentum of incoming photons and generate SPPs. Ebbesen and coworkers observed an interesting effect of the generation of surface plasmon waves on nanostructured metallic surfaces in 1998. They reported that transmission of light through an array of subwavelength nanoholes, fabricated in a metal film, was much higher than predicted by classical theory.[15] This effect is now known as

extraordinary optical transmission (EOT) and SPPs excited by periodic array of nanoholes have been found to play a major role in this mechanism.[16, 17] The wavelength at which plasmon resonance occurs can be controlled by changing the periodicity of the nanohole array. A transmission spectra of light passing through the nanoholes is obtained (Figure 2.3), which due to its dependence on surface plasmons, is extremely sensitive to the refractive index close to the metal-dielectric interface. This property of this setup can be utilized for biomolecular sensing.

Another example of plasmonic sensors are nanoparticles, where the metal is in the shape of a small sphere surrounded by air or water, and the electron oscillations are known as localized surface plasmons. Resonant excitement of these plasmons by photons is named as localized surface plasmon resonance (LSPR). Noble metal-coated nanoparticles have been used for in-vitro as well as in-vivo plasmonic sensing and therapeutic applications.[18] In case of LSPR the evanescent electromagnetic field is more tightly confined to the metal surface, with decay length on the order of 10 nm as compared to ~100 nm for SPR wave-based detection systems.

2.2 SPR-based refractive index sensing

SPR-based refractometric sensing relies on detection of change in the refractive index close to the metal-dielectric interface upon binding or unbinding of molecules.[19] The surface of the sensors are generally coated with a layer of receptors such as antibodies. Analytes such as antigens are then introduced in the sensor environment, allowing them to interact with surface-bound receptors. The change in local refractive-

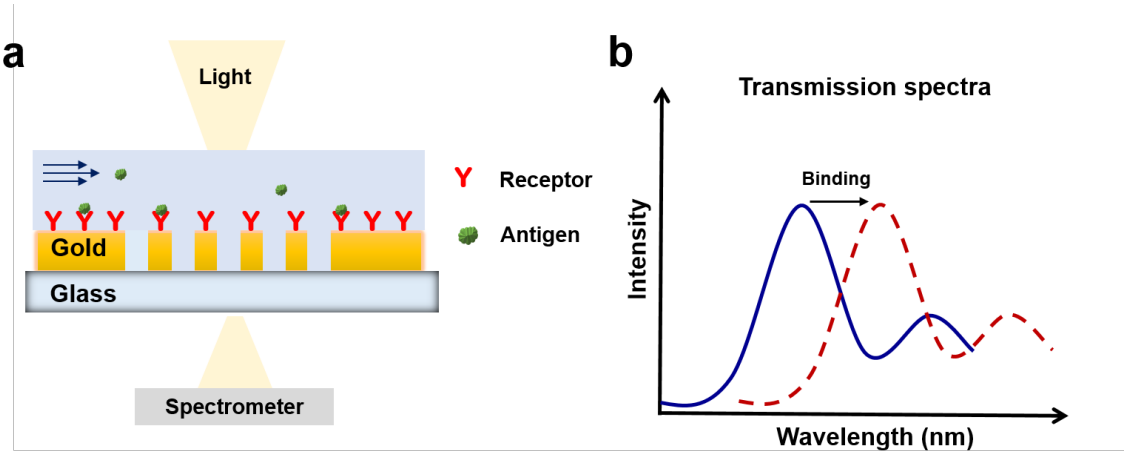

Figure 2.4: Nanohole array-based SPR sensing. (a) Schematic showing receptor-coated nanohole array chip coupled with target molecules flowing in a microfluidic channel. (b) Binding of molecules is reflected as red-shift in the transmission spectra.

index is directly related to the number of molecules close to the metal-dielectric interface. The resultant shift in the wavelength of resonance can be observed by monitoring the spectra of transmitted or reflected light. The shift in spectra can be tracked continuously to obtain real-time binding kinetics information. Importantly, the molecules do not need any additions labels such as fluorescent tags for their detection. This is significant because added labels can affect the native response of the molecules. Since SPR-based sensing can provide high sensitivity, label-free detection and real-time measurements, they are used as gold standard for analyzing complex biomolecular interactions, critical for areas such as drug discovery and clinical diagnosis.

Prism-coupling-based Kretschmann setup has been the most widely used and commercially successful platform for SPR-based refractive index sensing. However, these prism-based setups are extremely bulky and difficult to align. They are also very

expensive (>$250,000) and allow limited number of experiments to be performed simultaneously. Metallic nanoparticles exhibiting LSPR can be used for plasmonic sensing as well.[18] The electromagnetic field is much more tightly confined to the metal surface in this case, with decay length on the order of 10 nm as compared to ~100 nm for other SPR wave-based detection systems. This allows very sensitive detection of analytes near the surface with zeptomolar detection being reported in the past.[20] A significant drawback is that events happening further from the surface including binding of large molecules or multiple layers cannot be easily monitored.

An alternative strategy is to use metallic nanostructured substrates such as nanohole arrays, which facilitate low-cost, simple optical alignment, smaller footprint and multiplexed strategies for SPR-based refractometric biosensing. Substrates such as nanohole arrays in metal films can be simply placed under a microscope with no need for sophisticated alignment (Figure 2.4). An optical fiber connected to a spectrometer placed under the substrate is sufficient to monitor the transmission spectra. The size of the sensor can be user-defined, by fabricating an array of desired size. Furthermore, this platform can be easily combined with microfluidic channels for control over the number of samples to be analyzed at the same time. These several advantages promote nanostructured metallic substrates as a promising tool for on-chip detection of molecular binding.

2.3 Surface-enhanced Raman spectroscopy

In 1928, *Sir* C. V. Raman, together with K. S. Krishnan reported the inelastic scattering of light by molecules.[21] In this process, molecules are excited to a higher energy state by incoming photons. Relaxation of a molecule back to its lower energy state is accompanied by release of a scattered photon, with energy equal to the difference between the two states (Figure 2.5). If the scattered photon has the same energy as the incident photon, this is an elastic process and is called Rayleigh scattering. For inelastic scattering, the released photon can have a lower (Stokes scattering) or higher (Anti Stokes scattering) energy as compared to the incident photon. The change in energy and hence the frequency of inelastically scattered photons is dependent on the vibrational and rotational motion of the molecules being interrogated. Hence, this technique provides a basis for "fingerprinting" of molecules. The collective distribution of inelastically scattered photons from a molecule is identified as its Raman spectra.[21] However, Raman signals are generally very weak with only a small fraction of photons (1 in 10^6) hitting the molecules undergoing inelastic scattering. This makes detection extremely difficult requiring high-power laser sources and concentrated molecular samples.

Enhancement of Raman signal using rough silver electrodes was first noted in 1974 by Fleischmann *et al.*[22] Initially this enhancement was believed to be due to the increased surface area of the electrodes and thus increased molecular concentration. Alternative theories for this enhancement were put forward by Jeanmaire and Van Duyne (electromagnetic enhancement theory) and independently by Albrecht and Creighton (chemical enhancement theory) in 1977.[23, 24] This phenomena is known as

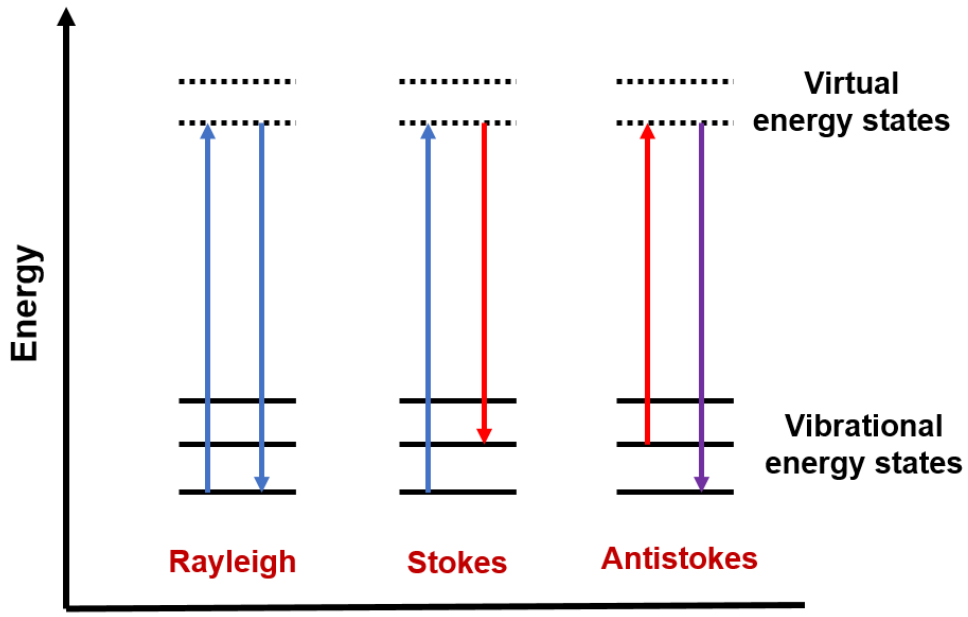

Figure 2.5: Raman scattering demonstrated by an energy-level diagram. Molecules are raised to virtual energy states upon interaction with an incident photon. Relaxation of molecules to their ground state is accompanied by release of a scattered photon.

surface-enhanced Raman scattering (SERS). Chemical enhancement of Raman signal is attributed to charge transfers between the metal and chemisorbed species, with proposed signal enhancement of 10-100 times, and is applicable in specific cases.[25, 26] Electromagnetic enhancement is much stronger (10^4-10^8 times) and is attributed to enhancement of electromagnetic fields near the metal surface by surface plasmons. Incident as well as scattered fields are enhanced, hence the SERS signal is proportional to square of electromagnetic field intensity at the sensing site and the fourth power of field enhancement. These regions with enhanced electromagnetic fields are called plasmonic "hotspots", where the detection is most sensitive.

There is a continued push towards development and application of novel SERS substrates capable of sensing and analysis with high sensitivity in complicated systems. Metallic nanoparticles which exhibit LSPR have been shown to be extremely efficient SERS substrates capable of single molecule detection.[27] These nanoparticles can be easily prepared and applied for in-vivo as well as in vitro sensing of small molecules, nucleic acids and proteins.[28] However the hotspots are randomly distributed which prevents reproducible detection. In order to facilitate better controlled and reproducible SERS sensing, various nanostructured substrates have been engineered including silver-coated nanospheres,[29] triangular nanoparticles,[30] metallic tips,[31] nanogaps,[32] and nanohole arrays.[33] These substrates aim for reproducible and intense enhancement of electromagnetic fields as well as efficient integration with the sample environment for effective detection. SERS-based platforms are now being applied towards various biomedical applications such as glucose monitoring for diabetes management and biomarker identification for kidney disease.[34, 35] With improved fabrication of substrates with reproducible field enhancement and availability of miniaturized, portable detectors, SERS can realize its true potential with several important biomedical applications.

2.4 Overcoming diffusion-limited analyte transport

The development of nanoscale sensors aims to improve the detection sensitivity through features such as enhancement of signal-to-noise. For plasmonic sensors this is achieved by confining the electromagnetic field near detection hotspots, which are nanoscale in dimension and can increase the signal by many orders of magnitude.

However reduction in sensor size is accompanied by a major limitation in the form of slow analyte binding and detection. A very small proportion of analyte molecules actually reach the sensor surface, and even fewer reach the nanoscale plasmonic hotspots. This is specially a problem when the number of analyte molecules in solution is very low (Figure 2.6). Sheehan and Whitman argued that sub-picomolar detection using nanoscale sensors under diffusion-limited conditions would require unrealistically long times (hours to days).[7] Diffusion-limited binding of analytes to the sensor surface can result in waste of expensive analyte, inaccurate kinetics and inefficient detection of disease biomarkers.[7, 36] Hence nanoscale sensors need to be accompanied with mechanisms guiding the transport of molecules to the sensing regions.

Sensing platforms are often combined with microfluidic technology that allows users to control the flow rate of analytes in a channel to monitor the binding events at the sensor surface. This convective flow can help maintain supply of analytes to the sensor surface to facilitate interaction of the analyte and receptor molecules. However, it has been argued that the convective flow over the sensor has limited benefits due to the formation of a depletion zone near the sensing site.[7, 36] Operating the device at a higher flow rate can help improve the analyte transport but the improvements are marginal as faster flow provides the analytes little time to stream past and interact with the receptors. This also leads to wastage of often expensive and difficult to extract analyte molecules. Hence techniques that can improve upon the performance of microfluidic convective flow over the sensors have been proposed.

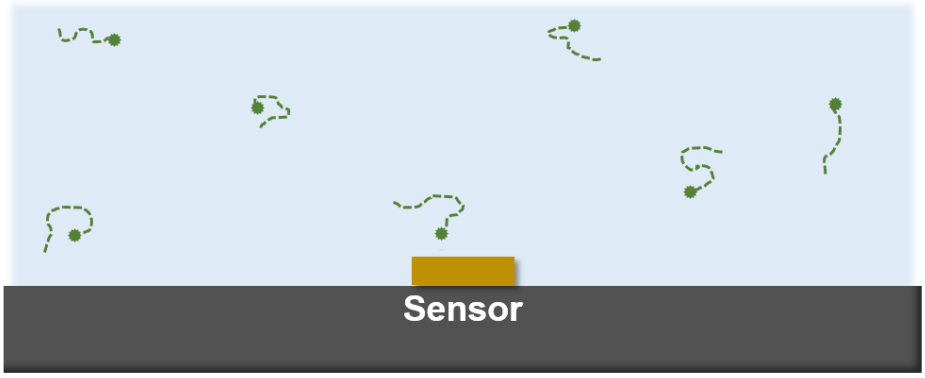

Figure 2.6: Diffusion-limited binding of analytes. Random thermal motion of analyte molecules limits sensor sensitivity, increasing detection time and sample consumption.

A pressure-driven flow through scheme was used, where the analyte solution was forced through metallic nanohole arrays milled in thin nitride membranes.[8, 37] As molecules flow through the confined space of the nanochannels, diffusion becomes efficient enough for them to interact with the nanohole sidewalls. This increases the chance of molecules binding to the sidewalls either through physical adsorption or chemical linkages if the surface is coated with a receptor for target molecules. This process showed a six-fold improvement in adsorption kinetics as compared to traditionally used microfluidic flow-over technique.[8] The pressure driven flow method is efficient in principle but forcing aqueous flow through nanochannels fabricated in thin hanging membranes leads to operational problems including sophisticated chip assembly to prevent leakage under high-pressure, destruction of the nitride membrane and fluctuation of optical signal.

Electric fields have also been used to preconcentrate the analytes for increased

sensitivity.[38, 39] Metallic nanostructures, which can act as electrodes, generate strong electric field gradients under an applied potential due to the existence of nanoscale variation in their spatial features. This property of nanostructures has been used for electric field gradient focusing, where charged species are concentrated near the electrodes, prior to detection.[9] Dielectrophoresis has also been used to assemble and concentrate target molecules at nanostructured sensing locations.[40] Dielectrophoresis does not require particles to be charged and they can be selectively trapped or repelled based on their size and dielectric properties. Practical applications of techniques such as dielectrophoresis for biomedical sensing remain difficult, since their operation is limited to solutions with low conductance. This is not realistic for fluids such as blood, urine or even buffer. Resistive heating of the solution is another barrier that needs to be overcome for electric field-driven techniques.

In this respect, "cold trapping" techniques, which are not associated with any in-process heating and can be used with complex biological fluids can be more useful. Platforms that can drive the concentration of molecules at the sensing site through directed passive flow or magnetic force-driven transport are therefore very relevant. Magnetic force-directed trapping is a technique, which provides fast capture, specificity and can act irrespective of the direction of bulk fluid flow. Target molecules can be captured by receptor-tagged magnetic particles, which are then collected using an external magnet. Concentration, separation and alignment of molecules as well as larger particles has been practiced using this strategy.[41-43] For miniaturized systems, the

challenge is to combine this method with nanostructures enabling more efficient on-chip concentration and simultaneous sensing. The work presented in this thesis focuses on nanostructure-based sensing platforms, which promote miniaturization and directed transport-driven increased sensitivity for improved detection, as well as ease-of-application in diverse environments for analysis of complex biological samples.

2.5 Bioparticle assembly and analysis

Trapping of molecules or particles at desired locations facilitates controlled interrogation over longer experimental time scales, improving the depth and breadth of information obtained. Use of infrared lasers for optical trapping and manipulation of biological particles with no damage was reported in 1987.[44] The optical force required for trapping is limited by the laser power source and diffraction-dependent focusing of the beam. As the size of particles decreases, the trapping force required for overcoming thermal energy of the particles increases. Confinement of light below the diffraction limit by photonic and plasmonic nanostructures has recently enabled trapping and observation of DNA and single protein molecules.[45]

While nanostructure-aided advances in optical trapping have benefited the behavioral analysis of single particles, platforms that can test multiple components of complex samples simultaneously are needed for high-throughput analysis. Microarray analysis has been widely used for study of DNA,[46] proteins,[47] carbohydrates[48] and cells[49, 50]. The success of microarrays has even led to interest in development of nanoarrays aiming for even higher spatial density of molecules.[51-53] Dip-pen nanolithography

technique was developed as a method to create protein nanoarrays.[54] A squeegee-based facile assembly technique has been demonstrated to arrange naturally occurring cell membranes into arrays for high throughput analysis.[55] These reports indicate that there is a continued interest in array-based studies of biological samples for their rapid and high-throughput analysis on-chip.

Biological particles like cells, liposomes or viruses trapped at a sensor surface can be utilized in combination with label-free techniques like SPR and SERS for diagnostics, analysis of structural changes, or binding events at the surface.[56] Binding interactions and cellular transport happening at the surface of cell membranes via membrane proteins control cellular signaling, behavior and function. About fifty percent of best-selling drugs target membrane proteins.[57] The traditional route of studying membrane protein interactions involves the purification and reconstitution of these proteins in liposomes or model lipid bilayers. Transmembrane proteins face the risk of denaturation while going through the removal and reconstitution process, which can be avoided by using natural membranes directly. A technique was shown for the transfer of native membrane sheets to nanopore arrays directly, for the study of ligand-receptor interactions using optical, electrical and scanning probe-techniques.[58] More recently a plasmonic nanohole array-based system has been used for capturing and profiling exosomes, that are phospholipid nanovesicles secreted by mammalian cells, for cancer diagnostics.[59] These secreted exosomes display membrane-bound proteins that can be traced back to their cellular origin. Existence of specific markers in the exosome membrane signals the presence of

cancer cells in the body. Nanohole array systems have also been used for the specific capture of viruses for their detection in complex biofluids.[60] The influence of nanoscale geometry on binding kinetics has also been utilized for localized trapping and detection of virus-like particles with increased spatial resolution.[61] These recent results show that plasmonic nanostructured substrates have tremendous potential for on-chip trapping and analysis of bioparticles with relevance in diagnostics as well as understanding of cell behavior.

The upcoming chapters will discuss nanostructured platforms with integrated directed transport for sensitive optical detection of molecules as well as on-chip trapping and analysis of biological particles.

Chapter 3

Evaporation-driven flow towards plasmonic nanoholes

Adapted from Kumar, S., Wittenberg, N. J., and Oh, S.-H. (2012). Nanopore-induced spontaneous concentration for optofluidic sensing and particle assembly. *Analytical chemistry*, 85(2), 971-977.

This chapter presents an evaporation-based technique to generate flow of analytes or particles towards nanostructured plasmonic sensors. Localized flow was obtained just by addition of aqueous droplet on the sensor, promoting concentration of proteins as well as assembly of larger liposomes and particles. This platform was used for sensitive optical detection of molecules using fluorescence as well as SPR-based refractive index sensing.

3.1 Introduction

The emerging field of optofluidics has facilitated on-chip integration of micro- and nanofluidics with optical sensing and manipulation techniques for a wide variety of applications.[1-3] The analytical tools mainly utilized by these optofluidic platforms have been fluorescence detection, SPR, and SERS, which are often combined with trapping and manipulation of biomolecules and small particles.[4-8] The potential advantages offered by optofluidic platforms include reduced sample consumption as well as improved sensitivity and detection time. However, demonstrating such benefits using highly miniaturized sensors has been challenging. In micro- and nanoscale sensors, diffusion-limited binding of low-concentration analytes to the sensing surface results in reduced sensitivity, prolonged detection time, artifacts in measured binding kinetics and excessive analyte consumption.[9,10] Thus new techniques to enhance targeted delivery of analytes beyond the conventional diffusion limit are needed. Likewise, rapid transport and site-specific trapping of particles such as beads, liposomes, or cells is also highly desirable, as it facilitates interrogation of complex biological molecules and structures over long

experimental time scales, improving the depth and breadth of information obtainable.[11] Cells or liposomes trapped on a pre-defined sensing surface can also be utilized for label-free analysis of ligands interacting with membrane receptors, which are important targets for drug discovery.[12]

Among various optofluidic systems, metallic nanohole arrays have been widely investigated for optical biosensing and spectroscopy[13-26] because extraordinary optical transmission (EOT) through nanohole arrays[27] can be exploited to develop SPR biosensors, which can detect changes in the interfacial refractive index imparted by analyte binding in a real-time label-free manner. While dead-ended nanohole arrays were initially used, subsequent development of open-ended nanohole arrays in a free-standing, gold-coated silicon nitride (Si_3N_4) membrane enabled "flow-through" plasmonic sensing to address mass transport limitations.[21,23,24] Solid-state nanopores have also been useful in DNA sequencing[28] and single-molecule spectroscopy.[29,30] In such open-ended nanopore systems, samples are typically injected through the nanopores using pressure-driven flow,[21,23] electrokinetic flow[31] or electric field gradient focusing.[32] These methods require external sources for generating pressure gradients, which can often damage the fragile membrane, or a bulky external power supply for creating an electric field.

The work presented in this chapter shows that such external driving mechanisms are not required at all for small-volume concentration of molecules or particle trapping, since each nanopore in the metallic membrane can act as a nano-capillary and has an intrinsic ability to induce trans-nanopore solution flow. Techniques based on capillary

flow have shown potential in generating passive flow and improving the sensitivity of assays.[6,33-36] This chapter demonstrates methods to harness such effects in engineered metallic nanopores for small-volume concentration and integrated optical detection, enabled by metallic nanopore arrays simply acting as passive "nano-drains" without external pumps. Moreover, because there is no need for microfluidic interconnects, the system operates with zero dead volume, which drastically reduces sample consumption. This simple technique also helps prevent damage to the thin suspended nanopore membrane. Working on the principles of capillary flow and evaporation, this approach leads to rapid accumulation and local concentration, which enables arraying and analysis of proteins, polymer and silica beads, as well as phospholipid vesicles.

3. 2 Methods

3.2.1 Nanopore array fabrication

Low-pressure chemical vapor deposition (LPCVD) was used to coat low-stress Si_3N_4 films (100 nm) on both sides of silicon wafers. Photolithography and anisotropic Si etching with potassium hydroxide (KOH) created freely suspended Si_3N_4 membranes. Electron-beam evaporation was used to deposit a 200 nm-thick gold layer on the nitride surface, along with a 5 nm-thick Cr adhesion layer. Holes were milled through the suspended gold/nitride stack using a focused ion beam (FIB). For binding experiments, atomic layer deposition (ALD) was used to conformally deposit a 10 nm-thick silica layer on the chips. Additional fabrication details were described by Im *et al*.[22]

3.2.2 Sample injection

During the experiments, the nanopore sensor chip was supported by glass slides, which acted as spacers. The chip was placed with the flat surface (*trans* side) facing down. A 1–10 μL drop of solution containing particles or streptavidin R-phycoerythrin conjugate (SAPE) was placed on the *cis* side of the chip directly over a single reservoir. The sample was left undisturbed for 5 to 10 minutes and then covered with a cover slip for imaging.

3.2.3 Phospholipid vesicle preparation

Vesicles were formed by rehydration of dried lipids. Solutions of lipids in chloroform were obtained from Avanti polar lipids. These solutions were dried in a desiccator for at least 3 hours. Dried lipids were then rehydrated with 0.1 M NaCl overnight at a final concentration of 0.1 mg/ml. The lipid mixture contained 99% (w/w) Egg-PC (Phosphatidylcholine) and 1% (w/w) 1,2-dimyristoyl-sn-glycero-3-phosphoethanolamine-N-(lissamine rhodamine B sulfonyl, ammonium salt (Rho-PE) as a fluorescent component. After rehydration, the vesicles were vortex mixed for 30 seconds and sonicated for 10 minutes in a room temperature water bath. The vesicles were then extruded through a polycarbonate filter (100 nm) to obtain approximately 100 nm-diameter vesicles. For recording the time-lapse movie, 10 μL of vesicle solution was added to the chip and a coverslip was placed on top. Images were recorded at an interval of 5 seconds with an acquisition time of 1 second.

3.2.4 Fluidic self-assembly of beads on nanopore arrays

Silica and polystyrene beads were used to observe and confirm the generic and size-independent nature of the nanopore-induced fluidic self-assembly process. Silica beads (mean diameter: 700 nm) and fluorescent polystyrene beads – poly (Styrene/2%DiVinylBenzene/Vinyl-COOH), mean diameter 2.19 μm, were obtained from Bangs Labs and used at a final concentration of 10^7 beads/mL in deionized (DI) water. For the experiment with silica beads, 5 μL of solution was placed on back of a single reservoir for 5 minutes and the remaining solution was rinsed off. Four arrays (16 μm x 16 μm) with a 600 nm pore diameter and 1 μm periodicity were used. The sample was then dried to record images with a scanning electron microscope. For polystyrene beads, 10 μL of solution was placed on back of a reservoir for 10 minutes and imaged in solution. Two arrays were milled on the suspended membrane. The larger array (32 μm x 32 μm) had a 2 μm periodicity and 1.2 μm pore diameter, whereas the smaller one (16 μm x 16 μm) had a 1 μm periodicity and 600 nm pore diameter.

3.2.5 SAPE and silane-PEG-biotin binding assay

Streptavidin R-phycoerythrin conjugate (SAPE, mol. wt. 292.8 kD) was obtained from Invitrogen and was diluted in PBS to the desired concentration. Silane-Polyethylene glycol (PEG)-biotin was obtained from NanoCS Inc. Silane-PEG-biotin was diluted in distilled water to make a 1 mM solution. The nanopore array chips with silica layer were left submersed in the solution overnight to form a biotinylated self-assembled monolayer on the surface. The chips were then gently rinsed to remove excess biotin from the

sample surface by submersing in distilled water for 5 minutes. This step was repeated thrice with fresh DI water.

For SAPE binding, 10 µL of sample solution was added to a reservoir and left for 10 minutes. A cover slip was placed on the backside of the chip and it was placed on a glass slide to be quickly imaged. The chip was then gently rinsed by submersing in fresh DI water for 5 minutes. This step was repeated thrice with fresh DI water to remove unbound SAPE before fluorescence imaging of the sensor chip.

3.2.6 Label-free SPR detection

For SPR sensing, nanopore chips with a gold layer deposited on the *cis* side were used. The suspended nitride area had 4 nanopore arrays, two (16 µm x 16 µm) and two (8 µm x 8 µm), each with nanopore diameter 200 nm and period 500 nm. A monolayer of silane-PEG-biotin was formed on the chips after silica coating, as mentioned above. Optical transmission spectra through the nanopores were measured in phosphate buffered saline (PBS) before addition of SAPE. 10 µL SAPE solution was added to the chip and left undisturbed for 10 minutes. This solution was then replaced with fresh PBS thrice to remove unbound SAPE molecules. Spectra through the nanopore arrays were measured again and used to calculate the shift caused by binding of SAPE.

3.2.7 Choleratoxin binding assay

For preparation of phospholipid vesicles containing ganglioside functional group, vesicles were prepared as stated but with 1% (w/w) GM1 and extruded to 200 nm. For

formation of a vesicle array, 5 µL of 0.1 mg/mL vesicle solution was placed over a single reservoir for 5 minutes. The *cis* side of the sample was rinsed with PBS to wash off excess solution and then blocked against nonspecific binding by adding bovine serum albumin (BSA; 2 mg/mL). The setup was left undisturbed for 30 minutes. The chip was rinsed with PBS to wash off excess BSA and 50 nM choleratoxin (CTX) was added to the *cis* side of the chip. Again the chip was left undisturbed for 30 minutes to allow the CTX to bind with GM1. The chip was washed with PBS again to remove unbound CTX. An upright microscope was used to capture fluorescence images through the *trans* side of the chip.

3.2.8 Microscope and software

The images and optical transmission spectra were recorded using a Nikon Eclipse LV 100 upright microscope and a 50× objective. In the SPR experiments, a MATLAB™ script was used which fits a second-order polynomial function around the measured peaks and calculates their centroid. This script is used to track the shift of the desired peak. Photometrics CoolSNAP HQ2 CCD was used in combination with Voodoo software to record the images. ImageJ software was used for analysis and coloring of the images. Data plots were prepared using GraphPad Prism version 5.04. (GraphPad Software, Inc.)

3.3 Results and discussion

The chip design and schematic of action are shown in Figure 3.1. A 1 inch × 1 inch chip containing 9 sensing areas was fabricated in a silicon wafer by

photolithography and anisotropic etching with KOH (Figure 3.1a). The visible openings form a truncated pyramid reservoir with sides of ~1 mm which converge to a suspended Si_3N_4 area with sides of approximately 150 μm (Figure 3.1b). For clarity, the surface of the chip with visible reservoir openings is referred to as the *cis* side and the opposite surface as the *trans* side. A single chip contains 16 sensing areas, each of which can be used independently. A 200 nm gold layer was deposited on the Si_3N_4 film to make the platform amenable to analytical techniques such as SPR,[22] SERS,[37] and electrochemistry.[38] Figure 3.1c shows the suspended nitride area with 4 arrays milled using FIB. Scanning electron micrograph (SEM) of an array is shown in Figure 3.1d. The schematic (Figure 3.1e) shows a single drop of solution (1-10 μL in volume) placed on a single etched reservoir leading to nitride and gold layers with milled nanopore arrays. Figure 3.1f demonstrates the proposed passive convection mechanism for local concentration and assembly of particles at the nanopore array site. Evaporation of solution through the open end of the nanopores from the *trans* side of the chip can act as can act as a passive pump to drive flow of solution towards the nanopores. The spontaneous flow of liquid towards the nanopore arrays directs particle migration and accumulation at the array site. Any loss of solution volume in the chamber due to evaporation and fluid flow also concentrates the particles and brings them closer to the nanopore arrays. Once the particles are close to the nanopore arrays, convection directs them to the array region where they are trapped (Figure 3.1f).

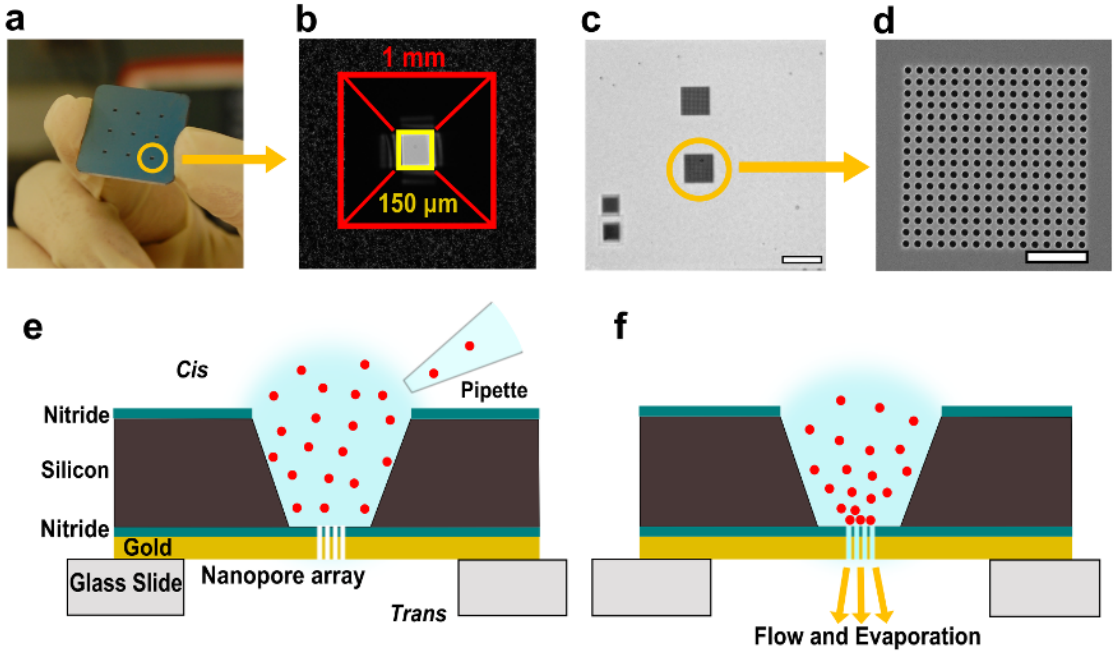

Figure 3.1: Nanopore array chips and schematic of assembly process. (a) A 1 inch × 1 inch chip with nine etched reservoirs leading to suspended nitride sensing regions. A single reservoir has been circled. (b) Bright-field image showing a single truncated pyramidal reservoir leading to suspended membrane. The opening on the *cis* side has sides ~1 mm leading to a Si_3N_4 membrane with sides of ~150 μm. (c) Bright-field image of the suspended membrane after milling 4 nanopore arrays. Scale bar is 20 µm. (d) Scanning electron micrograph of a nanopore array (pore diameter: 600 nm, periodicity: 1 µm) milled using focused ion beam. Scale bar is 5 µm. (e, f) Schematics of a single reservoir and suspended Si_3N_4 membrane region showing spontaneous accumulation of particles onto the nanopore array.

The time course of particle concentration was studied by taking time-lapse images. A drop of a solution of 0.1 M NaCl containing ~100 nm-diameter phospholipid vesicles was added on a single reservoir and images were taken every 5 seconds. Figure 3.2a shows a bright-field image of the suspended nitride area with five nanopore arrays. The larger 4 arrays (16 µm × 16 µm) have a 400 nm pore diameter and 1 µm periodicity

(pore center-to-center distance), whereas the smaller array (8 μm × 8 μm) has a 200 nm pore diameter and 500 nm periodicity. Figures 3.2b-d were taken from the time-lapse sequence and demonstrate the fluorescence increase over the nanopore arrays as more vesicles aggregate on them. The process is independent of the physical and chemical nature of the particle, as similar results were obtained for lipid vesicles extruded to 100 nm, silica beads (mean diameter: 700 nm) (Figure 3.2e-f) and fluorescently tagged polystyrene beads (mean diameters: 2 μm) (Figure 3.2g-h). Furthermore, during the observed interval, there was a steady flow of particles towards the arrays, which indicates that while the nanopores may be obscured by previously arriving particles, convective particle flux is not drastically reduced. Effective particle aggregation was observed for pore diameters ranging from 200 to 1200 nm. 8 μm × 8 μm arrays with a 200 nm pore diameter and 500 nm periodicity showed favorable results. Metallic nanopore arrays with these dimensions were previously used for SPR sensing.[22]

Dependence of the passive assembly process on evaporation was supported by a test where particle accumulation over the nanopore arrays was significantly reduced upon placing the chip in a humidity chamber (Figure 3.3). The effect of *cis*/*trans* addition as well as surface modification by deposition of silica on particle accumulation was studied (Figure 3.4). The samples were incubated with 10 μL solution of fluorescent polystyrene beads for 10 minutes and then imaged. Although changing between *cis* and *trans* addition of solutions resulted in relatively small variations in particle accumulation, changing the surface characteristics had a much more prominent influence. The nanopore chips with

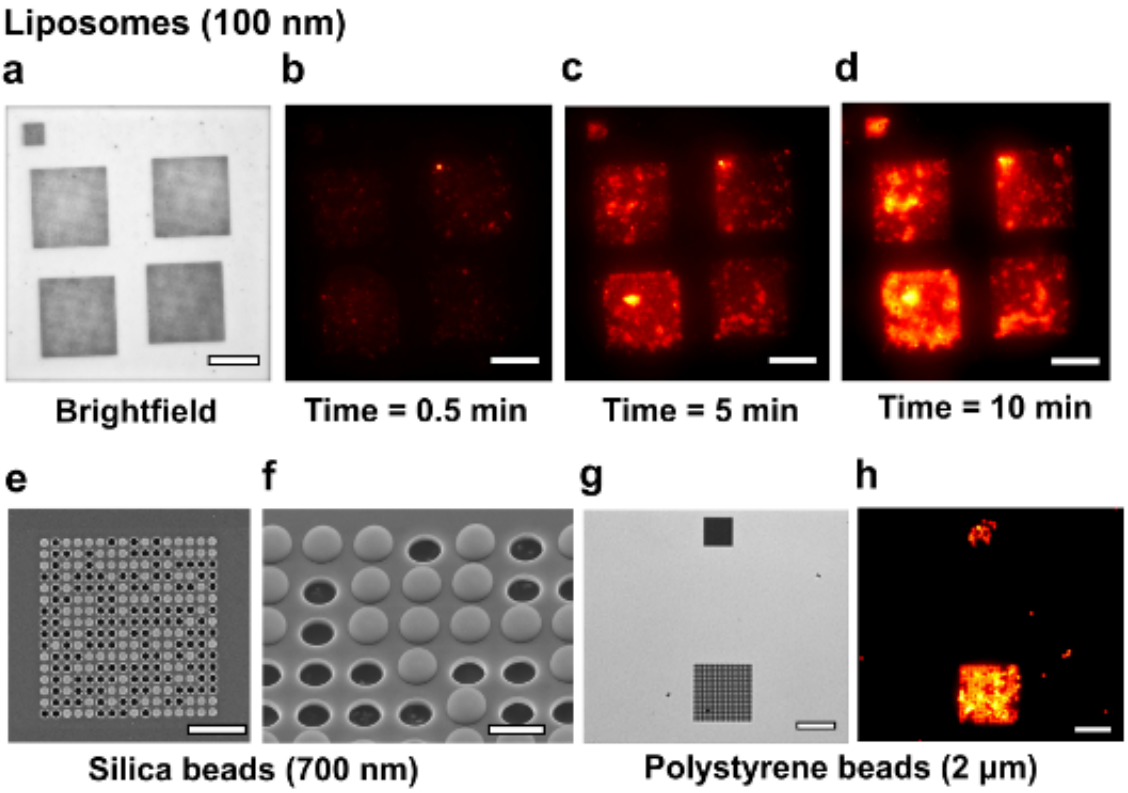

Figure 3.2: Rapid and materials-general particle assembly over nanopore arrays. (a-d) Bright field and time-lapse images of a suspended nitride area showing assembly of fluorescent liposomes over the array region. (e) SEM image demonstrating alignment of particles on an array having 600 nm pores with 1 μm periodicity. (f) A tilted zoomed-in image of the array. (g) A membrane with two arrays shown. (h) Polystyrene beads (2 μm) trapped on the arrays. Scale bar is 20 μm for figures (a-d, g-h), 5 μm for figure (e), 1 μm for figure (f).

conformal ALD silica coating demonstrated increased particle concentration as compared to unmodified Au/Si_3N_4 chips. This is likely due to improved wetting of the nanopores and increased surface area of the sample droplet on the more hydrophilic silica surface, which promotes faster evaporation. Nanopore-directed convection can also be used for passive, spontaneous self-assembly of particles using the right combination of array

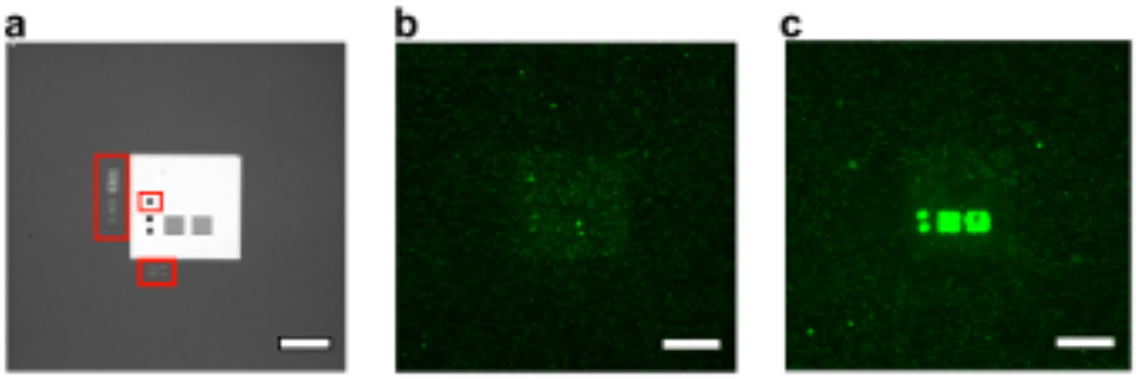

Figure 3.3: Evaporation dependent assembly of fluorescently tagged polystyrene beads (1.8 μm). a) Bright field image of the *trans* side of a chip with suspended nitride membrane and milled pore arrays. Gold was deposited on the *cis* side of this chip. The arrays enclosed in red rectangles are dead-ended. Two larger arrays (20 μm × 20 μm) have pore diameter 1 μm and periodicity of 2μm, whereas the smaller arrays (8 μm × 8 μm) have pore diameter of 200 nm and periodicity of 500 nm. b) Fluorescence image showing particle accumulation on a sample placed in the humidity chamber for 20 minutes. c) Fluorescence image showing particle accumulation on a sample placed outside the humidity chamber for 20 minutes. Scale bar is 50 μm for all the figures.

parameters, concentration of particles used and time allowed for aggregation. For optimal packing of the particles into arrays, the pore diameter was tuned to be slightly smaller than the particle diameter and the edge-to-edge distance between pores was less than the pore diameter. The silica beads had a mean diameter of 700 nm whereas the nanopores had a diameter of 600 nm and periodicity of 1 µm. The resultant bead arrays were very stable and they remained immobilized after overnight water submersion. Furthermore, the areas outside of the nanopore arrays were completely devoid of adsorbed beads.

Time-lapse sequences, which recorded accumulation of 2 µm polystyrene beads over nanopore arrays, were used to generate an estimate of solution flow rate through the

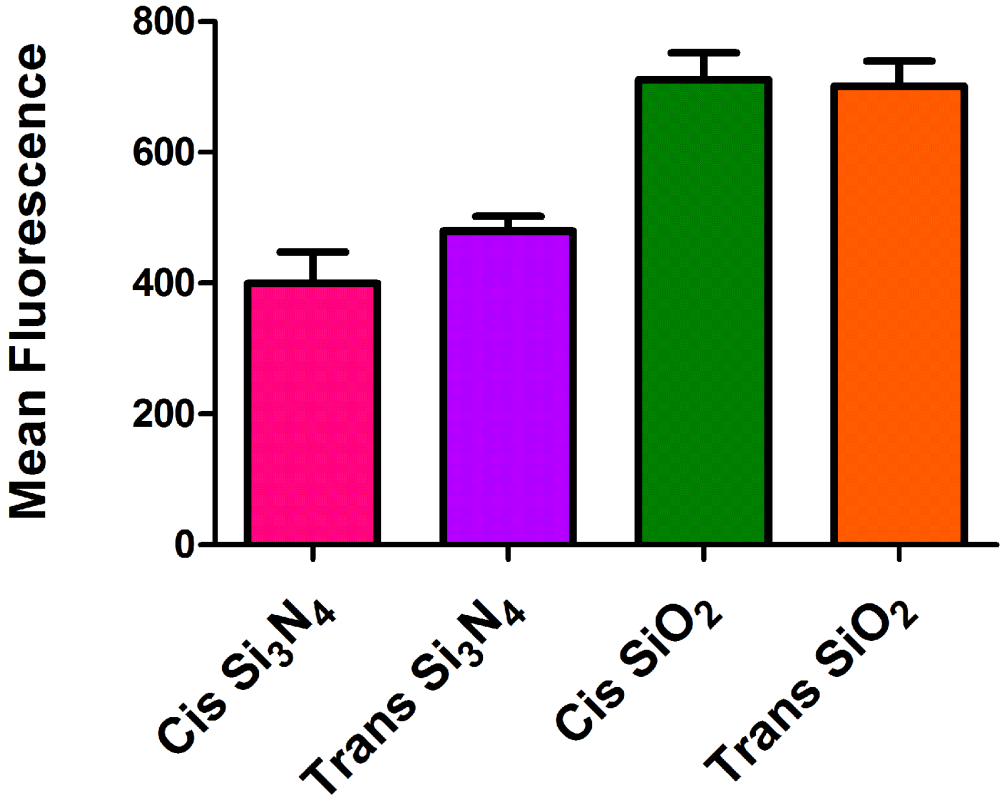

Figure 3.4: Assembly of fluorescently tagged polystyrene beads (1.8 μm) with respect to substrate geometry and surface. Mean fluorescence per array as obtained after 10 minute incubation time for different samples. Cis Si_3N_4 implies sample was added to the *cis* side of the chip with exposed nitride surface. Gold was on the *trans* side of this chip. For the plots labeled SiO_2, chips with 10 nm silica were used.

arrays. *Trans* addition of solution was used for two kinds of chips, type A with nitride surface exposed on the *trans* side and type B with 10 nm-thick silica deposited all over the chip. For an array (size 32 µm x 32 µm) with a 1.2 µm pore diameter and 2 µm periodicity, an estimated flow rate of approximately 6 nL/min for type A and 14 nL/min for type B was obtained. Individual arrays (size 16 µm x 16 µm) with a 600 nm pore size

and 1 μm periodicity were estimated to have a flow rate of ~3 nL/min for samples type A and ~5 nL/min for type B. Similarly, arrays (8 μm x 8 μm) with a 200 nm pore size and 500 nm periodicity had an approximate flow rate of ~1 nL/min for sample type A and ~2 nL/min for type B. Using this mechanism and by increasing the number of arrays, it should be straightforward to achieve passive flow through speeds in the order of 0.1 μL/min through suspended membrane nanopore arrays. Patterning large-area nanopore arrays can further increase the flow rates.

Protein preconcentration for biochemical assays is highly desired for early detection of low-concentration disease biomarkers. Micro- and nanofluidic channels in combination with applied electric field have been previously utilized for preconcentration and increased sensitivity for immunoassays.[39,40] The setup was utilized to demonstrate passive and rapid detection of low concentration analytes in small-volume droplets. The experiment was performed on a nanopore array chip with ALD silica coating. The chips were placed in a 1 mM silane-PEG-biotin solution overnight to form a monolayer of exposed biotin over the entire surface. The silane moiety covalently links the PEG-biotin to the silica surface and leaves the biotin free to interact with fluorescent SAPE (Figure 3.5a). A homogeneous monolayer of PEG-biotin ensures that SAPE can bind anywhere on the chip, not only on the nanopore array.

To confirm that the preconcentration process originates from trans-nanopore solution flow, an array of partially milled, dead-ended pores was used as control (Figure 3.5b-d). The dead-ended pores were exposed to the focused ion beam for around

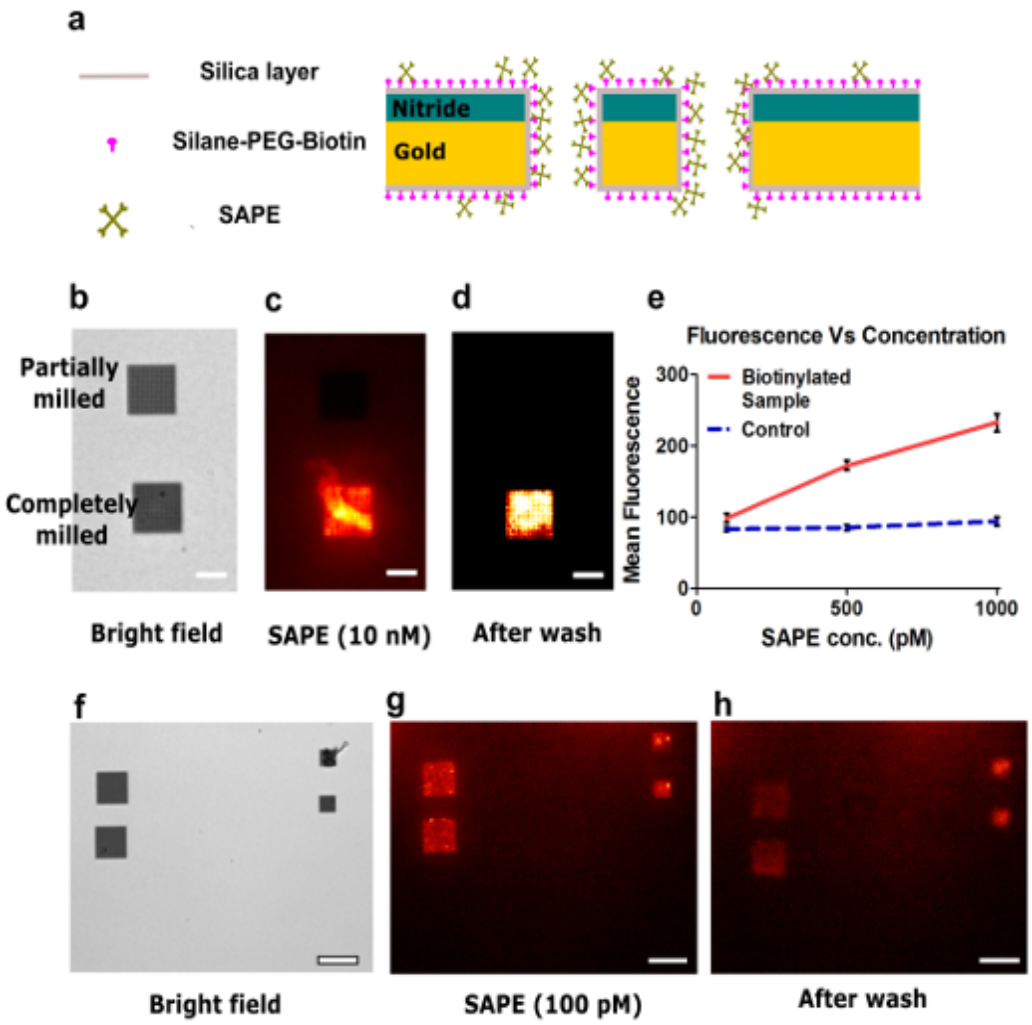

Figure 3.5: Schematic, flow dependence and low concentration analysis of SAPE-biotin binding. (a) Schematic showing all surfaces of the chip covered with silica and a monolayer of silane-PEG-biotin. SAPE is directed towards the nanopore arrays where it binds with the biotin. (b) Bright-field image of a suspended nitride region with one partially milled nanopore array and an array with completely milled pores. The arrays (16 μm x 16 μm) have a 600 nm pore diameter and 1 μm periodicity. (c) Fluorescence image of the sample after addition of 10 nM SAPE solution demonstrating nanopore-induced pre-concentration. (d) Fluorescence image of the sample after rinsing the chip with DI water. (e) A graph showing linear relationship between the mean fluorescence over the nanopore arrays as a function of the concentration of SAPE. (f) Bright-field image of a suspended nitride region with 4 nanopore arrays. (g) Fluorescence image of the sample

after addition of 100 pM SAPE solution. (h) Fluorescence image of the area after rinsing the chip with DI water. Scale bar is 10 μm for (b-d) and 20 μm for (f-h).

two-thirds of the time compared to the completely milled arrays. Upon adding a 10 nM SAPE solution, intense fluorescence was exclusive to the completely milled arrays. As the dead-ended pores could not display capillary action, SAPE binding in them was dependent on diffusion of molecules. Comparison of the fluorescence intensities in the completely milled and partially milled pores demonstrates that the directed convection in the open nanopores significantly increased the analyte concentration and binding (Figure 3.5b-d).

To quantify the concentration response of the nanopore arrays, SAPE concentrations of 1 nM, 500 pM and 100 pM were used and fluorescence of the nanopore array region was measured after an allowed binding time of 10 minutes and rinsing with DI water. Fluorescence was detected from nanopore arrays for all the samples. (Figure 3.5e-h) For 100 pM, the small concentration combined with the small volume (10 µL) means that 1 femtomole of SAPE molecules were added to the *cis* side of the chip (Figure 3.5f-h). A fraction of the solution was transported through the nanopores and detected within 10 minutes of concentration. For all the samples used, the background fluorescence from the region surrounding the nanopore arrays was not significantly larger than that observed before addition of SAPE. Also, a control sample, which had not been treated with silane-PEG-biotin solution, did not exhibit fluorescence from any region of the suspended membrane for all concentration values, indicating that SAPE does not

strongly adsorb to silica. The mean fluorescence value per nanopore array was plotted against concentration of SAPE for the samples (Figure 3.5e). The biotinylated sample shows a linear response in terms of measured fluorescence to the concentration of the SAPE used. The observed fluorescence intensity was not dependent on the pore diameter and periodicity, so the possibility of the fluorescence enhancement being due to plasmonic effects was negated.[41]

Analysis of SAPE binding to the nanopore arrays as compared to diffusion-limited dead-ended nanohole arrays has been further demonstrated in Figure 3.6. Directed convection of analyte solution to the nanopore arrays leads to accumulation of molecules and enhancement of fluorescence at the array site with time (Figure 3.6a). In comparison, there is no significant change in fluorescence measurements from the dead-ended nanohole arrays. For concentration-dependent binding analysis, SAPE concentrations of 1, 10, and 25 nM were added to the nanopore samples whereas the dead-ended nanoholes were used with SAPE concentrations of 25, 50, and 100 nM. The mean fluorescence values per nanohole array were obtained after a 10-minute binding interval and subsequent washing with DI water. Analysis of fluorescence measurements clearly demonstrates the enhanced binding response obtained from the nanopore array samples (Figure 3.6b).

Nanopore arrays with gold deposited on the *cis* side were used to measure SAPE binding by SPR. The diameter of the nanopores and periodicity of the array are 200 and 500 nm, respectively (Figure 3.7a inset). These dimensions were chosen to position

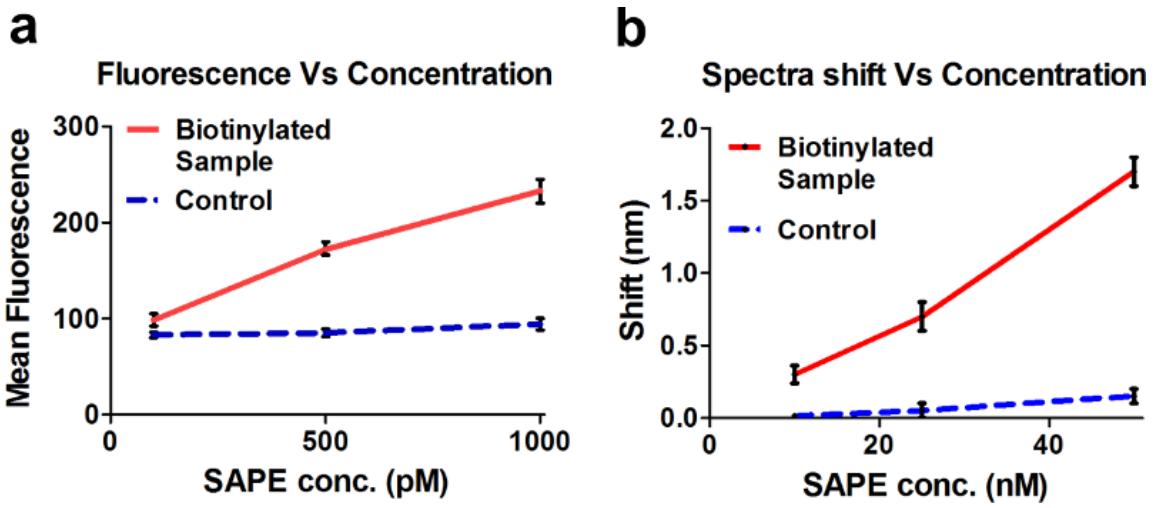

Figure 3.6: SAPE binding response for nanopore arrays as compared to control samples (dead-ended nanohole arrays). (a) Increase of mean fluorescence with time as a result of 25 nM SAPE binding in nanopore arrays (left axis) and control nanohole arrays (right axis). Analyte binding in dead-ended holes is limited by diffusion whereas nanopore-induced convection results in concentration of analyte. Addition of coverslip and fluorescence imaging were initiated 2 minutes post sample addition in order to allow the analyte solution to wet the reservoir and prevent formation of bubbles. (b) A graph showing the mean fluorescence values obtained from the arrays after 10 minute of SAPE binding and subsequent washing with DI water. Four arrays (16 μm x 16 μm) were milled for the binding analysis. Two arrays had hole diameter 200 nm and periodicity 500 nm while the other two had hole diameter 600 nm and periodicity 1000 nm.

optical transmission peaks through nanopore arrays in the visible regime for spectral measurements. Nanopore array made in metallic films can couple the incident light to surface plasmons, giving optical transmission peaks at specific wavelengths determined by the geometry of the array as well as the interfacial refractive index. The peak transmission wavelength is sensitive to the interfacial refractive index changes caused by molecular binding, and thus enables label-free SPR biosensing.[22] Normalized transmission spectra obtained through the nanopore array is shown in Figure 3.7a. A

transmission peak at approximately 800 nm, which is associated with surface plasmons at the gold-water interface, was used for sensing. The plot (Figure 3.7b) shows an increase in spectral shift with SAPE concentration for the biotinylated sample, whereas the control sample with no silane-PEG-biotin shows very little shift because of negligible nonspecific binding of SAPE to the surface, which agrees with the fluorescence measurements.

The results obtained with particles demonstrate that this method can be used to create particle nano- or microarrays without the need for chemical modification of the surface or particle. The successful application of microarray technology in high throughput analysis of biological particles has now led to tremendous interest in development of nanoarrays, which focus on immobilization of biomolecules in a small volume with very high spatial density.[42-45] In the method presented here, once the particles are in position and adhered to the walls of the nanopores, they could be utilized to perform statistical studies or create random particle arrays for multiplex biosensing experiments.[46,47] Accumulation of a monolayer of particles over 300 nm-deep nanopores enables study of the arranged particles from both the *cis* and *trans* sides of the chip. (Figure 3.8a) As seen in the schematic viewed from the *trans* side, each pore acts as a window with the ability to analyze the particle immobilized inside a nanopore. Thus an orderly assembly of particles in a nano- or microarray format is obtained without the requirement of any external chemical modification, which may alter the properties and behavior of the objects being tested. This method of analysis, where a thin membrane is

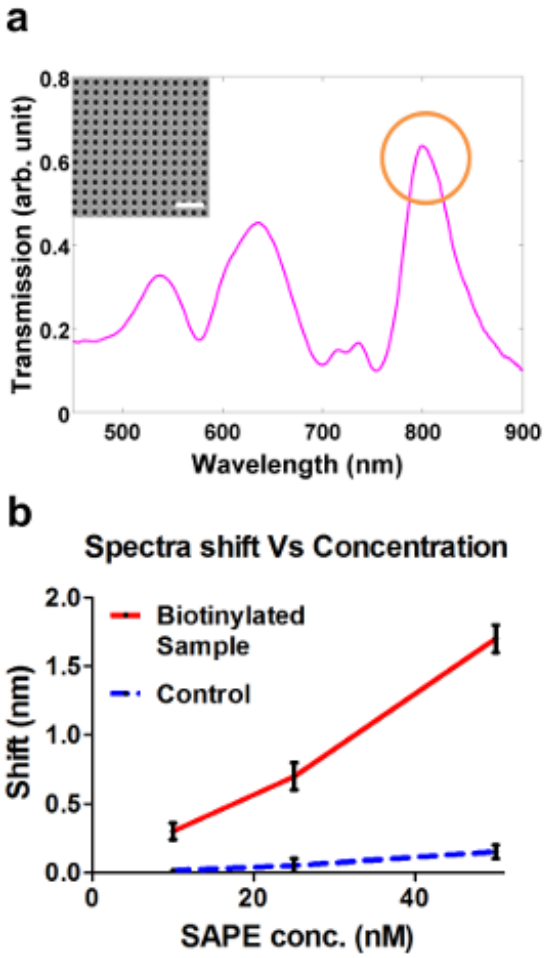

Figure 3.7: Surface plasmon resonance detection of SAPE-biotin binding. (a) Normalized transmission spectra as recorded from an array of 200 nm nanopores. The transmission peak at approximately 800 nm corresponds to the gold-water interface and was used to measure the shift in transmission. (Inset) SEM image of nanopores (diameter: 200 nm, periodicity: 500 nm) used for spectral measurements. Scale bar is 1.5 μm. Four arrays were milled on the suspended nitride area for measuring the transmission spectra, two large (16 μm x 16 μm) and two smaller (8 μm x 8 μm). (b) A graph showing shift of transmission spectra through the nanopore arrays upon SAPE binding as a function of SAPE concentration.

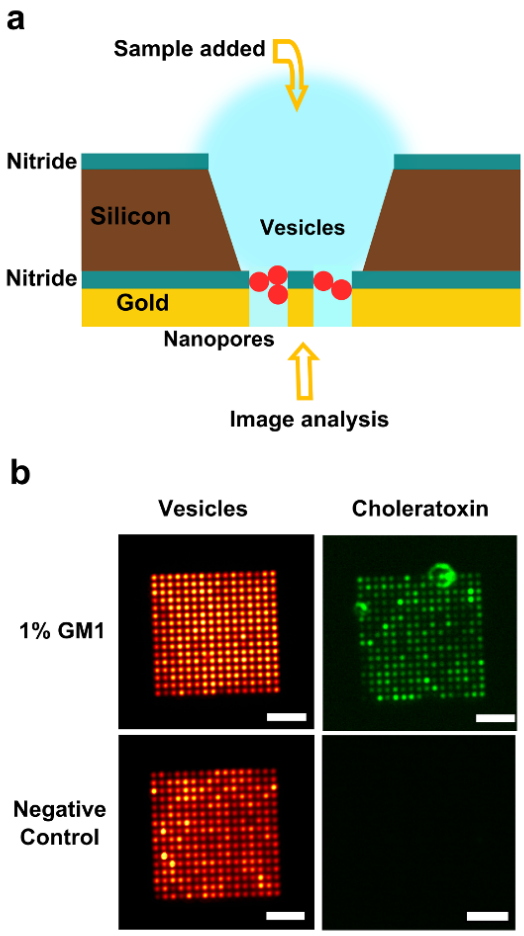

Figure 3.8: Suspended nanopore arrays for liposome assays. (a) Schematic showing that lipid vesicles immobilized in nanopores are accessible from both sides for analysis. (b) Two suspended nanopore arrays on a chip where vesicles were added from the *cis* reservoir side and images were collected from the *trans* side. The vesicles contained ganglioside GM1, which is bound by fluorescently tagged cholera toxin. The arrays (16 μm x 16 μm) have a 600 nm pore diameter and 1 μm periodicity. Scale bar: 5 μm.

used as a shadow mask to create an impression of arrays, can be utilized for single particle studies. For analysis of an array of single particles from both sides, the simplest case would be as visible in Figure 3.2e-f where the particle size is homogeneous, larger

than the pore diameter and results in a monolayer thus enabling single particle analysis. The process can also be efficient for physiologically relevant cases where the particle immobilization might be less uniform owing to size variability. This platform was utilized for assembly of lipid vesicles on-chip, which were then analyzed for the presence of a membrane component. Lipid bilayer vesicles act as models for cell membranes and this method could be utilized for study of membrane components including membrane-bound proteins, which are targets for the action of many drugs.[12,48] Vesicles with ganglioside GM1 (monosialotetrahexosylganglioside) were extruded to 200 nm and used for this assay. The B-subunit of cholera toxin (CTX) binds GM1 with high affinity. Nanopore arrays with a 600 nm pore diameter and 1 μm periodicity were used. The vesicle solution and subsequently Alexa 488-conjugated CTX were both added from the *cis* side. The images were obtained from the *trans* side utilizing each nanopore as a viewing window. Figure 3.8b shows the advantages of two open surfaces in this design, with the vesicles and their reaction with CTX being recorded in a visible array format.

3.4 Conclusion

This chapter has demonstrated a fast, passive, and small-volume method of directed immobilization of particles in orderly arrays using a suspended Au/Si_3N_4 membrane perforated with nanopores. The experiments demonstrate that nanopore arrays can act as nano-drains, spontaneously draining solutions from the reservoir via capillary flow and evaporation at the open end of the nanopores. This process, in turn, promotes molecular concentration and particle accumulation around the nanopores. This simple

setup improves analyte transport by directing convection to the sensor area, obviating the need for other complicated techniques or external power sources. The ease of experimentation, analysis and minimal sample consumption (less than 10 μL) make these nanopore arrays a powerful optofluidic platform for point-of-care sensing of biomarkers, which occur in low concentration. The simplicity of the passive sample injection and concentration makes the platform potentially useful for diagnostic applications in the developing world, as particle array formation or molecular concentration and subsequent fluorescence readout and analysis requires minimal setup and expertise. In addition, the nanopore-directed binding of molecules at the array site can be detected via SPR. The setup can also be used to obtain a periodic arrangement of monolayer of particles, aimed to gather statistical information from small-volume assays, which we further discuss in chapter 4. These results make a strong case for nanopore arrays as integrated optofluidic platforms, with their application demonstrated in label-free sensing, fluorescence assays, concentration and particle trapping. Efficient and large-scale fabrication of the nanopore platform is possible based on recent advances in high-throughput fabrication of metallic nanoholes.[17,25,49] This platform can readily be combined with nanohole-based SPR,[13,15,19,50] SERS,[14,37] and electrochemical sensors[38] for improved chemical selectivity and lower detection limits for molecules of biological and physiological relevance.

Chapter 4

Nanohole array-driven mitochondria assembly and analysis

Adapted from **Kumar, S.**, Wolken, G. W., Wittenberg, N. J., Arriaga, E. A., and Oh, S.-H. (2015) Nanohole array-directed trapping of mammalian mitochondria enabling single organelle analysis. *Analytical Chemistry*, 87 (24), 11973–11977. This work was performed in collaboration with Prof. Edgar Arriaga's group at the University of Minnesota, who provided the mitochondria samples and helped design the experiments.

The evaporation-driven flow technique introduced in the previous chapter is utilized here for on-chip assembly and analysis of mammalian mitochondria. This method enabled directed positioning of single mitochondria in individual nanoholes without the requirement of any external appendages or surface functionalization. Array-like assembly of mitochondria enabled statistical analysis of the difference in behavior of polarized and depolarized mitochondria.

4.1 Introduction

Mitochondria play important roles in cell-maintenance,[62] cell-death,[63] are linked with the aging process,[64] diseases like cancer,[65] and recently were used for bioenergy generation on chip.[66] Technologies facilitating on-chip bioanalytical analysis of mitochondria are therefore extremely relevant for their improved understanding and derived applications. Existing platforms for on-chip mitochondrial analysis are generally dependent on steps such as surface modification of the chip,[67, 68] microfluidic assemblies or electrical connections,[69-73] which limit the ease of sample delivery and analysis. Attempts have been made recently to overcome these limitations, utilizing platforms such as PDMS wells or optical fiber bundles for the analysis of yeast-derived mitochondria.[74, 75] These substrates are still reliant on random mitochondrial attachment with no directional control over localization of these organelles, require surface hydrophilization for organelle capture and have little scope for combination with other analytical techniques. Random distribution of mitochondria as well as staining of PDMS substrates by fluorescent dyes such as JC-1 can result in increased background fluorescence, which

interferes with sensitive analysis of these organelles. Substrates based on metallic nanohole arrays fabricated in silicon nitride membranes can lead to significant improvements over existing limitations for efficient and stable analysis of complex bioparticles such as organelles.

Metal-coated nanohole arrays[15] have emerged as a versatile bioanalytical platform having been widely used for analytical sensing including SPR,[76] SERS,[33] plasmon-enhanced fluorescence,[77] and single-molecule analysis.[78] They have also been utilized for on-chip detection and analysis of complex bioparticles such as exosomes,[59] viruses,[60] and virus-like particles.[61, 79] However, these platforms have also primarily relied on non-directional capture of molecules and particles, though some examples have spatially-heterogeneous surface chemistry for selective capture of particles. As discussed in chapter 3, nanoholes fabricated in free-standing silicon nitride (Si_3N_4) films can efficiently direct the flow of solution through them, which can be used for directed trapping of particles suspended in solution.[8, 9, 37, 80, 81] As this trapping methodology works well with aqueous media, it can be readily applied for the capture and array-based analysis of biological particles such as organelles.

This chapter demonstrates that nanohole-based passive flow-driven technique facilitates directed assembly of mammalian mitochondria arrays with exact positioning of single mitochondria inside individual nanoholes. Single mitochondria analysis can enable us to identify differences within as well as between organelle subpopulations, which is an improvement over analysis of aggregated organelles.[70, 82] Spatial control over the

localization of mitochondria can reduce random adsorption of organelles improving the signal-to-noise ratio, facilitating array-like analysis and improving integration with other analytical methods such as SERS.[80, 81] As the evaporation-driven flow minimizes the limitations imposed on the setup by surface-treatment or external attachment, it can be applied towards the stable analysis of complex bioparticles including other organelles and cells.

4.2 Methods

4.2.1 Chip fabrication

Low-stress nitride (Si_3N_4, 100 nm) was deposited on single-side-polished <100> silicon wafers using low-pressure chemical vapor deposition (LPCVD). Photolithography and dry etching were used to remove the nitride film from desired regions from the back of the wafers. The wafers were then immersed in a KOH bath for anisotropic etching of silicon to locally suspend nitride membranes. Gold (200 nm) was then deposited on the top, unetched surface of the chips using electron-beam evaporation. Individual chips sized 1 inch × 1 inch were obtained, each of which had 16 suspended membrane areas (100 μm × 100 μm). Focused ion beam with beam current 0.1 nA was used to mill nanoholes through the suspended gold-nitride bilayer membrane. Nanohole arrays were milled where each array consisted of 10 × 10 holes with hole diameter 600 nm and periodicity 1200 nm. Gold was utilized during the fabrication of these structures since it helps conduct ions during the focused ion beam milling stage of the fabrication, stabilizes the thin suspended nitride membrane and makes it opaque to transmitted light.

4.2.2 Mitochondrial preparation

L6 rat myoblast cells or 143B human osteosarcoma cells (ATCC) were cultured in DMEM supplemented with 10% fetal bovine serum (Life Technologies, Carlsbad, CA) in vented flasks at 37 °C and 5% CO_2 and were lifted with 0.25% trypsin and reseeded after reaching 90% confluency. For the sample loading experiments, mitochondria labeled with red, green, or both red and green fluorophores were produced. For the red-labeled mitochondria, 143B cells were transfected to express the DsRed2 fluorescent protein targeted to mitochondria (Clonetech, Mountain View, CA). The procedure to prepare 143B cells expressing DsRed2 targeted mitochondria has been previously described.[83] For green-labeled mitochondria, 143B cells were incubated with 160 nM MitoTracker Green FM (Life Technologies, Carlsbad, CA) for 30 min at 37 °C. For dual-labeled mitochondria, 143B cells expressing DsRed2 were labeled with MitoTracker Green. Mitochondria from cell culture were isolated by differential centrifugation and mechanical homogenization. Cells were lifted with 0.25% trypsin, washed three times, and resuspended in mitochondrial isolation buffer, which contains 210 mM mannitol, 70 mM sucrose, 10 mM HEPES, and 5.0 mM EDTA, adjusted to pH 7.4 with KOH. Cells were disrupted in a Kontes glass dounce homogenizer (Kimble Chase, Vineland, NJ). Cell breakage, determined by Trypan Blue staining and counting in a hemocytometer, was from 80-100%. After disruption, cellular debris was discarded by centrifugation at 600g for 10 min. Mitochondria in the supernatant were pelleted by centrifugation at 10000g for 10 min. Mitochondria were resuspended in mitochondrial isolation buffer in

concentrations normalized by initial cell count according to Trypan blue staining and kept on ice.

For the experiments involving polarized or depolarized mitochondria, initial mitochondrial fraction was then resuspended in respiration buffer containing 125 mM KCl, 10 mM HEPES, 5 mM $MgCl_2$, 2.5 mM succinate, 2 mM K_2HPO_4, and 1% DMSO, adjusted to pH 7.4 with KOH. For the depolarized mitochondria, the buffer also contained 2 μM valinomycin. Mitochondria were incubated in these buffers at 37 °C for 10 min with gentle mixing then labeled with 100 nM JC-1 (additional 5 min mixing at 37 °C). Samples were then kept on ice until loading on the nanohole array chip.

4.2.3 Sample loading

To capture mitochondria in nanoholes, 10 μL of buffer solution containing mitochondria was added to the backside reservoir of the nanohole array chip. The setup was left undisturbed for 10 minutes to direct mitochondria over the nanohole array region and eventually trap them inside nanoholes. To remove untrapped mitochondria from the chip, the reservoir area was washed by addition and suction of 10 μL of fresh buffer solution using a micropipette. This step was repeated three times. To confirm the trapping of single mitochondria in the nanoholes, two mitochondria samples were prepared. One sample contained mitochondria tagged with DsRed2 fluorescent protein, whereas the other sample had mitochondria tagged with MitoTracker Green (MTG). Equal volumes of the samples were mixed together before loading on the nanohole array substrate. For the depolarization of mitochondria on chip, 10 μL of buffer solution with mitochondria

containing JC-1 was added to the nanohole array substrate. Once the mitochondria were trapped, 1 μL buffer solution containing valinomycin at a concentration of 20 μM was added to the reservoir. After dilution, the actual valinomycin concentration in the reservoir was approximately 2 μM. The samples were imaged after being exposed to valinomycin for 2 minutes.

4.2.4 Imaging

The chips were placed on a Nikon Eclipse Ti-S inverted microscope stage and imaged in epifluorescence mode from the gold-coated side of the chip. The fluorescence images were acquired for 30 seconds using a 50× objective (Nikon, numerical aperture (NA) = 0.55). Filters were used with this setup to collect green (Chroma Technology Corp., Ex 449-489/Em 500-548) and red fluorescence (Chroma Technology Corp., Ex 540-553/Em 565-605). Photometrics CoolSNAP HQ2 CCD was used in combination with open source software Micromanager to record the images.[84]

4.2.5 Data analysis

ImageJ software with microarray profiler plugin (OptiNav, Inc.) was used to obtain fluorescence intensity information from the images.[85] The data was corrected for change in fluorescence due to photobleaching and other possible artifacts by calculating the photobleaching rate from sequential images of mitochondria samples with no valinomycin added to them, as well as background fluorescence information from areas

with no mitochondria present. Data plots were prepared using GraphPad Prism version 5.04 (GraphPad Software, Inc.).

4.3 Results and discussion

Nanohole array chips with a 100-nm-thick suspended nitride membrane were prepared as discussed elsewhere (Figure 4.1).[80] Mitochondria in suspension were added to the etched backside reservoir of the chips resulting in directed assembly of mitochondria onto the suspended nanoholes. The assembly of mitochondria arrays in nanoholes is driven by evaporation and capillary forces (Figure 4.2a).[80] This process works on the principles of the coffee-stain effect where capillary flow towards pinned edges of a water drop results in concentration of particles.[86] In this case, the meniscus of water inside the nanoholes undergoes constant evaporation and is replenished by flow of water from the large drop of mitochondrial suspension.[80] This directed flow drags any particles suspended in the aqueous solution towards the nanoholes, where they are trapped. Once assembled, the samples were imaged through the gold-coated side of the nanoholes. An image of a suspended membrane area with four mitochondria arrays can be seen in Figure 4.2b. These mitochondria were tagged with a mitochondrial-selective fluorescent label MitoTracker Green (MTG).

These arrays were formed within minutes simply by the addition of solution on the substrate, enabling rapid trapping and simultaneous fluorescence analysis of many mitochondria in a periodic array. The nanoholes have a diameter of 600 nm and their

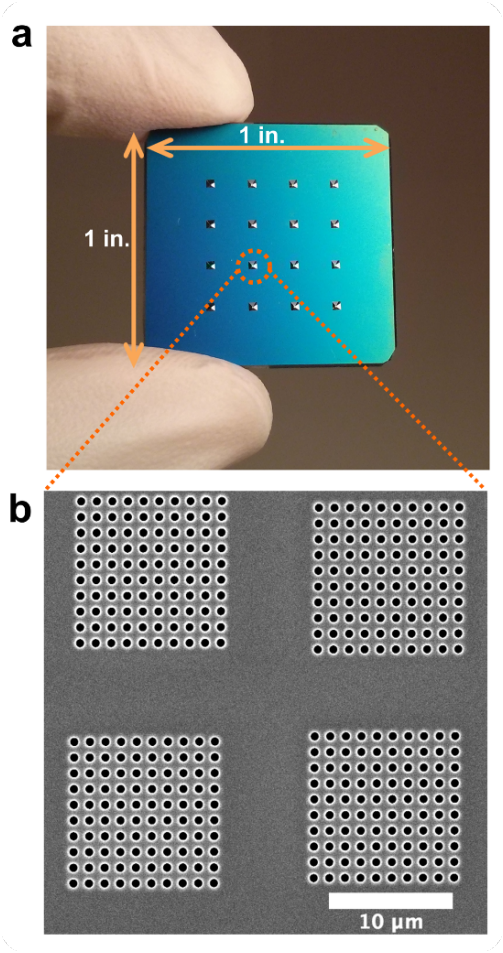

Figure 4.1: Nanohole array chip. (a) A photograph showing the backside of a 1 inch × 1 inch silicon chip with 16 KOH etched reservoirs visible. (b) A SEM showing 4 arrays milled on the suspended nitride membrane with hole size 600 nm and periodicity 1200 nm.

depth, which is defined by the thickness of the nitride membrane and the thin metal film, is 300 nm. The average diameter of mitochondria used in these experiments was around 600 nm. Nanohole diameter of 600 nm was chosen as a starting point for these experiments to enable optimal trapping of mitochondria while reducing the chances of multiple mitochondria cohabiting the same hole. The limited size combined with diluted

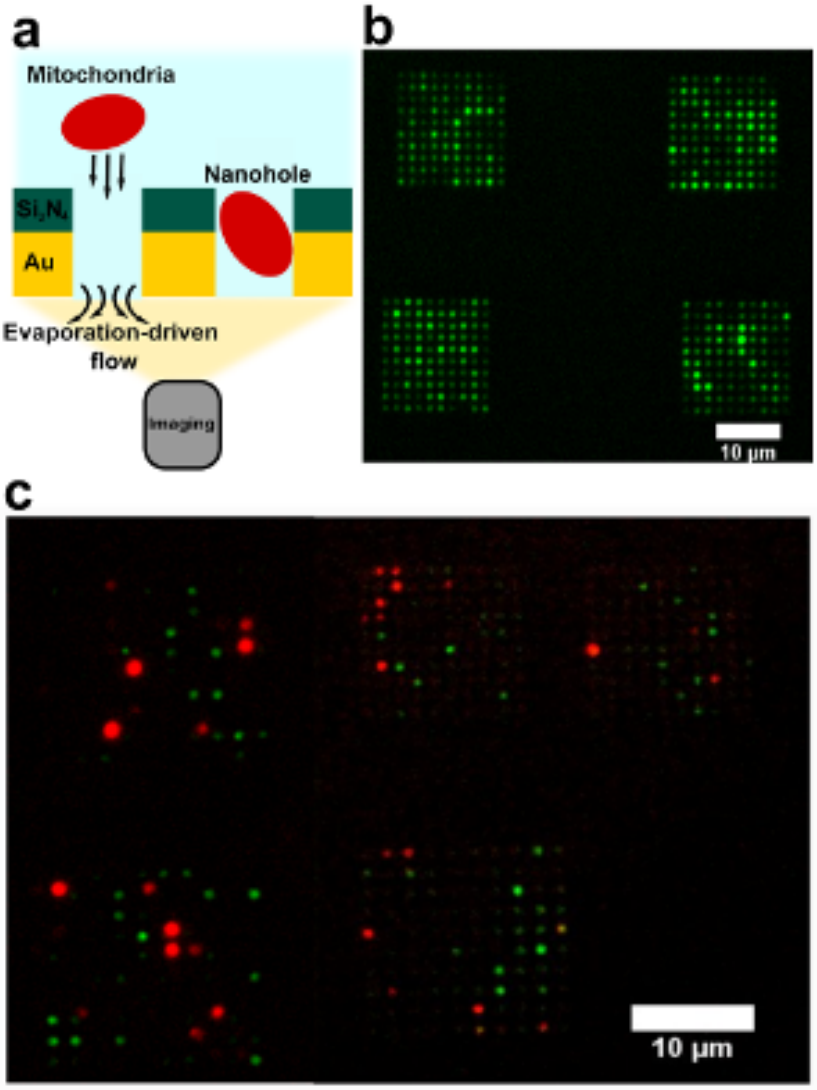

Figure 4.2: Sample analysis in an array format. (a) Sample was added to the backside reservoir on the chip and mitochondria were allowed to assemble on to the nanoholes. The samples were washed and then imaged from the gold-coated end of the nanoholes. (b) Image shows 4 arrays containing trapped mitochondria tagged with MitoTracker Green dye. (c) Two samples containing mitochondria tagged with a fluorescent marker (DsRed2 in one sample and MitoTracker Green in the other) were diluted and mixed. The mixed mitochondria suspension was then added to the chip over the nanohole arrays for the capture of mitochondria. Image shows 5 arrays containing captured mitochondria tagged with either DsRed2 or MitoTracker Green.

mitochondria suspension was expected to facilitate trapping and visualization of isolated single mitochondria in the nanoholes. This was tested using two mitochondria samples, each tagged with a different fluorophore. In one sample mitochondria were tagged with DsRed2 fluorescent protein whereas in the other sample mitochondria were tagged with MTG. Equal volumes of the samples were mixed, added to the nanohole array substrate and then imaged. An image showing overlap of the two fluorescence channels for these experiments can be seen in Figure 4.2c. The arrays were analyzed to record the number of holes with green, red and overlapping colors (Figure 4.3). Green fluorescence was observed from 63% of the occupied holes (# of holes = 51), red from 35% (# of holes = 34), whereas overlap of colors was seen in a small fraction of the holes (2%) in the arrays (# of holes = 2).

The relative excess of MTG to DsRed2 mitochondria (63 % vs. 35 %) can be due to a few factors. First, prior to mixing, the mitochondria concentration in the MTG- tagged sample may have been greater than that of the DsRed2 sample, creating an excess of MTG relative to DsRed2 mitochondria. Second, DsRed2 fluorescence is dependent upon expression of DsRed2 protein, which varies across mitochondria and may not be expressed in some mitochondria. In fact, some of the apparently empty nanoholes in the array may be occupied by mitochondria from the DsRed2 sample that do not express DsRed2 or express it at concentrations below the detection threshold, which skews the apparent distribution toward an excess of MTG-tagged mitochondria. The variation in red fluorescence intensities visible in Figure 4.2c can be due to difference in expression of

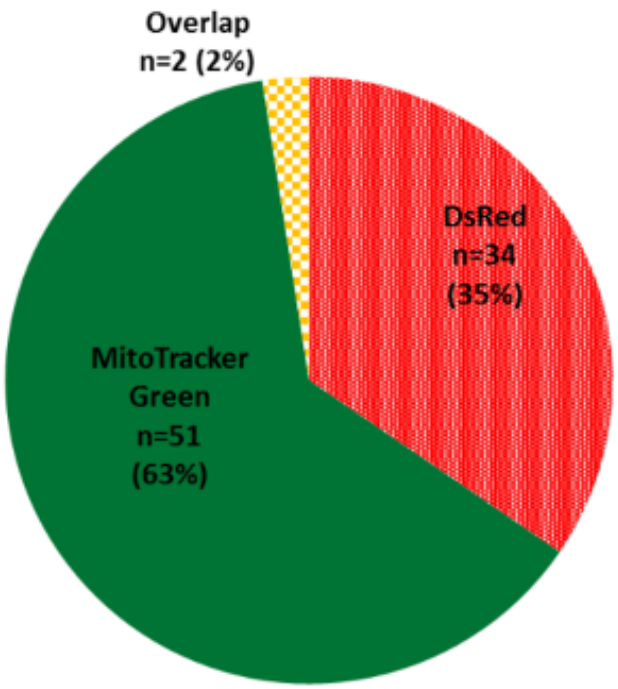

Figure 4.3: Counting trapped mitochondria. Chart showing the number of nanoholes occupied by red or green-labeled mitochondria in five arrays (500 nanoholes) along with the overlaps.

DsRed2 protein amongst the trapped mitochondria.

For the known number of holes and observed numbers of mitochondria in Figure 4.3, we can estimate the probability of overlaps. We assume that the mitochondria are captured randomly in the nanoholes, the capture of red and green mitochondria are independent events and we neglect the chances of capturing more than one mitochondria of same color in a nanohole. Using these assumptions, we can state that the probability of a nanohole capturing a red-labeled mitochondria is P(R) = (number of captured red

labeled mitochondria)/ (number of nanoholes) = 36/500 = 0.072. Similarly, the probability of a nanohole capturing a green-labeled mitochondria is P(G) = 63/500 = 0.126. As we consider the capture of differently-labeled mitochondria to be independent events, the probability of capturing both in a single hole can be calculated using, $P(R \cap G) = P(R) \times P(G) = 0.009072$. For 500 nanoholes, we can expect to see overlap in about 4 nanoholes on average, which is close to our observation.

The application of the organelle-on-a-chip system for fluorescence-based analysis of mitochondrial properties, in particular their membrane potential, was demonstrated. The transmembrane potential in mitochondria is an important indicator of function.[87] Trapped mitochondria were treated with valinomycin that depolarized mitochondria on chip. Valinomycin is a potassium ionophore, which facilitates the transport of potassium ions through the membrane leading to decrease of the mitochondrial membrane potential i.e. depolarization of the membrane.[88] This change in mitochondrial membrane potential can be visualized using a membrane-permeant JC-1 dye, whose accumulation in the mitochondria is dependent on the transmembrane potential.[89] The dye can exist in a monomeric form (green fluorescence, emission ~529 nm) or can form J-aggregates (red fluorescence, emission ~590 nm). Increase in the mitochondrial membrane potential causes accumulation of the dye in the mitochondria, facilitating the increase in the formation of aggregates and leading to higher red-to-green fluorescence ratio. Depolarization of the mitochondrial membrane is indicated by a decrease in ratio of red-to-green fluorescence emission from red (~590 nm) to green (~529 nm). For samples

under observation, this ratio of red-to-green fluorescence intensity is recorded to monitor the changes in mitochondrial membrane potential.[89]

The schematic for two approaches of mitochondria depolarization is shown in Figure 4.4a. In the first approach valinomycin was added to polarized mitochondria trapped on the chip (Case A), whereas in the second approach mitochondria were depolarized off-chip in bulk suspension (control) and then added to the chip (Case B). These samples were imaged before and after on-chip valinomycin treatment. The JC-1 fluorescence values were monitored and the ratios were calculated. Plots showing the fluorescence ratios before and after on-chip addition of valinomycin for twenty-five holes on a single array are shown in Figure 4.4b-c. The decrease in the red-to-green fluorescence ratio for each nanohole can be tracked from the plot. The variation in the fluorescence ratio for the polarized samples can be due to in-sample heterogeneity i.e. difference in the transmembrane potential or functional states of different trapped mitochondria.

Fluorescence ratios for all nanoholes in a single array are shown in the form of vertical scatter plots (Figure 4.4d-e). The decrease in the red-to-green fluorescence ratio for each nanohole can be tracked from the plot. Before valinomycin addition, the mean value of red-to-green fluorescence for the polarized samples was 0.55 and the median was 0.47. After valinomycin addition, the mean value changed to 0.31 whereas the median changed to 0.30. For the bulk-depolarized control samples, the mean and median

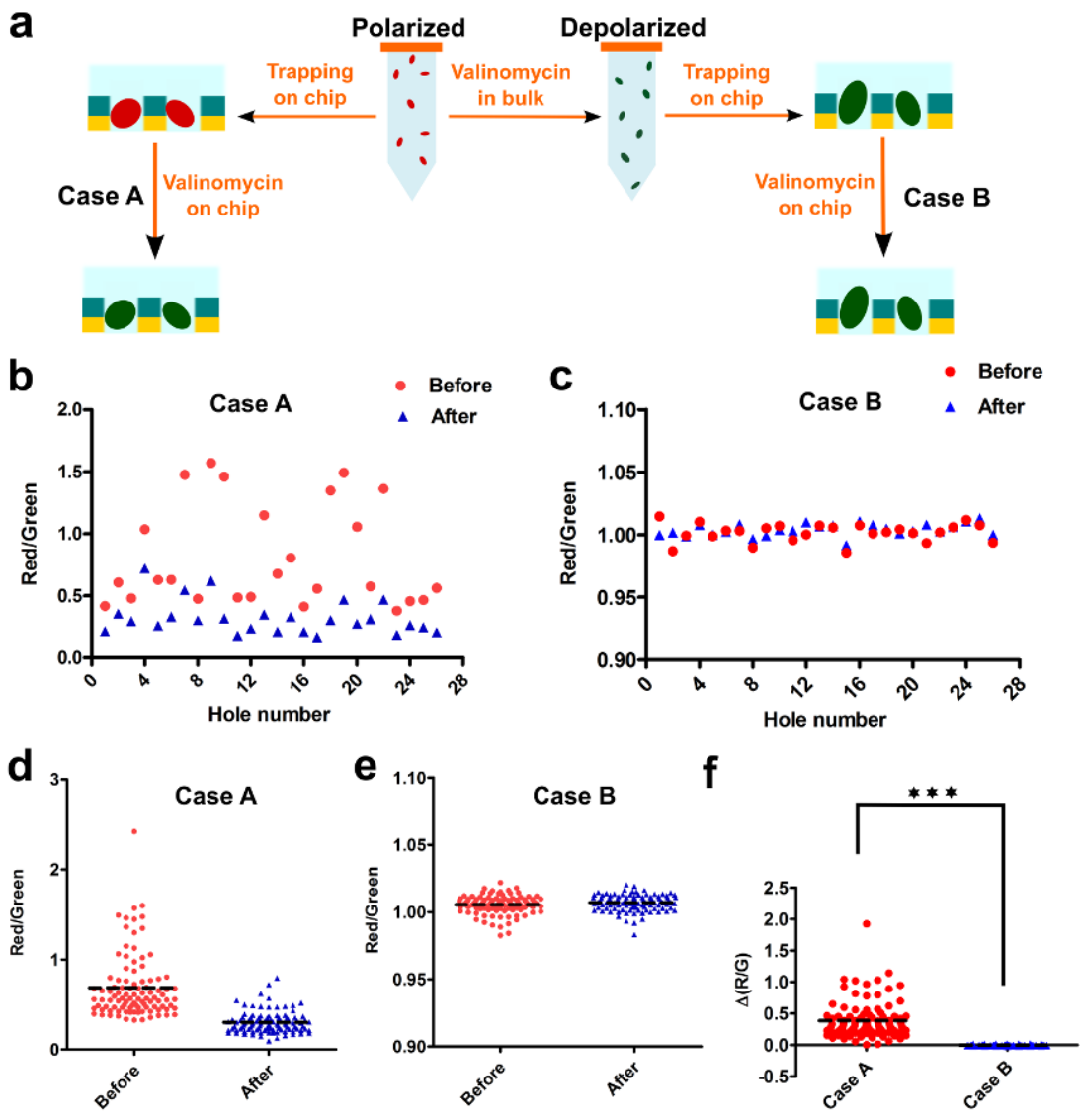

Figure 4.4: Statistical analysis using mitochondria arrays. Mitochondria tagged with JC-1 dye were treated with valinomycin and the change in the ratio of red-to-green fluorescence was monitored for each nanohole. (a) Depiction of the experimental scheme using two samples of mitochondria. On-chip valinomycin addition to polarized mitochondria has been termed as Case A whereas addition of valinomycin to already depolarized mitochondria has been termed as Case B. (b) 25 holes on an array containing polarized mitochondria i.e. case A. Vertically aligned data points were obtained from the same hole before and after on-chip valinomycin addition. (c) 25 holes on an array

containing bulk-depolarized mitochondria i.e. case B. Vertically aligned data points were obtained from the same hole before and after on-chip valinomycin addition. (d) Vertical scatter plot showing the distribution of red-to-green ratio for all holes in an array before and after on-chip valinomycin addition for case A. (e) Vertical scatter plot showing the distribution of red-to-green ratio for all holes in an array before and after on-chip valinomycin addition for case B (f) The difference in the red-to-green fluorescence ratio (i.e. $\Delta R/G$) = R/G before – R/G after) shown for an array with polarized mitochondria (case A) and pre-depolarized mitochondria (case B). T-test indicates significant difference in the change observed for the two cases, ***$p < 0.0001$. Dashed line indicates the mean value for all the plots.

fluorescence ratios before on-chip valinomycin addition were both 1.01. After on-chip valinomycin addition, the mean and median ratios showed no change with their value being 1.01. Unpaired t-tests performed for the two cases calculated a statistically significant difference in the means for the polarized samples ($P \leq 0.0001$), whereas for the control samples the change was not significant ($P = 0.1138$).

The change in the red-to-green fluorescence ratio before and after on-chip addition of valinomycin were calculated. This change is defined as the difference between the fluorescence ratio before and after addition of valinomycin on chip ($\Delta(R/G)$ = R/G before – R/G after). A scatter plot for calculated $\Delta R/G$ for the nanoholes in a single array for both cases is shown in Figure 4.4f. The mean change for the polarized samples was about 0.25 units, whereas the change for the bulk-depolarized control samples was close to zero. A t-test comparing the calculated change for a polarized sample vs. control also showed that there is statistically significant difference ($P \leq 0.0001$) between the changes in fluorescence-ratios observed. The observed response indicates that the mitochondria maintain their viability and function during this on-chip

assembly process. The setup allows monitoring of individual mitochondria localized at multiple identifiable spots on the same chip with the ability to perform multiple assays.

4.4 Conclusion

The work presented in this chapter shows that nanohole arrays fabricated on nitride membranes can be used as a platform for directed, localized trapping of mitochondria by addition of a micro-droplet. The application of this simple, efficient, self-propelling and biocompatible platform was demonstrated through trapping and subsequent array-based analysis of individual mammalian mitochondria. The effect of external chemical stimulus in the form of valinomycin on polarized mammalian mitochondria was recorded and compared to pre-depolarized mitochondria. The observed difference in their response clearly indicated that the mitochondria maintain their viability and function after the passive flow-driven on-chip assembly process, indicating the potential of this platform for stable analysis of fragile bioparticles including organelles and cells. Fabrication techniques such as nanoimprinting can be used in the future to obtain large-scale arrays, allowing us to analyze larger sample sizes.[81] Importantly, this platform can be easily combined with techniques such as SPR imaging,[90] nanohole-enhanced SERS[33, 81] or electrochemistry[91] for high-throughput multimodal organelle-on-a-chip analysis. Hence this platform can be a uniquely attractive tool for stable organelle analysis as it promotes directed localization with minimal limitations and complexity, while supporting diverse analytical techniques.

Chapter 5

Surface tension-driven flow through nanoholes

Adapted from **Kumar, S.**, Cherukulappurath, S., Johnson, T.W. and Oh, S.-H. (2014). Millimeter-sized suspended plasmonic nanohole arrays for surface-tension-driven flow-through SERS. Chemistry of Materials, 26(22), 6523-6530. Computer simulation plots by T. Johnson.

This chapter presents an alternative technique for fabrication of plasmonic nanohole arrays in freely suspended silicon nitride membranes utilizing nanoimprint lithography. Nanohole arrays in freely-hanging nitride films with size approximately 1 mm^2 were obtained as compared to arrays with sizes on the order of 100 μm^2 used previously. A surface tension-based method for driving flow of solution through plasmonic nanoholes has been introduced in this chapter, and was observed to be an order of magnitude faster than evaporation-driven flow. The optical properties of the substrates were also tuned for maximizing the SERS signal intensity. Combination of surface tension-driven flow and optimized SERS detection enabled rapid and sensitive optical detection of analytes on this nanohole array platform.

5.1 Introduction

As discussed in Chapter 3, the field of optofluidics explores new possibilities to combine optical detection techniques with micro- and nanofluidics[92-94] to develop miniaturized optical sensors with improved performance. Analytical techniques such as SPR, SERS, and fluorescence imaging are commonly used with these sensors.[95] SERS, a powerful technique for biosensing and chemical identification, largely depends on the drastic enhancement of weak Raman signal obtained from analyte molecules, upon their interaction with optical near-fields of metallic nanostructures.[23, 96] As an analytical technique, SERS combines the benefits of label-free sensing, high sensitivity, and chemical specificity. An important aim is to further improve the capabilities of SERS for diverse applications such as healthcare and environmental monitoring using substrates

which can be fabricated reproducibly and have uniform geometry.[97] As the enhancement of electromagnetic fields occurs in nanoscale regions, termed as plasmonic hotspots, integration of microfluidics capable of directing the analyte flow and resultant concentration towards these hotspots can improve the sensitivity and reduce the detection time for SERS.[7, 9, 36, 80] Among various options, metallic nanohole arrays fabricated in suspended silicon nitride (Si_3N_4) membranes can provide a unique option to integrate SERS with flow-through sensing.

Nanohole arrays in thin metallic films can act as plasmonic substrates with multifarious applications. Enhancement of the electromagnetic field and extraordinary optical transmission (EOT) through the nanoholes has led to their application in plasmonic sensing.[15, 98-100] Primarily, they have been used as a platform for SPR refractive-index sensing.[40, 76, 101-103] While groups have demonstrated nanohole-enhanced Raman spectroscopy,[33, 104-106] the reported Raman enhancement factors (below ~10^5) are weaker than that of other SERS substrates. And these previous experiments relied on low-throughput fabrication techniques such as focused ion beam (FIB) or electron-beam lithography to pattern nanoholes in a metal film. Suspended nanohole arrays have been utilized for SPR sensing, but have not been utilized for SERS. Flow of analyte solution through suspended nanoholes has been utilized for overcoming diffusion-limited transport in SPR sensing.[8, 9, 37, 80, 107] Most of these methods, however, require external sources for generating pressure gradients, which can often damage the fragile membrane,

and microfluidic tubing or an external power supply for creating an electric field. A simple and robust sample delivery mechanism can eliminate the flow-through sensing.

In this chapter, nanoimprint lithography (NIL)[108-111] is used to fabricate periodic Ag nanohole arrays over a millimeter-sized suspended silicon nitride (Si_3N_4) membrane with high throughput and reproducibility. To improve Raman enhancement factor (EF) on these large-area substrates, plasmon resonances of suspended nanohole arrays are precisely tuned using a sucrose solution. Raman EF of up to 10^7 is obtained for silver-coated suspended nanoholes using this technique. Furthermore, suspended nanohole arrays are demonstrated to be capable of fast flow through the nanoholes driven by surface tension forces, which promote adsorption of the analytes towards the plasmonic hotspot and further boost the SERS signal by 50 times compared to diffusion-limited transport. Using this optofluidic SERS substrate, 100 pM 4-Mercaptopyridine (4-MP) sample was detected.

5.2 Methods

5.2.1 Fabrication of large-area suspended nanohole arrays.

Suspended nanohole arrays were fabricated over a region of size 1 mm^2 using nanoimprint lithography (NIL) as shown in Figure 5.1(a-c). Low-stress silicon nitride (200 nm) was deposited on both sides of single-side polished (100) silicon wafers using low-pressure chemical vapor deposition (LPCVD). These wafers were then patterned using photolithography and dry etching such that some regions on the back of the wafers

had nitride removed exposing the silicon. Nanoimprint resist was then spun over the top surface of the wafer. A nanoimprint mold was carefully placed on the resist so that it aligned well with patterns etched on the back of the wafer. The mold used for nanoimprinting had pillars with 200 nm diameter, 500 nm periodicity and 300 nm pillar height over a 1 cm × 1 cm area. Nanoimprinting generated nanohole patterns in the resist layer. The sample was further processed to etch the nanohole arrays into the top nitride layer. The etching was done for a fixed time-period such that the holes go about two-thirds of the way into the nitride. This was necessary to protect the silicon from subsequent KOH etching. The nanoimprint resist was then cleaned off and samples were placed in a KOH bath for anisotropic etching. A suspended nitride membrane with nanohole array patterns was obtained. The samples were further dry-etched to remove the remaining nitride from the bottom of the nanoholes and obtain suspended open-ended nanoholes. Silver (120 nm) was then deposited on the top of the samples using an electron-beam evaporator.

5.2.2 Raman spectroscopy

For Raman measurements of BZT and 4-MP solutions, a quartz cuvette with 1 mm path length was used. A 785 nm diode laser with incident power of 10 mW was loosely focused onto the sample using a 10× objective. The Raman scattered light was collected in transmission mode using a 50× objective (NA 0.5) and passed onto a spectrometer (Ocean Optics QE65000) through a multi-mode fiber after removing the excitation light with a notch filter. The acquisition time was 30s. Neat BZT (~ 10 M) and

0.6 M 4-MP solution were used to acquire the Raman spectra. For formation of a self-assembled monolayer (SAM), chips were placed in 1 mM BZT (eth.) or 1 mM 4-MP (aq.) overnight. They were then rinsed thrice with ethanol (BZT samples) or deionized (DI) water (4-MP samples) over a period of 30 minutes. The parameters used for calculation of the enhancement factor are described in Supporting Information.

5.2.3 Optical analysis

The chips were placed on a Nikon Eclipse LV 100 upright microscope stage with a 10× objective and a fiber-optic spectrometer was used to record transmission spectra through the nanoholes. Sucrose solutions of desired concentration (0 - 1.5 M) were used to tune the transmission spectra. SERS signal was then obtained from the samples. ImageJ software was used for analysis and coloring of the images. Data plots were prepared using Matlab (MathWorks, Inc.) and GraphPad Prism version 5.04 (GraphPad Software, Inc.).

5.2.4 Computational modeling

Three-dimensional (3D) finite-difference time-domain (FDTD) simulations around the suspended nanoholes were performed using FullWAVE^{TM} simulation software. (RSoft, Inc.) A single hole was simulated with periodic boundary conditions on the faces intersected by the metal film to represent an infinite hole array and absorbing boundary conditions on the final two faces. A grid size of 3 nm was used around the hole in all dimensions. The index of refraction for the nitride was set at 2, the optical constants

for silver were measured via ellipsometry, and the refractive indices of materials surrounding the hole array were varied. The excitation wavelength was set to 785 nm to match experiments.

5.2.5 Surface tension-induced flow

A 30-nm-thick SiO_2 film was deposited on the back of the samples using an electron-beam evaporator. Using this directional deposition technique, the sidewalls of the nanoholes, which lie parallel to the direction of evaporation, were coated with a much thinner layer of silica. Desired volume of aqueous solution was then added to the top surface of the chips.

5.2.6 Bead and 4-MP concentration

Fluorescent polystyrene beads were obtained from Bangs Labs, - poly (Styrene/2%DiVinylBenzene/Vinyl-COOH), mean diameter 2.19 μm, and used at a final concentration of 10^6 beads/mL in DI water. 10 μL solution containing beads was added on the top of the chips for the three cases I, II and III. The samples were left undisturbed until the solution was consumed through evaporation or flow. The top was then imaged using a fluorescence microscope to monitor accumulation of particles. For SERS measurements, 4-MP solution of desired concentration and volume was added to the top of the chips and allowed to completely flow through. Sucrose solution was used to obtain the optimized SERS signal from the chips as discussed earlier. In the case of loss in the volume of sucrose from the top of the chip due to flow-through, fresh sucrose solution

was added to the sensing region.

5.2.7 Calculation of enhancement factor (EF)

The surface enhanced Raman signal (SERS) EF were calculated using the following equation:

$$EF = \frac{I_{SERS}}{I_{RAMAN}} \times \frac{N_{RAMAN}}{N_{SERS}}$$

I_{SERS} refers to the intensity of surface enhanced Raman peaks measured from the nanohole arrays. I_{RAMAN} refers to the intensity of Raman peaks measured directly from neat Benzenethiol (BZT) or 4-Mercaptopyridine (4-MP) solution in a cuvette. N_{SERS} and N_{RAMAN} refer to the number of molecules contributing to the SERS and Raman signal respectively.[112]

N_{SERS} was calculated using $N_{SERS} = SA * \rho_{surface}$, where SA = surface area of the chip under focused illumination, and ρ = packing density of Raman active molecules on the surface. The value used for ρ was 6.8×10^{14} molecules/cm^2.[113] The top metal surface as well as the nanohole sidewalls were included for calculating the value of N_{SERS}. N_{RAMAN} was calculated using $N_{RAMAN} = A * d * \rho_{solution}$, where $A = \pi r^2$ = area of the focused beam, with r (50 μm) being the radius of the focused beam spot, d = effective depth of the solution containing molecules contributing to the Raman signal and $\rho_{solution}$ = density of the Raman active molecule in solution.

The effective depth of solution, which refers to the depth of effective cylindrical focal

volume in solution containing molecules contributing equally to the Raman signal was calculated. SERS signal was obtained from a metallic nanohole array sample coated with BZT self-assembled monolayer with the beam focused on the sample surface and the objective lens position optimized for maximum signal. The objective was then moved, towards and away from the chip with 50 μm increments so that the focal plane was shifted with every step. Raman signal was recorded at each of these locations from the same position on the sample. The measured signal was plotted against the distance and the resultant area under the curve was calculated. This area gives us the total signal obtained from the effective focal volume. Dividing this area by the largest measured signal, gives us the effective depth (d) of the cylindrical effective focal volume.[114] The effective depth was calculated to be 230 μm and used for the calculation of enhancement factor.

5.3 Results and discussion

Suspended metallic nanohole arrays were fabricated on low-stress silicon nitride (Si_3N_4) membranes using NIL (Figures 5.1a-c). One such chip with a 1 cm × 1 cm area of imprinted nanohole arrays is shown in Figure 5.1d. The suspended membrane region, approximately 1 mm × 1 mm defined by KOH wet etching of Si, consisting of open-ended nanoholes is also indicated. A scanning electron micrograph (SEM) shows uniform suspended nanohole arrays (Figure 5.1e). An SEM image at higher magnification shows individual nanoholes in the silicon nitride membrane (Figure 5.1f). The holes are

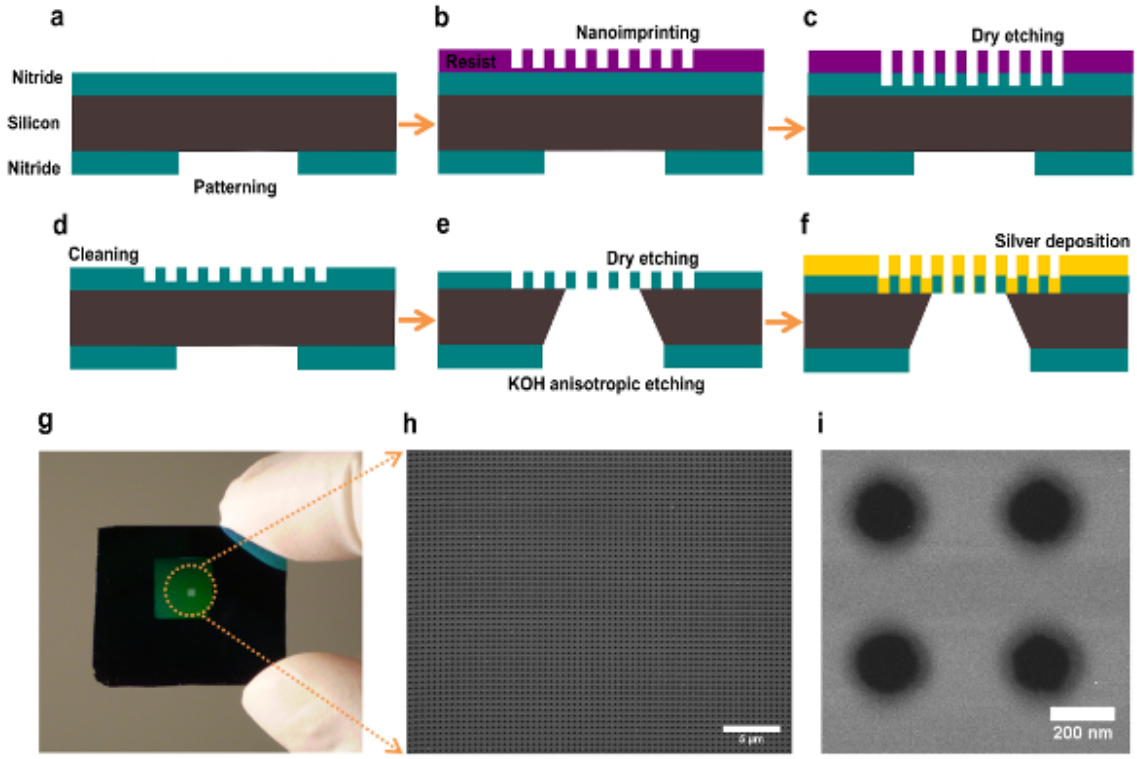

Figure 5.1. Fabrication of suspended nanohole array chip. (a) A silicon chip after 200 nm low-stress nitride deposition and photolithography to expose desired regions on the backside. (b) Nanoimprinting and dry etching was performed to transfer the nanohole array pattern to the top nitride membrane. Nanoimprint resist was then washed away. (c) Anisotropic KOH etching of silicon was used to obtain the suspended nitride membrane. A final dry-etch removed the remaining nitride from the bottom of the holes. Silver was then evaporated from the top to obtain suspended metallic nanohole arrays. (d) A 1 inch × 1 inch chip with a 1 cm x 1 cm nanoimprinted region in the center. The nanoimprinted region further has a 1 mm x 1 mm suspended membrane in the center. (Circled) (e) SEM image of the suspended membrane with nanoholes. (f) SEM shows magnified image of the individual nitride nanoholes.

approximately 200 nm in diameter and the array has a periodicity of 500 nm. Silver (thickness 120 nm) was deposited over the chips using electron-beam evaporation.

Optimization of SERS signal requires tuning of the plasmon resonances of the metallic substrate such that for a given laser wavelength, there is maximum enhancement of electromagnetic field around nanoholes. Generally, modification of the design of the plasmonic substrate such as changing the periodicity of nanohole arrays or altering the wavelength of the laser source is used for this tuning.[33, 104, 115] Here a simple method to achieve desired plasmon resonance conditions on suspended nanohole arrays was demonstrated using refractive-index-based tuning. It has been established that surface-plasmon-mediated transmission can be modulated by the refractive index at the metal-dielectric interface. In fact, the shift in transmission peaks of nanohole arrays due to change in refractive index close to the sensor surface has been used for biosensing.[76, 101-103] This intrinsic property of metallic nanohole arrays was utilized to tune the resonance peaks. Sucrose solutions of appropriate concentration were added on the nanohole array surface to shift the transmission spectra as desired and to test the evolution of SERS signal. Sugars like glucose and sucrose have been reported to be very difficult to detect using SERS owing to their small normal cross-section and negligible adsorption to bare metal surfaces.[116] This property makes them suitable to be used on a SERS substrate without adding unwanted Raman peaks.

The schematic for SERS measurement and the steps for signal optimization from the suspended nanohole array chips are illustrated in Figure 5.2a. Benzenethiol (BZT) and 4-MP were used to characterize the SERS response of the chips as these molecules are known to have large scattering cross-sections and can easily form self-assembled

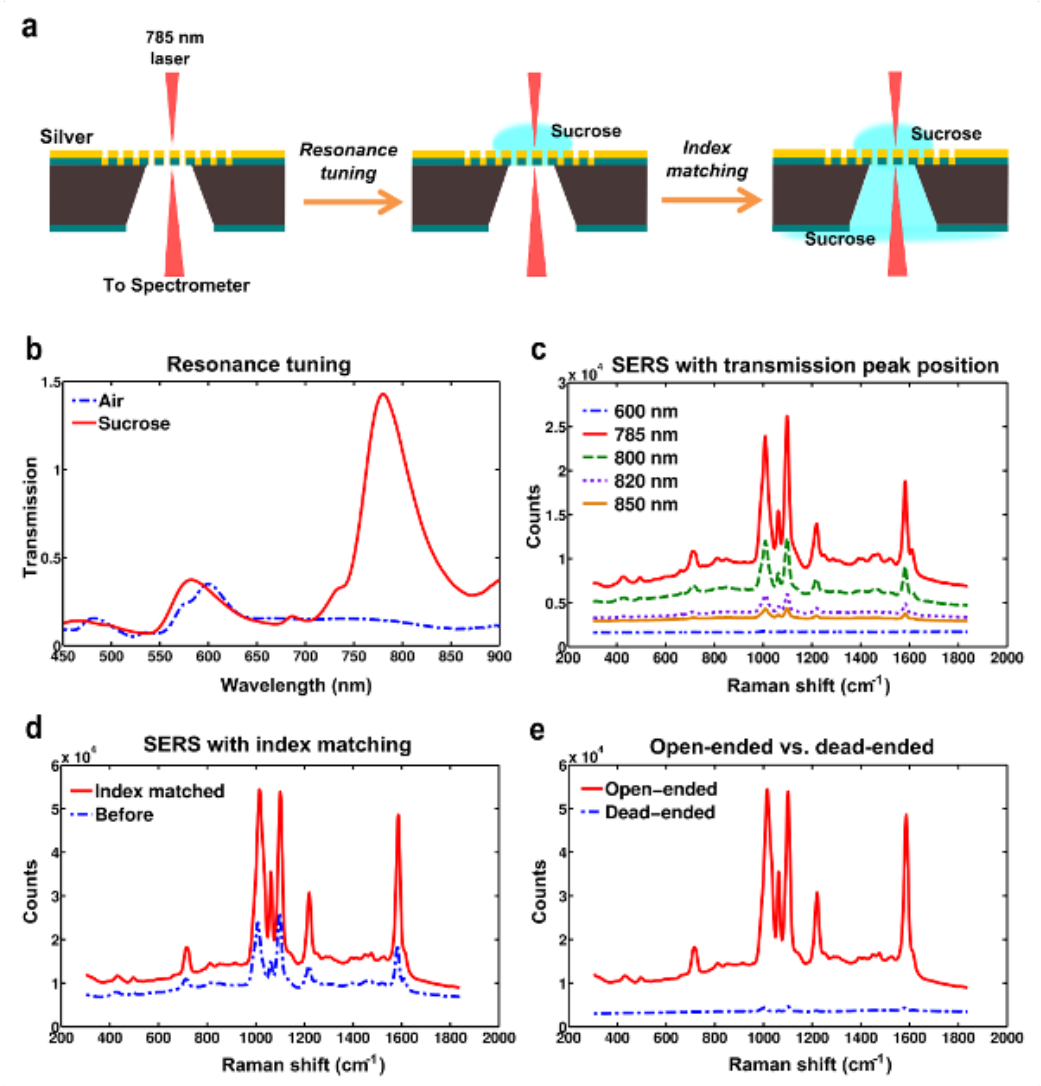

Figure 5.2: Optimized SERS from suspended nanohole arrays. (a) Schematics showing the process of obtaining SERS signal from chips with air as dielectric media, resonance tuning using sucrose to improve the signal and index matching to further optimize the signal. (b) Figure showing normalized transmission maxima at around 600 nm corresponding to (1,0) metal-air interface shifts to 785 nm after addition of desired concentration of sucrose. (c) SERS signal obtained from the same spot on the chip with transmission peak tuned to different wavelengths. (d) SERS signal obtained from the same spot before and after index matching. There is close to three times increase in signal after index matching. e) SERS signal obtained from 4-MP SAM layers on suspended nanohole arrays as compared to FIB milled dead-ended nanoholes. The signal from

suspended nanoholes is about fifty times higher than that obtained from dead-ended samples.

monolayers (SAM) owing to thiol-metal bonding on gold or silver. Chips with 4-MP SAM layer were used for the results shown in Figure 5.2. By increasing the concentration of added sucrose solution, the transmission peak can be shifted to longer wavelengths. Upon addition of approximately 1 M sucrose solution the transmission peak at 600 nm corresponding to the (1,0) silver-air interface was shifted to 785 nm (Figure 5.2b).

SERS spectra were obtained from the sample with variation in position of the transmission peak of the nanoholes (Figure 5.2c). These measurements were taken from the same spot on the sample to avoid any other sources of variation in signal. As expected, maximum SERS signal was obtained when the peak transmission wavelength of the nanoholes matched the laser wavelength at 785 nm. Upon adding the same sucrose solution to the backside cavity of the suspended nanohole array membrane, further increase (up to 300 %) in the SERS signal was observed (Figure 5.2d). It has been known that surface-plasmon-enhanced transmission through nanoholes can be enhanced up to an order of magnitude by matching the refractive index on either side of the metal film.[117]

Three-dimensional (3D) finite-difference time-domain (FDTD) simulations were performed to demonstrate the increase in the plasmonic field around the nanohole arrays with refractive-index-based tuning (Figure 5.3). In the first case, air was used as the refractive index medium and weak plasmonic hotspots can be observed at the edges of the nanoholes (Figure 3a). With the addition of sucrose and filling of the nanoholes such

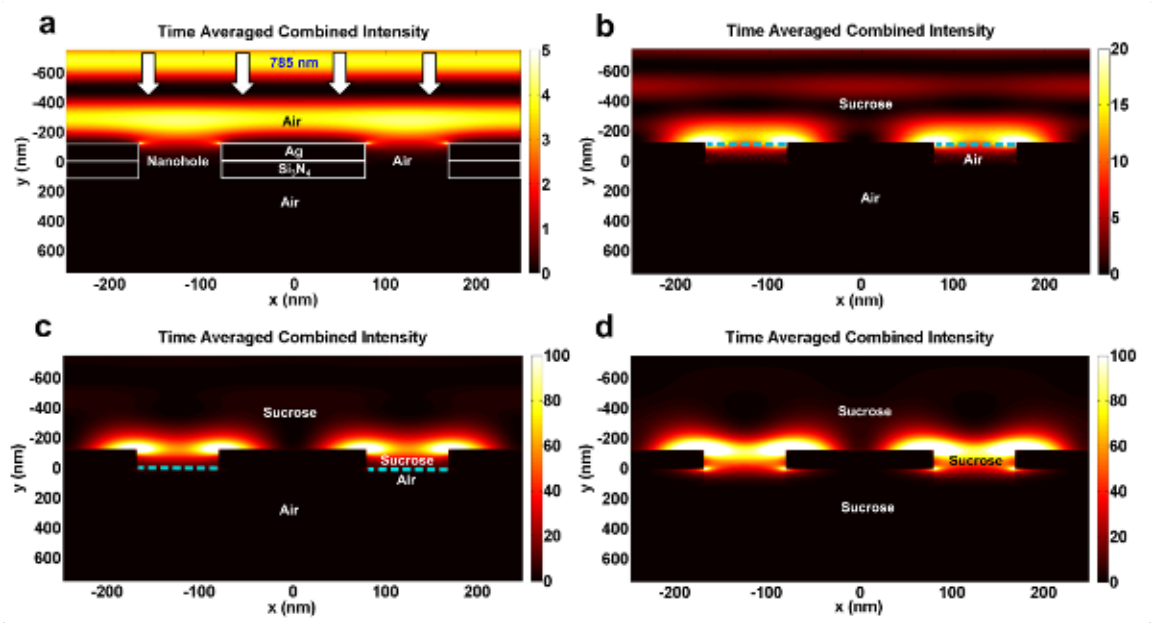

Figure 5.3: Three-dimensional FDTD simulations for suspended nanohole arrays with excitation wavelength 785 nm. Electric field intensity with (a) air as the dielectric medium around and inside the suspended nanoholes. (b) Sucrose present on top metal surface. Air present inside and at the bottom end of the nanoholes. (c) Sucrose present on the top silver surface and filling top half of the nanoholes, whereas air is present elsewhere. Concentration of sucrose is adjusted such that the transmission maxima through the nanoholes matches the excitation wavelength (785 nm). (d) Sucrose present on both sides and completely filling the nanoholes.

that the transmission maxima is in resonance with excitation wavelength (785 nm), more than an order of magnitude enhancement of the plasmonic field at the hotspots can be observed (Figure 5.3b-c). Further increase in electric field was obtained with sucrose present on both sides of the sample as well as inside the nanoholes (Figure 5.3d). The increase in electric field observed in these FDTD simulations correlates qualitatively with the measured increase in SERS signal (Figures 5.2c-d). For further comparison, samples with dead-ended hole arrays were prepared using FIB milling. 120 nm thick silver was deposited on suspended nitride membranes and nanoholes with diameter 200 nm and

periodicity 500 nm were milled through the silver but not through the nitride membrane. These samples were also placed in a solution of 4-MP overnight to form a SAM layer. To measure the SERS signal from the dead-ended hole array samples, a drop of sucrose solution was added to the substrate such that the transmission peak matches the laser wavelength. SERS signal obtained from a FIB milled dead-ended hole array sample as compared to the signal obtained from suspended nanohole array under optimized transmission conditions has been shown in Figure 5.2e. The signal obtained from suspended nanoholes was approximately 50 times higher as compared to dead-ended samples (Figure 5.2e). This difference could be attributed to combination of a number of factors including refractive index matching between the top and bottom sides of the suspended nanoholes, improved transmission, and nanoscale variations in geometry of the nanohole edges (hotspots) obtained via nanoimprinting as compared to ion milling.

Raman signals obtained from neat solutions of 4-MP and BZT were used to calculate enhancement factors for the chips. The vibration bands used for this calculation correspond to the in-plane ring breathing mode coupled to the C-S stretching for the BZT and 4-MP samples.[118] When BZT adsorbed to the silver surface, the vibration band was observed to shift from 1092 cm^{-1} to 1072 cm^{-1}. Similarly for 4-MP, the vibration band shifted from 1115 cm^{-1} in aqueous solution to 1099 cm^{-1} upon adsorbing to the silver surface. Enhancement factors of $\sim 10^7$ were obtained for the suspended nanoholes for both 4-MP and benzenethiol samples. These numbers were obtained repeatedly over multiple spots on different samples using both BZT and 4-MP as analytes. In comparison,

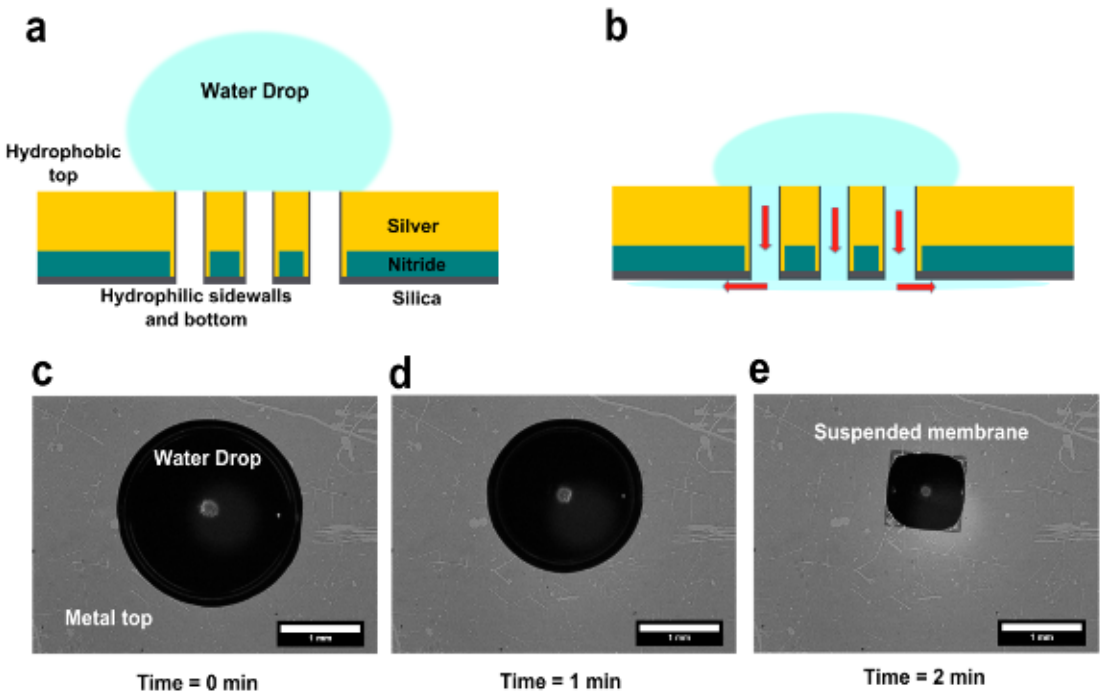

Figure 5.4: Schematic for surface-tension-induced flow through nanoholes. (a) Aqueous solution is placed over the nanoholes. The top metal surface is hydrophobic whereas silica layer within the holes and on the backside of the chip is hydrophilic. (b) Hydrophilic nanohole sidewalls suck-in the solution, driving the flow towards the back of the chip (shown as red arrows). (c-e) Bright-field images showing flow of a 2 μL drop of water through the suspended nanohole array within 2 minutes. The water drop shrinks as it is sucked in through the hydrophilic nanohole sidewalls.

previous studies on nanohole array SERS[33, 104, 106] have reported EFs in the range of 10^4-10^5. This improvement in the EF values (~ 100 times) confirms that suspended nanohole arrays can be used as excellent SERS substrates.

Nanohole-based biosensors with integrated flow-through fluidics can provide one route to overcome diffusion-limited transport of analytes improving the detection time and detection limit of the sensor.[10, 11] To facilitate the flow-through process, silica (30

nm), which is hydrophilic, was deposited on the backside of the chips using electron-beam evaporation. As this deposition technique is highly directional, the sidewalls of the nanoholes, which lie parallel to the direction of evaporation, were coated with a much thinner layer of silica. The addition of the silica layer on the opposite side of sample injection drastically altered the flow properties of the chip. Figure 5.4 shows the schematic of chips with silica on the backside, and a hydrophobic top surface. When an aqueous solution of analyte or particles was placed on the top of the chip, flow through the nanoholes was initiated as soon as the solution came into contact with the hydrophilic inner walls. The solution then flowed and spread on the back surface of the chip. Figure 5.4(c-e) show snapshots of the flow in process, where a 2 μL drop of water disappears through the nanohole membrane within 2 minutes. For membranes of size 1 mm^2, an approximate flow rate of 1 μL/min was obtained.

The effect of flow-through concentration as compared to diffusion-limited adsorption or evaporation-driven concentration over suspended nanoholes was visualized using fluorescent 2 μm polystyrene beads. In Figure 5.5, the accumulation of polystyrene beads (10^6 beads/mL) was compared for three cases: I) where the holes were dead-ended, II) where the holes were open and concentration was driven by evaporation through the open-end of the nanoholes and III) holes were open and silica was deposited on the backside leading to flow and concentration. Schematics for cross-section of a single nanohole accompany the fluorescence images for each of the three cases in Figures 5.5(a-c). During the evaporation of a liquid drop on a surface, evaporation of solution from the

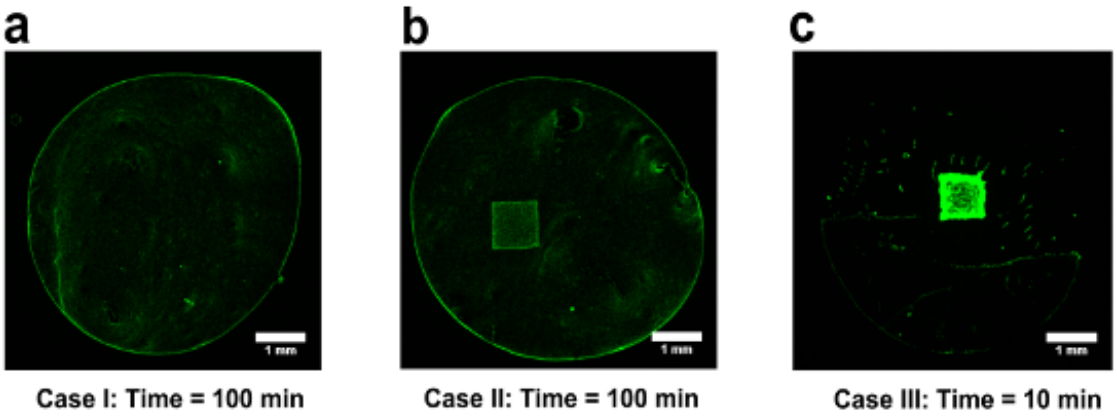

Figure 5.5: Bead concentration and time taken for consumption of solution over nanohole arrays for three cases. (a) Case I: Accumulation of 2 μm polystyrene beads after evaporation of a 10 μL drop over dead-ended nanohole arrays. The schematic shows cross-section of a single dead-ended nanohole for this case. (b) Case II: The same experiment performed over suspended nanohole arrays with metal-coated (hydrophobic) sidewalls. Evaporation from open end of nanoholes promotes directed flow and concentration. (c) Case III: These samples had silica deposited on the back surface and sidewalls resulting in surface-tension-directed flow.

pinned outer edges generates an outward flow and concentrates particles at the edges. This phenomenon, known as the 'coffee stain effect',[86] is clearly visible in Figures 5.5(a) and (b). The particles were randomly distributed within the area of the drop, as shown in Figure 5.5(a), as their position was determined by diffusion and the outer flow. In case II, open-ended holes with no silica also promoted evaporation-based localized flow and accumulation of particles over the nanohole array was obtained. There was no significant difference in the time scales of evaporation for cases I and II. For case III (open-ended holes with silica), the flow was based on surface tension and the time scale was an order of magnitude less than evaporation-based methods. This case demonstrates significantly

higher concentration as most of the solution was directed to flow through the nanoholes improving particle aggregation over the holes (Figure 5.5c). Absence of prominent outer ring for the drop indicates the dominance of nanohole directed flow and the relatively shorter time scale of the process.

These results illustrate that surface-tension-induced flow through nanoholes promotes the most efficient concentration of particles and is at least an order of magnitude faster as compared to evaporation-based techniques. This principle can also be utilized for overcoming diffusion-limited interaction of analytes with the nanoholes for plasmonic sensing. For small analyte molecules, the passive flow generated by surface tension forces drives them to pass within less than 100 nm (radius of the nanoholes) of the hotspot i.e. edge of the nanoholes and the nanohole sidewalls. This short distance can be easily overcome by diffusion of analyte molecules increasing the probability of the analytes adsorbing on or close to the plasmonic hotspots, which can lead to enhancement of Raman signal of analytes. The 4-MP molecules, which have a thiol group, can be captured on the nanohole array substrate through formation of covalent thiol-silver bonds. The molecules may also get physically adsorbed to silica layered regions inside the nanoholes through van der Waals forces.

To demonstrate the advantage of flow through the nanoholes over diffusion-based transport for SERS sensing, experiments were performed using nanohole substrates prepared in two different ways. In the first case, 20 μL of 100 nM 4-MP solution was allowed to completely flow through suspended nanoholes in about 20 minutes. For

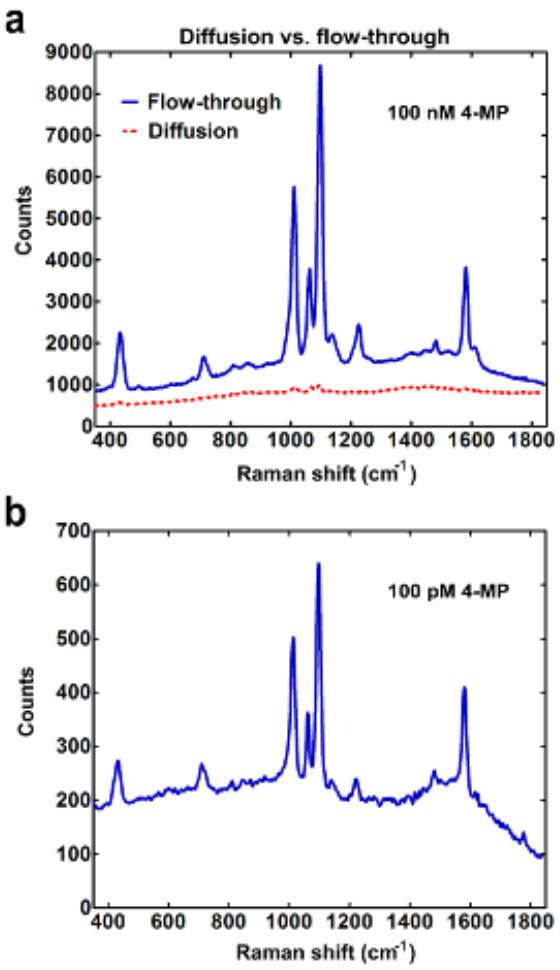

Figure 5.6: SERS with surface-tension-induced flow-through. a) Comparison of SERS spectra obtained from flow-through of 100 nM 4-MP (red spectrum) as compared to diffusive transport (blue). b) SERS spectra obtained after flow through of 100 pM 4-MP for an hour.

diffusion-based adsorption, substrates were submerged in a reservoir containing identical 4-MP solution for the same amount of time. SERS signal obtained from both the samples has been shown in Figure 5.6(a). Samples with surface-tension-induced flow gave about 50 times higher signal as compared to diffusion-limited adsorption. The experiment was

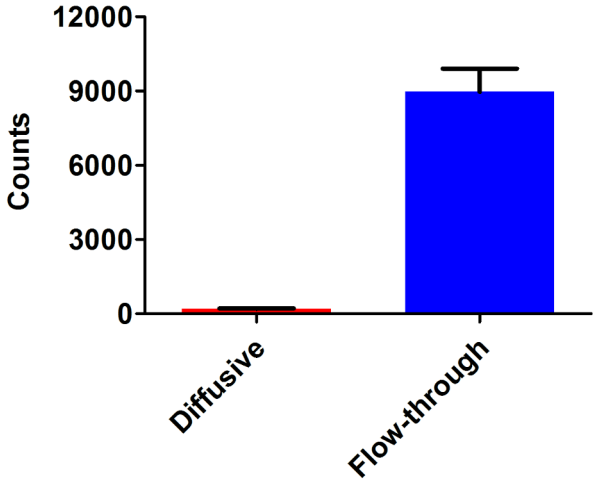

Figure 5.7: Improved SERS signal after flow-through. Comparison of SERS signal obtained from flow-through vs. diffusion-dependent adsorption of 100 nM 4-MP on suspended nanohole array substrates over three rounds of experiments.

repeated over multiple sets of samples and similar results were observed (Figure 5.8). To demonstrate detection of low concentration samples, 50 µL of 4-MP at a concentration of 100 pM (i.e. 5 femtomoles of 4-MP) was allowed to flow through the sample for about an hour. SERS signal collected from this sample shown in Figure 5.6b demonstrates the capability of the method to detect low concentrations of analyte molecules. The high sensitivity in this case results from the combination of two factors: large Raman enhancement factor of the nanohole array substrate and flow-through-based concentration of molecules at the hot spot.

The limit of detection of the setup, in terms of 4-MP concentration, will be dependent on the duration of time the solution is allowed to flow through the nanoholes. However it can be estimated in terms of number of molecules of 4-MP in solution. Using

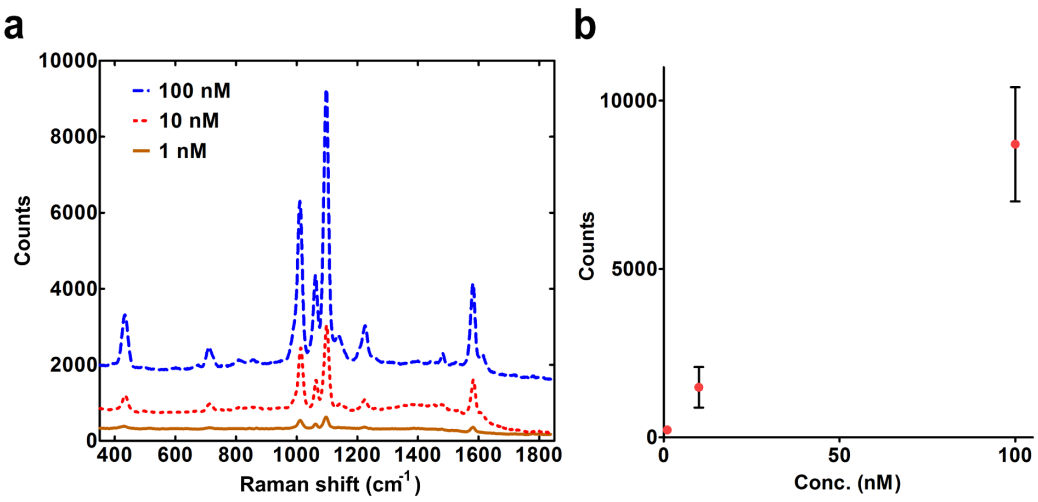

Figure 5.8: SERS signal vs. concentration. (a) 20 μL 4-MP solutions of varying concentrations were added to the samples and Raman signal was measured. (b) Signal intensity for the peak corresponding to 1099 cm^{-1} with varying 4-MP concentration.

the peak at 1099 cm^{-1} in the SERS signal shown in figure 5.6b, the signal-to-noise (S/N) ratio was calculated to be approximately 55. Assuming a linear concentration vs. signal response (Figure 5.9), and calculating for a final S/N ratio of 3 gave us a limit of detection of approximately 272 attomoles of 4-MP molecules in solution.

5.4 Conclusion

This chapter has demonstrated the fabrication of millimeter-sized suspended metallic nanohole arrays using NIL and their potential for flow-through SERS. Refractive-index-based tuning with sucrose solution was implemented on this suspended nanohole array substrate for optimized SERS.. This tuning method was utilized to match the plasmon resonance peaks with the excitation laser wavelength. Sucrose solution was used because it has very weak intrinsic Raman signal and therefore doesn't contribute

detectable background to the measurements. This simple tuning method can also be utilized for plasmon-enhanced fluorescence[77, 119] where the plasmon resonance can be tuned based on the excitation or emission spectra of the fluorescent species. Furthermore, this technique can easily be translated to other plasmonic substrates utilizing the principle that by changing the refractive index of the dielectric medium around the metal, plasmon resonance conditions can be changed to optimize the detection of optical signal from analyte molecules. The suspended Ag nanohole arrays have SERS enhancement factor in the order of 10^7, which is two orders of magnitude greater than those reported previously for nanohole arrays and compares well with other commonly used SERS substrates. Demonstration of high SERS enhancement factor from nanohole arrays can open up many possibilities, because the nanohole geometry enables trapping of biomolecules and small particles,[80, 120] formation of model membranes such as suspended lipid bilayers,[103, 121-123] as well as flow-through sensing to overcome the diffusion limit.[10,11, 24-26] To combine nanohole-enhanced SERS with flow-through sensing, surface-tension-induced passive flow was used and particles were concentrated over the nanohole arrays. Passive flow rates of around 1 μL/min were obtained using this technique. This passive flow reduced the time required to consume the solution while bringing the analyte molecules closer to the plasmonic hotspots. The presented device design utilizing passive flow obviates the use of a bulky external pump and fluidic interconnects, thus improving the simplicity and portability of the process. Thus the simple and novel resonance tuning as well as passive flow-through technique discussed here on a suspended nanohole array

platform can help alleviate the mass transport limitations and benefit wide applications in optofluidics.

Chapter 6

Magnetic force-driven transport

Adapted from Kumar, S., Johnson, T. W., Wood, C., Qu, T., Wittenberg, N. J., Otto, L.M., Shaver, J., Long, N. J., Victora, R., Edel, J. B., and Oh, S.-H. Template-stripped multifunctional wedge and pyramid arrays for magnetic nanofocusing and optical sensing (submitted for publication). This work was done in collaboration with other members of Oh group (computer simulation plots by L. Otto), Prof. R. Victora's group at the University of Minnesota and Prof. J. Edel's group at Imperial College, London. Prof. Victora's group handled the derivation of analytical formula. Prof. Edel's group assisted with 30 nm nanoparticle trapping data.

In previous chapters platforms and techniques have been discussed, where the flow of solution is diverted towards nanoscale plasmonic hotspots without the application of any external force. In this chapter an alternative approach is utilized, where plasmonic nanostructured substrates are fabricated with integrated magnetic layers. The potential of these structures towards directed and localized capture of analytes-tagged to magnetic nanoparticles and their concurrent optical detection has been discussed in this chapter.

6.1 Introduction

The distribution of electromagnetic fields around nanostructures can be greatly influenced by their shape.[124, 125] Electrostatic fields near sharp conducting tips or edges exhibit a singular behavior owing to the 'lightning rod' effect.[126] Electromagnetic fields can also be tightly confined at sharp tips made with noble metals by "nanofocusing" incident free-space light via surface plasmons.[127, 128] Magnetic fields around a sharp ferromagnetic tip can far exceed the saturation magnetization of the material, leading to singular behavior near infinitely sharp tips.[129] When such ferromagnetic tips are coated with gold or silver shells, it is possible to combine strong magnetic fields with plasmonic effects. Therefore, optimal design and fabrication of sharp magnetic tips are highly desirable, yet reproducible high-throughput fabrication methods have been difficult to achieve.

Among many potential applications, biosensing can greatly benefit from the aforementioned combination of enhanced magnetic and optical fields. One of the major problems in surface-based biosensing is diffusion-limited transport of analytes to the

sensing surface,[7, 36, 130] which increases the time taken for detection and reduces the sensitivity for low-concentration analytes. Directed transport of analytes to the sensor surface via selective surface functionalization,[107] passive flow[131, 132], or actively using pressure-driven flow,[8] electrokinetic,[9, 133] or magnetic methods[134] can improve detection sensitivity and speed. Among various options, magnetic forces can work well with complex media, including conductive and non-transparent solutions like blood, enabling biomedical diagnostics. The localization and enhancement of the magnetic field gradient are of great practical importance for rapid isolation and concentration of cells or biomolecules,[42, 135, 136] which are usually tagged to magnetic beads. The ability to run multiple tests simultaneously is also important, which requires large-area substrates with arrayed sensing regions. While magnetic tips have been produced for MFM applications,[137] the fabrication method is slow and expensive, and integration with large-area substrates for array-based particle manipulation and sensing is not straightforward. Realization of the potential of sharp magnetic tips for the enhancement of magnetic fields along with field gradients requires fabrication techniques that can reproducibly generate structures with nanoscale features at precise locations over large areas.

Template stripping has emerged as a practical technique to mass-produce sharp metallic wedges and pyramids with high reproducibility.[138-140] The key advantage of this approach for tip fabrication is to use crystalline-orientation-dependent wet etching of silicon wafer templates[141] to produce inverted pyramids or wedges with extremely sharp corners (~10 nm radius of curvature) without using high-resolution lithography. After

template fabrication, noble metals such as gold or silver can be deposited to form sharp tips, which can be stripped using adhesive backing layers due to poor adhesion between noble metals and oxidized silicon surfaces. To date, template stripping of coinage metals (Au, Ag, Cu),[139] refractory metals (W, Ta),[142] and oxides (TiO_2, ITO)[142] has been shown. While colloidal pyramidal nickel particles have been fabricated using sacrificial templates, the magnetic particles required collection from aqueous media in clumps by dissolving the template.[138, 143] This restricts further application of such colloidal nickel particles for investigation of tip-enhanced magnetic fields and magnetic trapping.

In this chapter, the generation of localized, extremely strong magnetic fields and field gradients using template-stripped nickel wedges and pyramids is demonstrated using analytical equations, numerical simulations, and experimental evidence. Analogous to the electrostatic lightning rod effect, the equations show that as a magnetic tip or wedge becomes infinitely sharp, the field at the tip diverges. To study such effects, a template-stripping technique was used to produce sharp nickel tips with gold or silver shells from a reusable silicon template. The gold or silver-coated nickel structures can be used for trapping magnetic nanoparticles with nanoscale control over large areas and analysis like SERS.

6.2 Methods

6.2.1 Fabrication of sharp nickel wedge and pyramid arrays

To create a silicon template for wedges, standard (100) silicon wafers were coated with 200 nm-thick low-stress silicon nitride (Si_3N_4) using low-pressure chemical vapor

deposition (LPCVD). Then photolithography and dry etching were used to remove nitride from the front of wafers to obtain rectangle-shaped areas with exposed silicon. The wafers were then dipped in a KOH bath where the silicon was anisotropically etched to obtain wedge-shaped grooves in silicon wafers (Figure 6.1a). The process for fabricating silicon templates with pyramid-shaped grooves has been described in previous work.[140] A layer of gold or silver (thickness 10 to 50 nm) followed by a layer of nickel (thickness 125 nm) were deposited on the wafers using electron-beam evaporation (Figure 6.1b). The gold-nickel bilayer films were then template-stripped using optical adhesive (NOA 61, Norland Products, Inc.) and attached to a glass slide (Figure 6.1c).

6.2.2 Numerical simulations

COMSOL Multiphysics^{TM} 4.4 was used along with the AC/DC module (magnetic fields, no currents) to perform numerical simulations of several models relating to the analytical calculation and experimental conditions. A 2D approximation of wedge was used. A Gaussmeter (GM 2, Alphalab Inc.) was used to experimentally measure the strength of the NdFeB magnet (ND040-52NM-4C, CMS magnetics, cylindrical shape with 0.5 inch diameter and 0.5 inch height) that was placed below the wedges and pyramids during experiments. The external magnetic field B was measured to be 4300 G (or 0.43 T) 1 mm above the surface of the magnet to account for the thickness of the glass slide on which the wedge and pyramids were template stripped. This magnetic field value was applied to the model by creating a magnetic potential drop vertically across the modeling region. The nickel material was modeled using a BH curve from the available

non-linear magnetic materials in version 4.4. The external material (representing water, optical adhesive, and gold) was modeled as $\mu_r = 1$.

6.2.3 Synthesis of silver-coated magnetic polystyrene beads

Silver-coated magnetic polystyrene beads were synthesized using a polyol reduction method with minor modifications.[1] Magnetic polystyrene beads (300 nm diameter) were obtained from Spherotech (FCM-02556-2). A small sample of beads (100 µL) were pelleted from their initial suspension (1 % w/v) using a 0.5 inch diameter neodymium magnet (CMS Magnetics), then resuspended in ethylene glycol. This process was repeated, then the beads were suspended in 125 µL of ethylene glycol containing 0.25 M $AgNO_3$ and 0.35 mM polyvinylpyrrolidone-40 (PVP-40). The bead suspension was vigorously mixed with a vortex mixer then placed in an oven at 100 °C for 20 hours with intermittent vortexing. After 20 hours the beads were vortexed, then sonicated for 3 minutes in a bath sonicator at room temperature. The beads were separated from the reaction solution by magnetic pelleting followed by discarding of the supernatant. Next the beads were resuspended in 300 µL of ethanol, triturated with a 100 µL Eppendorf pipette and vortex mixed. This process was repeated twice more, then 700 µL of ethanol was added to make a 1 mL suspension of silver-coated magnetic polystyrene beads.

6.2.4 Functionalization of silver-coated magnetic polystyrene beads

The silver-coated beads were functionalized with 4-mercaptopyridine (4-MP) as follows. In a small Eppendorf tube 180 µL of the silver-coated beads were mixed with 20 µL of a 20 mM 4-MP solution in ethanol, resulting in a final 4-MP concentration of 2

mM. The beads were incubated in this solution overnight, then washed 3 times by magnetic pelleting, discarding of supernatant, and resuspension in 200 μL of ethanol. The beads were then transferred to aqueous solution by magnetic pelleting, discarding of supernatant and resuspension in deionized water. This process was repeated two more times.

6.3 Results and discussion

The process for fabrication of sharp nickel wedges and pyramids using a template-stripping process has been shown in Figure 6.1(a-c). Glass slides (thickness 1 mm) with arrays of sharp metallic wedges or pyramids were obtained. A scanning electron micrograph (SEM) of an array of wedges is shown in Figure 6.1d. Another SEM shows a bird's eye-view of array of wedges (Figure 6.1e). A zoomed-in side-view of one of the wedge tips can be seen in Figure 6.1f. The radius of curvature of the tip measured by SEM was approximately 10 nm. Such sharp tips were observed for 10 as well as 50 nm of deposited gold. The radius of curvature of the tip measured by SEM was approximately 10 nm. Such sharp tips were observed for 10 as well as 50 nm of deposited gold. Pyramids were similarly fabricated using silicon molds with pyramidal trenches (Figure 6.1g,h).

On account of nickel having ferromagnetic properties, the substrate can be magnetized under the influence of an external magnetic field. Substrates were magnetized using a Neodymium Iron Boron (NdFeB) magnet (ND040-52NM-4C, CMS magnetics, cylindrical shape with 0.5 inch diameter and 0.5 inch height). The degree and nature of

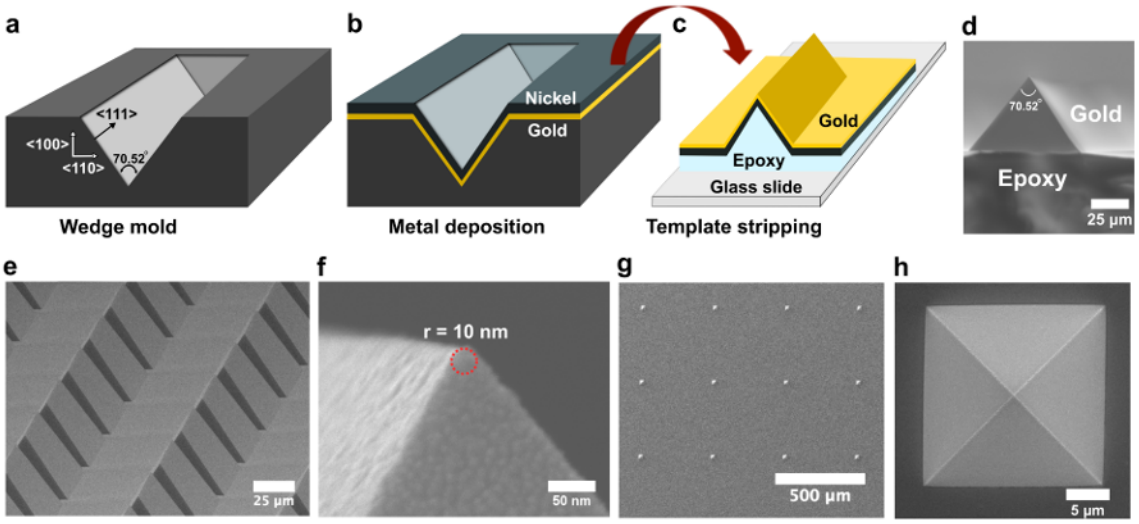

Figure 6.1: Fabrication scheme and images of magnetic wedges and pyramids. a) Trenches in the silicon template formed using anisotropic etching of <100> silicon wafer in KOH. b) Thin layer of gold followed by nickel deposited on the template using electron-beam evaporation. c) Optical adhesive (NOA61) was added to the template and a glass slide was placed on top. The sample was then placed under ultraviolet light for curing. The metal film attached to epoxy and glass slide was template-stripped. SEM images showing d) cross-sectional view of a template-stripped wedge. e) bird's eye view of arrays of wedges. f) side-view of the tip of a wedge with 10 nm radius of curvature. This wedge had 50 nm gold deposited on top of 125 nm nickel film. g) Widely-separated array of pyramids fabricated using a pyramidal silicon template. h) Top-down view of a template-stripped pyramid.

magnetization of the fabricated structures by the external magnetic field was explored using analytical calculations and computer simulations. First, an analytical formula was derived describing the magnetic field for an infinitely long 2D wedge with an infinitely sharp tip for the region near the tip. The cross-section of the wedge was a triangular shape with magnetic metal thickness at the tip region t, which is small compared to the base width of the triangle, as illustrated in Figure 6.2a.

We used the first-order Taylor expansion to obtain the magnetic scalar potential Φ_m, and the magnetic field component along the y axis, H_y.[126] For uniform saturation magnetization, the contribution to the field is only from the surface.

$$\Phi_m(0,b,0) = \frac{M\sin(\beta)}{4\pi}\oint \frac{\partial(x^2+(y-b)^2+z^2)^{-\frac{1}{2}}}{\partial y}\,t\,dS \qquad (\mathbf{1})$$

$$\mathrm{H}_y(0,b,0) = -\frac{\partial\Phi_m}{\partial b} = M\sin(\beta)\frac{w(b+w\cot(\beta))}{\pi b(w^2+(b+w\cot(\beta))^2)}t \qquad (\mathbf{2})$$

where b is the distance of the observation point from the tip, w is the half-width of the base of the triangular structure, β is the wedge half-angle, t denotes thickness of the wedge, M is the magnetization magnitude of the wedge, and H_y is the magnetic field strength normal to the base of the structure. For points in the regions very near the tip, $b << w$.

$$\mathrm{H}_y(0,b,0) = \frac{Mt\cos(\beta)\sin^2(\beta)}{\pi b} \qquad (\mathbf{3})$$

Using the parameter values from these fabricated wedges, assuming the magnetization to be saturated (483,000 A/m) in the vertical direction from the tip, and adding the background field from the NdFeB magnet (342,000 A/m), magnetic field strength H_y was calculated as a function of distance as shown in Figure 6.2b. The magnetic field rapidly decreases and is inversely proportional to the distance from the tip.

It should be noted that for an infinitely sharp 2D wedge, the magnetic field H_y diverges at the tip ($b = 0$), even though the saturation magnetization and thus the effective

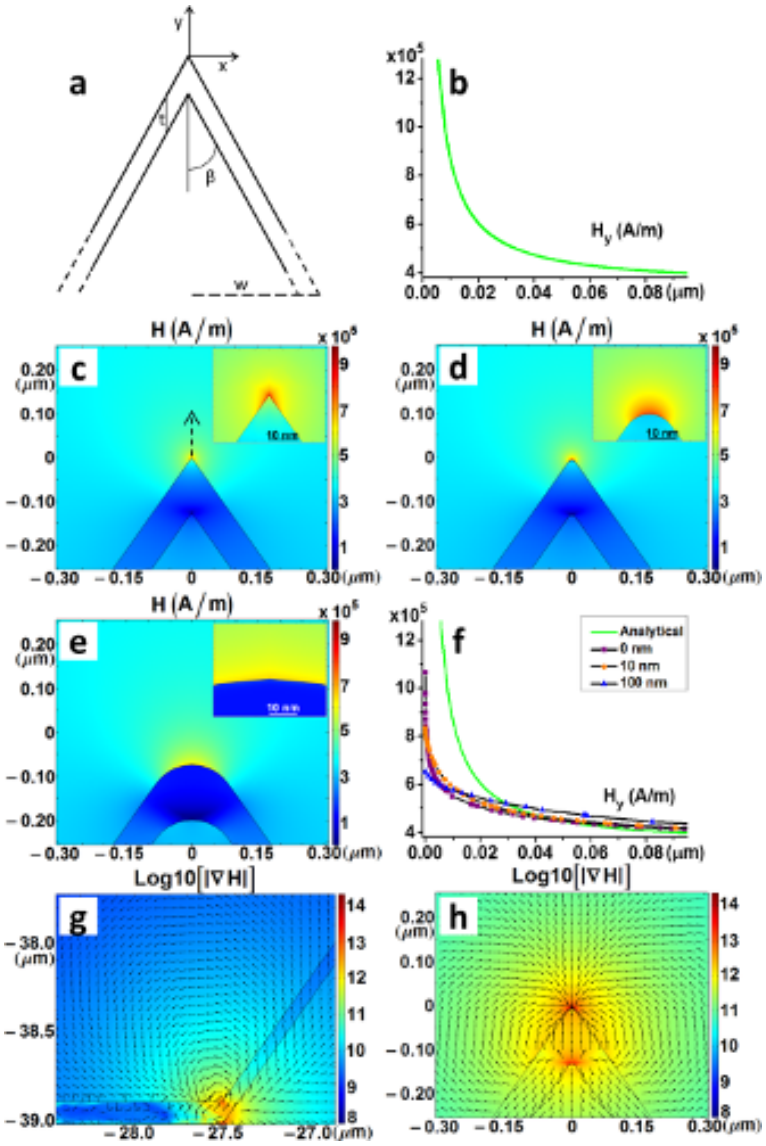

Figure 6.2: Analytical calculations and computational modeling results. (a) A schematic of the 2D wedge and (b) a graph of H_y as a function of the distance from the tip along the y-axis resulting from Equation 3 + the background H field (342,000 A/m). COMSOL field maps of H in the region near the wedge tip with radius (c) 0 nm, (d) 10 nm, and (e) 100 nm. Insets show the area within ~30 nm of the tip. (f) H_y as a function of the distance from the tip along the y-axis for both the analytical result + the background H field (342,000 A/m) and the modeling results corresponding to (c-e) (plotted along the arrow shown in (c)). An order of magnitude map of $|\nabla H|$, which is proportional to the

strength of the force acting on a particle, is shown in (g) near the base of the wedge and (h) near the 10 nm tip of the wedge. The arrows show the direction of the force.

magnetic surface charge is finite. Similarly, we can also obtain the analytic form for a 3D cone with triangular cross section, which can approximate the pyramidal tip produced via template stripping. For points very near the tip, $b << w$.

$$\mathrm{H}_y(0, b, 0) = \frac{Mt\cos(\beta)\sin^2(\beta)}{b} \qquad (\mathbf{4})$$

Comparison of Eq. 3 and Eq. 4 shows that a perfectly cone-shaped 3D tip can generate a maximum field that is π times larger than the 2D wedge tip for the same tip half-angle β. For template-stripped wedges and pyramids, the tip half-angle β is fixed at 70.52/2≅35.3°, which is determined by the crystallographic orientation of {111} facets in silicon.[141]

To better understand the behavior of the magnetic field around the fabricated wedge structures, which has a finite radius of curvature, COMSOL Multiphysics™ software was used to perform numerical simulations. 2D models were created to simulate a wedge structure with varying tip radii. A 0 nm-radius tip was modeled for comparison with the analytical model, a 10 nm-radius tip was modeled to represent the experimental conditions, and a 100 nm-radius tip was modeled for comparison with a blunt tip. Maps of the resulting fields *H* are shown in Figures 6.2c-e and become progressively weaker near the tip as the radius becomes larger (i.e. the tip becomes more blunt). The dependence of H_y on the vertical distance from the tip can be seen in Figure 6.2f for all

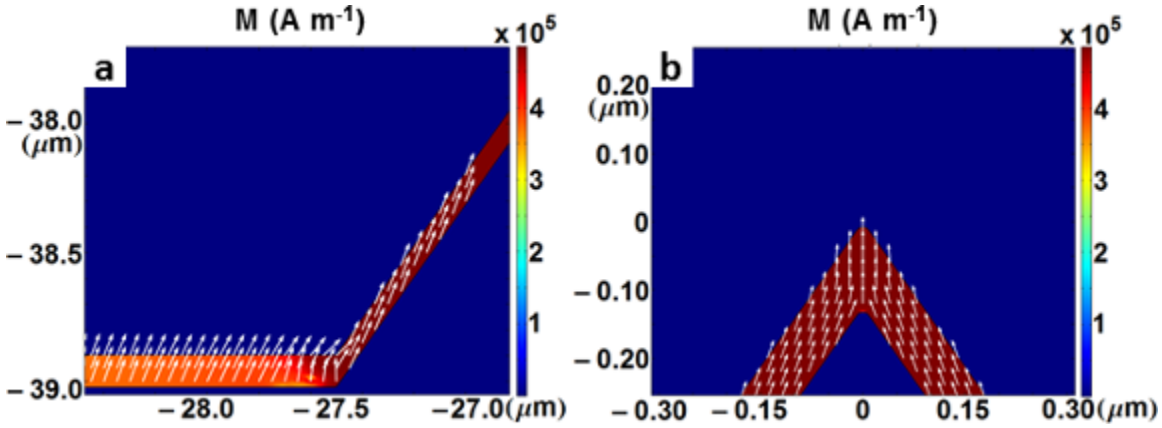

Figure 6.3: Magnetization of the nickel wedge (a) near the base and (b) near the tip. The saturation value of 4.83×10^5 A m^{-1} was reached in the wedge region, although the direction of the magnetization is still somewhat in-plane due to shape anisotropy effects.

the three cases as well as the analytical case, after including the background field from the NdFeB magnet (342,000 A/m), which is still present in experiments. The numerical calculation for 0 nm radius suggests divergent behavior, but the power dependence of H_y on y differs from the analytic result, presumably owing to the usual numerical problems near a divergence and the lack of perfectly vertical magnetic saturation in the wedge (Figure 6.3).

Further calculations were performed to determine the effect of the tip geometry on the magnetic field gradient, ∇H. The tip and base regions of the wedges and pyramids have a high spatial gradient, which upon magnetization of the substrate, translates into a highly localized and strong magnetic field gradient. A base 10 logarithmic plot of ∇H generated for a 2D wedge model shows intense magnetic field gradient zones near the tip

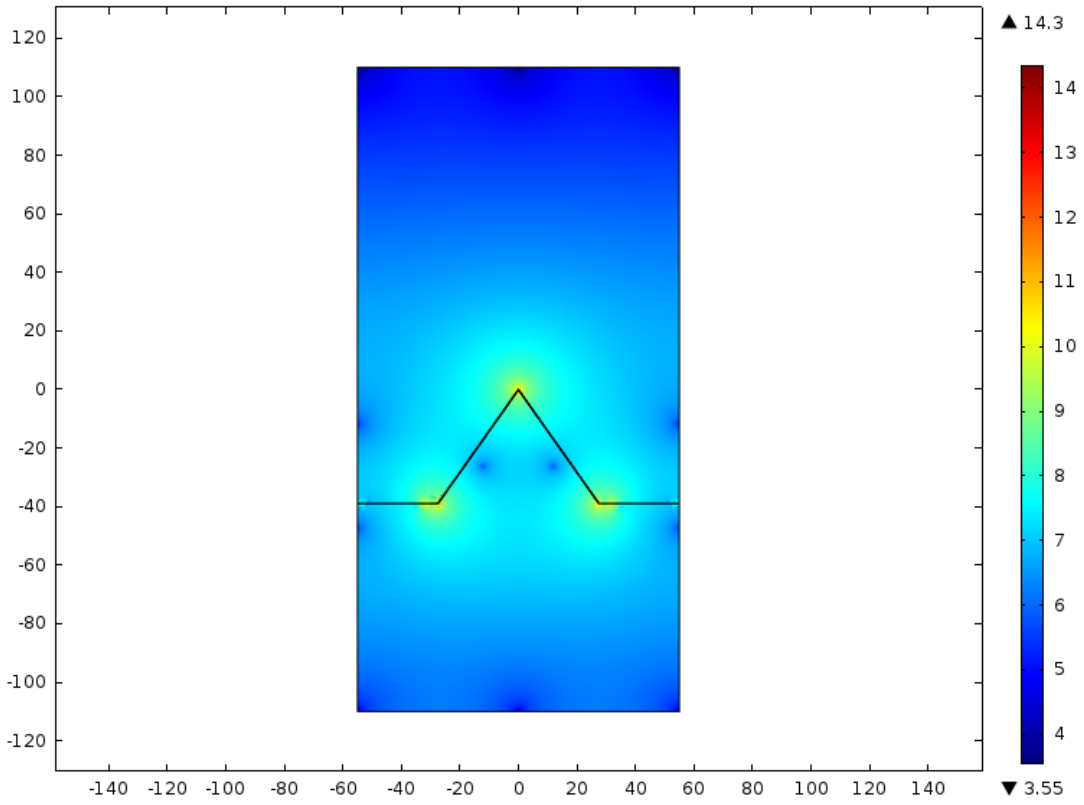

Figure 6.4: Plot of ∇H around a wedge. Order of magnitude plot of ∇H for a wedge with 10 nm tip radius showing the entire modeled area.

and base regions (Figures 6.2g,h). Orders of magnitude difference in $|\nabla H|$ close to the wedge base and tip as compared to neighboring regions can be seen in Figure 6.4. The arrows indicate the direction of force experienced by a magnetic particle in the vicinity.

Localized and intense magnetic field gradient near the sharp tips of these nanostructures can be used for rapid and directed capture of magnetic particles. Calculations based on the magnetic field gradient values obtained from computer simulations were used to realize the ability to capture magnetic nanoparticles on these substrates. Even though the substrates can be fabricated with top metal layer thickness as

low as 10 nm, the calculations and trapping experiments were performed for a system which is more relevant for plasmonic sensing i.e. 50 nm gold or silver on top of nickel. Substrates with minimal top metal layer covering the nickel should improve the trapping efficiency of the system, as the magnetic field and field gradient values decrease the further we move away from the nickel tip. However, thicker noble metal films are usually needed on plasmonic substrates for efficient propagation of surface plasmon polaritons (SPP) on the surface, which have a penetration depth of approximately 30 nm in gold or silver films in the visible wavelength regime.[19] Hence, calculations were performed for trapping of magnetic nanoparticles (300 nm and 30 nm diameter) on substrates with 50 nm gold or silver as the plasmonic shell.

The force on a particle with magnetic dipole $\boldsymbol{m}$ in a magnetic field can be written as:

$$\mathbf{F} = \mu_0 \nabla(\boldsymbol{m} \bullet \boldsymbol{H}) \qquad (\mathbf{5})$$

Where $\mu_0$is the permeability of the surrounding medium (in this case, gold and a water solution where the relative permeability ~1). Since these nanoparticles are known to be superparamagnetic for an applied magnetic field of 0.43 T (field measured from the NdFeB magnet), the magnetic dipole is assumed to be saturated where $\boldsymbol{m}$ is constant and parallel to H, so we can rewrite Eq. 5 as:

$$\mathbf{F} = S\mu_0\mu_B \nabla H \qquad (\mathbf{6})$$

Where S is the number of Bohr magnetons, μ_B. ∇H was determined from the numerical simulations (Figure 6.2h) to have a value of ~10^{12} A/m^2 in the downward direction in the region 50 nm above the tip (next to the gold), which is where the edge of a trapped particle would be located. For the 300 nm particles (FCM-02556-2, Spherotech), the composition was 12% γ-ferric oxide (γ-Fe_2O_3) by volume, which yielded $S \sim 1.5\times10^8$ Bohr magnetons per particle assuming 2.2 Bohr magnetons per Fe atom. As a reference, the threshold force necessary to overcome Brownian motion for the 300 nm particles was determined to be $F_{th} \sim (k_B T / 2r_p)$ = 14 fN (k_B is Boltzmann's constant, T is the temperature (300 K), and r_p is the particle radius) whereas the force experienced by the beads 50 nm above the nickel tip was 1700 pN, thus demonstrating the simple capture of the 300 nm particles. As a rough approximation for the 30 nm particles (Nanocs Inc.), the Fe_2O_3 properties were assumed to be the same as for the 300 nm particles and estimated the threshold force to be 0.14 pN and the applied force to be 1.7 pN. These calculations show that even with 50 nm gold or silver layer on top of the nickel, the tip-enhanced magnetic field gradient generated by these structures should allow trapping of these nanoparticles.

For tip-enhanced magnetic trapping experiments, a drop of water containing suspended fluorescently-tagged magnetic beads was placed on the glass substrate on top of the template-stripped wedge or pyramid region. Magnetic particles of various sizes (1.6 μm, 300 nm, and 30 nm) were used for these experiments. The setup was placed on an upright microscope stage and a magnet was brought in contact with the bottom surface

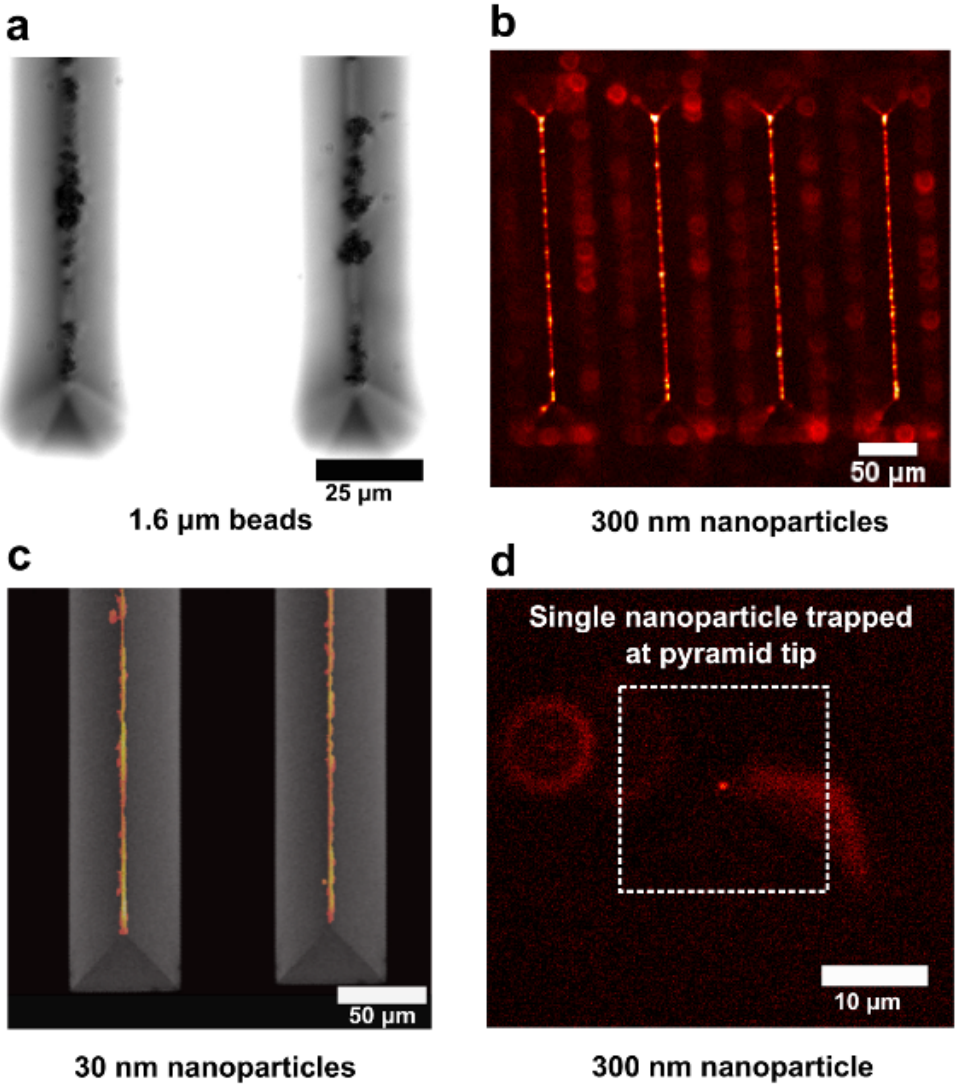

Figure 6.5: Tip-enhanced trapping of magnetic beads. a) Bright-field image showing captured 1.6 µm beads captured on tips of wedges. b) Fluorescence images showing 300 nm nanoparticles captured on sharp wedge tips. c) Fluorescence image showing 30 nm magnetic nanoparticles captured on sharp wedge tips. The image has been overlaid on top of a SEM of the wedges. d) Fluorescence image showing capture of a single 300 nm magnetic nanoparticle at the tip of one such pyramid under the influence of a magnetic field.

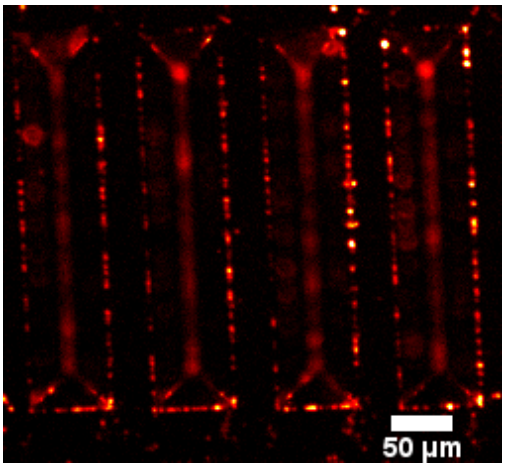

Figure 6.6: Trapping of magnetic nanoparticles at sharp bases. Fluorescence image showing 300 nm magnetic nanoparticles trapped along the sharp bases of magnetic wedges.

of the glass. The larger particles (1.6 µm and 300 nm) were trapped within seconds of application of external magnetic field. The rough calculations showed that the applied magnetic force for the 30 nm nanoparticles was within about an order of magnitude to their threshold trapping force. Images for these beads were collected 30 minutes after placing the external magnet to allow for their capture. Bright-field and fluorescence images were collected for all the cases and the magnetic particles can be seen trapped at the tips (Figure 6.5) and base regions of the wedge structures (Figure 6.6). These experiments show that magnetic particles ranging from microns to tens of nanometers in diameter can be trapped on these substrates over a large area of arrayed nanostructures with nanometer-scale precision. This can be performed using a droplet-based method or in combination with microfluidic channels. Many applications can be foreseen including

on-chip pre-concentration, spatially controlled particle assembly, and targeted delivery of molecules toward plasmonic hot spots.

Nickel pyramids were also used for magnetic trapping and showed that it is even possible to trap a single 300 nm nanoparticle at the tip (Figure 6.5d). Interrogation of individual units of a system can provide further details about their behavior such as in-sample variation as compared to studying agglomerates. Trapping of individual particles is particularly important when combined with tip-based analytical sensing, giving us control over the number of analytes being interrogated by the sharp pyramidal tip. These experimental results demonstrate tip-based trapping of magnetic nanoparticles, indicating strongly localized and enhanced magnetic fields as expected from theory and computational modeling. The force experienced by the beads can be further increased by applying stronger external magnetic fields, using materials with stronger saturation magnetization such as Co or NiFe, fabricating even sharper tips,[144] or reducing the thickness of the top gold/silver layer.

A potential application of this technique is to improve the sensitivity of plasmonic sensors. Magnetic beads tagged with analyte molecules can be concentrated on these sharp metallic tips or bases. As the wedges and pyramid substrates are coated with gold or silver, they can be used as plasmonic sensing substrates for concurrent SPR or SERS detection. To demonstrate this, the 300 nm magnetic beads were coated with layers of silver nanoparticles.[43] These beads were then tagged with 4-mercaptopyridine (4-MP), which forms a monolayer on the silver surface via covalent thiol-metal bonds (Figure

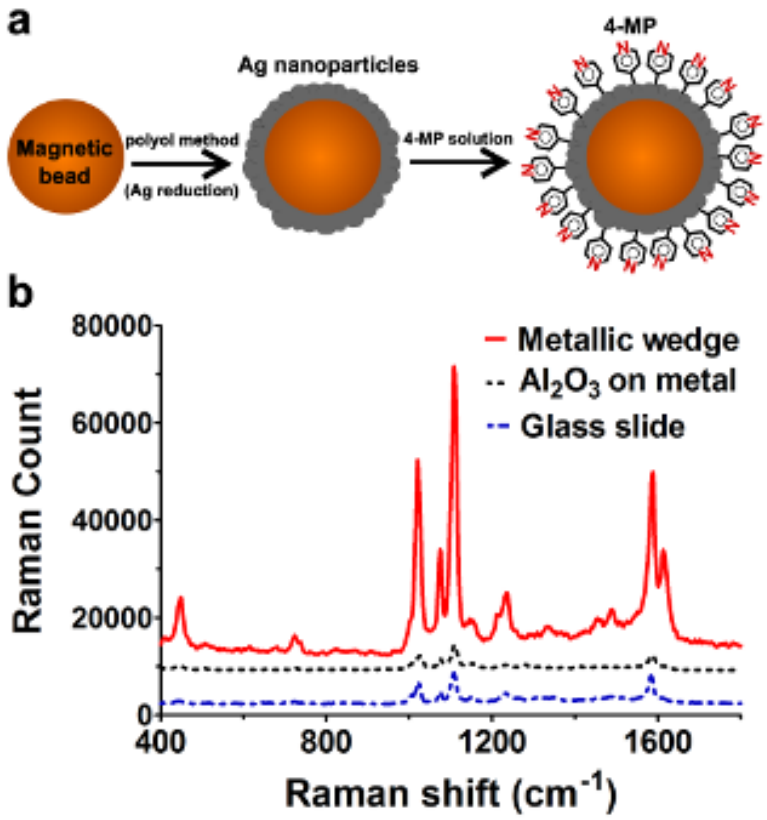

Figure 6.7: Plasmonic sensing using analyte-coated magnetic beads. (a) Cross-sectional schematic showing the chemical functionalization of magnetic beads with 4-mercaptopyrdine (4-MP) after coating them with Ag nanoparticles. (b) Raman signal obtained from the beads captured on metallic wedges as compared to on metallic wedges coated with 10 nm of Al_2O_3 and standard glass slide.

6.7a). These Ag-nanoparticle-coated beads were found to be excellent SERS substrates by themselves. The 4-MP tagged magnetic particles were trapped on three different substrates to test for any plasmonic contribution from the metal layer on top. Silver was chosen as the plasmonic metal for SERS measurements. The three substrates were a) magnetic wedges coated with a 50 nm silver shell (Ag/Ni); b) magnetic wedges with a 50 nm silver shell and 10 nm Al_2O_3 (Al_2O_3/Ag/Ni); and c) a standard glass slide. Substrates

(b) and (c) serve as negative controls for SERS as the 4-MP molecules have minimal or no interaction with the metal surface.

The results show that a higher Raman signal was obtained from the beads trapped on the silver-coated nickel wedges as compared to those on glass slide or Al_2O_3-coated wedges (Figure 6.7b). The signal intensities obtained from glass slide and Al_2O_3-coated wedge substrates were very similar, which is expected, as there is no enhancement from the substrate. For the particles captured on silver-coated wedges, the observed enhancement could be a result of generation of hotspots, which are nanoscale regions of intense electromagnetic field, between the wedge metal layer and silver nanoparticles on the magnetic beads.[145] The observed Raman enhancement is expected to be much higher if the trapped beads were not excellent SERS substrates themselves. For further Raman applications, plasmonic nanofocusing can be utilized to launch and confine surface plasmons at the sharp tips.[127, 128, 146, 147] Furthermore, these tips can combine strong magnetic fields and plasmonic hot spots for novel applications in magnetoplasmonics.

6.4 Conclusion

In summary, large-area magnetically active plasmonic wedge and pyramid arrays have been fabricated directly onto planar substrates via template stripping and used towards tip-enhanced magnetic trapping and SERS. Simple analytical equations were derived, which allows calculation of the magnitude of enhanced magnetic fields near sharp tips. COMSOL modeling revealed a similar trend for the magnetic field distribution close to the fabricated nanostructures. Force experienced by magnetic particles during

these experiments was also analyzed, which can help design sensors with better understanding of the rate and efficiency of magnetic nanoparticle capture. Tip-enhanced magnetic trapping was shown using magnetic particles ranging from microns to tens of nanometers with nanoscale control over their localization. This directed trapping can be used for various applications including concentration, isolation and analysis of analytes,[148] as well as cells[149] and viruses.[150] Compared with electrokinetic or optical trapping methods, magnetic trapping is highly advantageous for handling biological samples as it does not suffer from restrictions based on solution transparency or conductivity and does not cause any local heating effects which may damage the samples. The fabricated substrates with periodically arranged nanostructures over a wide-area can allow multiple droplet or microfluidics based experiments on the same chip with array-like analysis. The experiments also showed that the top metal layer of gold or silver does not impede efficient trapping of magnetic nanoparticles and allows application of plasmonic sensing such as SERS. Future directions include applying these nanostructures for magnetic-field-aided optical[151] and electrochemical sensing.[152]

Chapter 7

Summary and future directions

This dissertation has focused on work done towards development of metallic nanostructure-based optical biosensing platforms, which can spontaneously direct the transport of molecules and particles towards them. These techniques enabled sensitive detection of analytes in solution, and further allowed successful integration of bioparticles with the nanostructures for their on-chip analysis. Combination of smart fluidics with biosensing substrates further minimized the operational complexities and limitations imposed on the system in the form of external appendages and power sources. In this chapter we summarize these results and look towards some future applications.

7.1 Summary

A passive-flow driven technique was introduced where nanoholes fabricated in suspended nitride membranes were able to utilize evaporation from pinned-edges of droplets to drive localized concentration of analytes. Accelerated protein-protein binding on chip was demonstrated using fluorescence and SPR-based refractive index shift. This technique also enabled directed positioning of biological particles suspended in aqueous solution on the nanostructured substrates. Nanoarrays of liposomes and organelles were assembled facilitating on-chip bioanalysis. This array-like assembly enabled measurement of the membrane properties of individual mitochondria with the ability to statistically analyze the difference between the behavior of polarized and depolarized mitochondria.

A nanoimprint lithography-based technique was developed to demonstrate improved fabrication of nanohole arrays in suspended nitride membranes with size

approximately 1 mm^2. Efficient fabrication of sensing platforms with large area is necessary for cost-effective manufacturing, sampling of larger volumes, and higher signal-to-noise for improved detection. Selective patterning of the surface allowed creation of hydrophobic and hydrophilic zones on the sensor surface, which directed the flow of water towards and through these nanohole arrays. This process allowed efficient binding of analyte molecules in solution inside and around the nanohole array regions. SERS signal obtained from these substrates was 50 times higher than substrates with diffusion-limited binding.

The potential of ultrasharp nanostructures with magnetic and plasmonic functionalities for localized trapping of particles and concurrent optical sensing was discussed. A template stripping-based technique was utilized to fabricate nanostructures with ultrasharp tips and multimetallic layers integrating magnetic and plasmonic functions. The existence of tip-enhanced magnetic fields and field gradients was demonstrated using analytical equations, computer simulations and trapping of magnetic nanoparticles. Optical sensing was also utilized for obtaining surface-enhanced Raman signature of analytes-tagged to magnetic nanoparticles.

The platforms discussed in this dissertation can be used by adding a drop of solution to the nanostructured substrate or in combination with microfluidic channels. The ability to use droplet-based sensing techniques is important towards development of portable sensors that can be used in low-resource settings. Further advances in miniaturization and on-chip integration of detectors are needed to achieve complete

portability. The presented techniques have also attempted to overcome other limitations such as heating and solution conductance requirements, which can affect concentration techniques driven by electric bias.

7.2 Future work

The application of plasmonic nanostructured substrates for label-free analysis of lipid membrane reorganization is one of the important future goals. Multicomponent lipid bilayers act as model cell membranes and undergo membrane reorganization into domains spontaneously and also as a function of nanostructure geometry and surface roughness.[153, 154] This behavior of model membranes can be used to improve our understanding of reorganization in real cell membranes with implications towards membrane protein distribution and cellular signaling. We intend to form lipid bilayers over these nanostructures and use plasmonic techniques including SERS and SPR to identify the changes in local composition with time. These changes will be studied with respect to initial composition of the lipid bilayers as well as a function of nanostructure geometry. Since these detection techniques are not dependent on labeling of lipid molecules with fluorescent tags, the chances of label-induced artifacts in lipid mobility is eliminated.

During initial efforts, Raman signal was obtained from liposomes suspended in solution (Figure 7.1). The liposomes used in this experiment constituted of 95% DOPC (1,2-Dioleoyl-sn-glycero-3-phosphocholine) and 5% DNP-PE (1,2-dipalmitoyl-*sn*-glycero-3-phosphoethanolamine-N-(2,4-dinitrophenyl)). Moving further, Raman signal

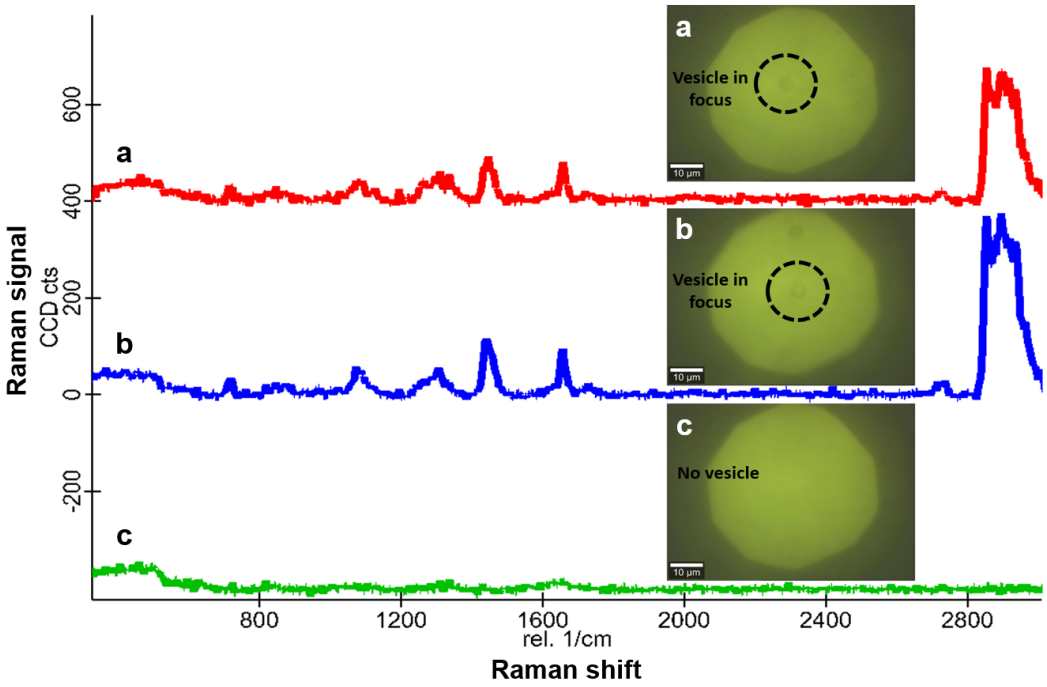

Figure 7.1: Raman signal obtained from liposomes suspended in aqueous media. (a, b) Liposome is visible in the focal volume. Recorded Raman signals have been shown. (c) Beam is focused on a region with no liposomes. Raman peaks are no longer observed.

will be collected from liposomes with varying composition to record the signal contribution from each constituent. Then these liposomes will be added to silica-coated metallic nanostructured substrates, where they can rupture and form a mobile lipid bilayer.[155] The major challenge for obtaining SERS signal from these lipids is forming a bilayer close to the metal surface. Since electromagnetic field intensity drops exponentially away from the metal surface, proximity of the bilayer to the metallic hotspots is needed for optimum Raman enhancement. Efforts are ongoing to facilitate liposome rupture directly on metal or very thin (< 2 nm) silica surfaces to improve the measurements.

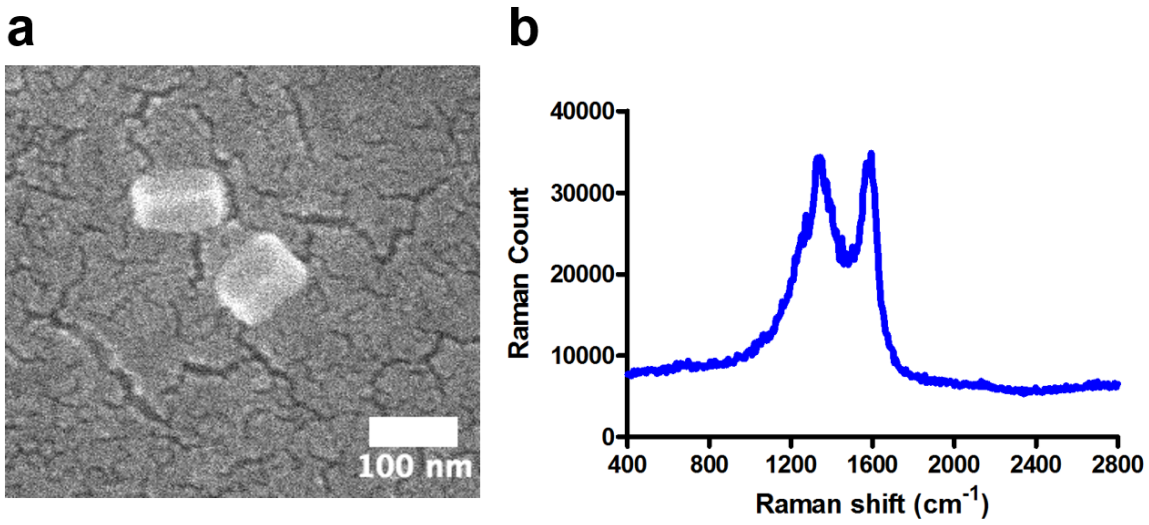

Figure 7.2: SERS signal obtained from virus-like particles (a) SEM showing two virus-like particles (VLPs). VP1 protein from SV40 viruses undergo self-assembly to form the outer capsid of the virus, used here as a virus-like particle. (b) SERS signal obtained from VLPs captured on silver-coated nanohole arrays.

Another important aim is to utilize these substrates for trapping and specific detection of bioparticles such as viruses. The ability of these nanostructures for trapping and study of single particles has already been discussed in previous chapters. Moving forward the performance of these platforms for SERS or SPR-based specific detection for on-chip diagnostics will be examined. SERS can be used to detect viruses by distinguishing between their vibrational spectra. The variation in Raman signature of different viruses has previously been reported, which can be used for their identification.[156] Some preliminary results obtained in this direction have been shown in Figure 7.2. Virus-like particles (VLPs), which consist of the outer capsid of viruses but lack the genome, were assembled. Self-assembly of a structural protein from SV40 viruses, called VP1, was utilized to form the VLPs. These particles were captured on

nanoholes and SERS signal was obtained. For SPR-based specific detection, the substrates will be functionalized with a monolayer of receptors for the target virus particles. Directed flow on the nanostructured chips should facilitate highly sensitive detection. The long-term goal is rapid on-chip identification and subtyping of viruses, which can have significant impacts towards the detection and management of virus-born communicable diseases such as influenza.

These devices further have the potential for non-plasmonic applications, including electrochemical sensing. The metal layer on these devices can be easily used as electrodes for electrochemical measurements using techniques such as cyclic voltammetry or impedance spectroscopy. Infact nanoholes fabricated in metallic films have been used as electrochemical sensors in the past.[157] With the advancements shown in this dissertation, further improvements in device performance can be expected. Confined volume of nanoholes can improve the ability to detect molecules at low concentrations, facilitating repeated collisions of the molecules with the electrode surface where they are oxidized or reduced. Flow of solution through nanoscale channels can also be used for size-based separation of suspended particles. Nanoholes can act as filters limiting the size of molecules or particles travelling through them. Applications towards filtration and specific detection of small molecules in complex solutions can be foreseen.

To conclude, the novel techniques presented in this dissertation can significantly contribute towards development of nanostructure-based platforms for sensitive on-chip molecular sensing and bioparticle analysis.

Bibliography

1. Bangs, L., New developments in particle-based immunoassays: Introduction. *Pure and Applied Chemistry* **1996,** 68, (10), 1873.
2. Keith, M.; Prior, M. E.; Richards, I. Diagnosis of pregnancy. 1997.
3. Gibb, K. A.; Yee, A. S.; Johnston, C. C.; Martin, S. D.; Nowak, R. M., Accuracy and usefulness of a breath alcohol analyzer. *Annals of Emergency Medicine* **1984,** 13, (7), 516.
4. Wang, J., Electrochemical glucose biosensors. *Chemical Reviews* **2008,** 108, (2), 814.
5. Howorka, S.; Cheley, S.; Bayley, H., Sequence-specific detection of individual DNA strands using engineered nanopores. *Nature Biotechnology* **2001,** 19, (7), 636.
6. Wittenberg, N. J.; Im, H.; Xu, X.; Wootla, B.; Watzlawik, J.; Warrington, A. E.; Rodriguez, M.; Oh, S.-H., High-Affinity Binding of Remyelinating Natural Autoantibodies to Myelin-Mimicking Lipid Bilayers Revealed by Nanohole Surface Plasmon Resonance. *Analytical Chemistry* **2012,** 84, (14), 6031.
7. Sheehan, P.; Whitman, L., Detection limits for nanoscale biosensors. *Nano Letters* **2005,** 5, (4), 803.
8. Eftekhari, F.; Escobedo, C.; Ferreira, J.; Duan, X.; Girotto, E. M.; Brolo, A. G.; Gordon, R.; Sinton, D., Nanoholes As Nanochannels: Flow-through Plasmonic Sensing. *Analytical Chemistry* **2009,** 81, (11), 4308.

9. Escobedo, C.; Brolo, A. G.; Gordon, R.; Sinton, D., Optofluidic concentration: plasmonic nanostructure as concentrator and sensor. *Nano Letters* **2012,** 12, (3), 1592.

10. Lim, J. Y.; Donahue, H. J., Cell sensing and response to micro- and nanostructured surfaces produced by chemical and topographic patterning. *Tissue Engineering* **2007,** 13, (8), 1879.

11. Ritchie, R. H., Plasma Losses by Fast Electrons in Thin Films. *Physical Review* **1957,** 106, (5), 874.

12. Barnes, W. L.; Dereux, A.; Ebbesen, T. W., Surface plasmon subwavelength optics. *Nature* **2003,** 424, (6950), 824.

13. Kretschmann, E., Die Bestimmung optischer Konstanten von Metallen Die Bestimmung optischer Konstanten von Metallen durch Anregung von Oberfliichenplasmaschwingungen. *Zeitschrift für Physik* **1971**, 241, (4), 313.

14. Fivash, M.; Towler, E. M.; Fisher, R. J., BIAcore for macromolecular interaction. *Current Opinion in Biotechnology* **1998,** 9, (1), 97.

15. Ebbesen, T. W.; Lezec, H. J.; Ghaemi, H. F.; Thio, T.; Wolff, P. A., Extraordinary optical transmission through sub-wavelength hole arrays. *Nature* **1998,** 391, (6668), 667.

16. Barnes, W. L.; Murray, W. A.; Dintinger, J.; Devaux, E.; Ebbesen, T. W., Surface plasmon polaritons and their role in the enhanced transmission of light through periodic arrays of subwavelength holes in a metal film. *Physical Review Letters* **2004,** 92, (10), 107401.

17. Gao, H. W.; Henzie, J.; Odom, T. W., Direct evidence for surface plasmon-mediated enhanced light transmission through metallic nanohole arrays. *Nano Letters* **2006,** 6, (9), 2104.

18. Jain, P.; Huang, X.; El-Sayed, I.; El-Sayad, M., Review of some interesting surface plasmon resonance-enhanced properties of noble metal nanoparticles and their applications to biosystems. *Plasmonics* **2007**, 2, (3), 107.

19. Homola, J.; Yee, S. S.; Gauglitz, G., Surface plasmon resonance sensors: review. *Sensors and Actuators B-Chemical* **1999,** 54, (1), 3.

20. McFarland, A. D.; Van Duyne, R. P., Single silver nanoparticles as real-time optical sensors with zeptomole sensitivity. *Nano Letters* **2003,** 3, (8), 1057.

21. Raman, C. V.; Krishnan, K. S., A new type of secondary radiation. *Nature* **1928,** 121, (3048), 501.

22. Fleischmann, M.; Hendra, P. J.; McQuillan, A.J.; Raman spectra of pyridine adsorbed at a silver electrode. *Chemical Physics Letters* **1974,** 26, (2), 163.

23. Jeanmaire, D. L.; Van Duyne, R. P., Surface raman spectroelectrochemistry: Part I. Heterocyclic, aromatic, and aliphatic amines adsorbed on the anodized silver electrode. *Journal of Electroanalytical Chemistry* **1977,** 84, (1), 1.

24. Albrecht, M. G.; Creighton, J. A., Anomalously intense Raman spectra of pyridine at a silver electrode. *Journal of the American Chemical Society* **1977,** 99, (15), 5215.

25. Lombardi, J. R.; Birke, R. L.; Lu, T. H.; Xu, J., Charge-transfer theory of surface-

enhanced Raman spectroscopy - Herzberg-Teller contributions. *Journal of Chemical Physics* **1986,** 84, (8), 4174.

26. McCreery; L., R., *Raman Spectroscopy for Chemical Analysis*. Wiley-Interscience: New York, **2000**.

27. Nie, S. M.; Emery, S. R., Probing single molecules and single nanoparticles by surface-enhanced Raman scattering. *Science* **1997,** 275, (5303), 1102.

28. Bantz, K. C.; Meyer, A. F.; Wittenberg, N. J.; Im, H.; Kurtulus, O.; Lee, S. H.; Lindquist, N. C.; Oh, S.-H.; Haynes, C. L., Recent progress in SERS biosensing. *Physical Chemistry Chemical Physics* **2011,** 13, (24), 11551.

29. Van Duyne, R. P.; Hulteen, J. C.; Treichel, D. A., Atomic force microscopy and surface-enhanced Raman spectroscopy .1. Ag island films and Ag film over polymer nanosphere surfaces supported on glass. *Journal of Chemical Physics* **1993,** 99, (3), 2101.

30. Hao, E.; Schatz, G. C., Electromagnetic fields around silver nanoparticles and dimers. *Journal of Chemical Physics* **2004,** 120, (1), 357.

31. Pettinger, B., Tip-enhanced Raman spectroscopy (TERS). *Surface-Enhanced Raman Scattering: Physics and Applications*. Springer Berlin, Heidelberg **2006,** 217.

32. Im, H.; Bantz, K. C.; Lindquist, N. C.; Haynes, C. L.; Oh, S.-H., Vertically Oriented Sub-10-nm Plasmonic Nanogap Arrays. *Nano Letters* **2010,** 10, (6), 2231.

33. Brolo, A. G.; Arctander, E.; Gordon, R.; Leathem, B.; Kavanagh, K. L., Nanohole-enhanced Raman scattering. *Nano Letters* **2004,** 4, (10), 2015.

34. Yonzon, C. R.; Haynes, C. L.; Zhang, X. Y.; Walsh, J. T.; Van Duyne, R. P., A glucose biosensor based on surface-enhanced Raman scattering: Improved partition layer, temporal stability, reversibility, and resistance to serum protein interference. *Analytical Chemistry* **2004,** 76, (1), 78.

35. Tian, L.; Morrissey, J. J.; Kattumenu, R.; Gandra, N.; Kharasch, E. D.; Singamaneni, S., Bioplasmonic paper as a platform for detection of kidney cancer biomarkers. *Analytical Chemistry* **2012,** 84, (22), 9928.

36. Squires, T.; Messinger, R.; Manalis, S., Making it stick: convection, reaction and diffusion in surface-based biosensors. *Nature Biotechnology* **2008,** 26, (4), 417.

37. Yanik, A. A.; Huang, M.; Artar, A.; Chang, T. Y.; Altug, H., Integrated nanoplasmonic-nanofluidic biosensors with targeted delivery of analytes. *Applied Physics Letters* **2010,** 96, (2), 021101.

38. Wang, Y.; Stevens, A.; Han, J., Million-fold preconcentration of proteins and peptides by nanofluidic filter. *Analytical Chemistry* **2005,** 77, (14), 4293.

39. Wang, Y.; Han, J., Pre-binding dynamic range and sensitivity enhancement for immuno-sensors using nanofluidic preconcentrator. *Lab on a Chip* **2008,** 8, (3), 392.

40. Barik, A.; Otto, L. M.; Yoo, D.; Jose, J.; Johnson, T. W.; Oh, S.-H., Dielectrophoresis-enhanced plasmonic sensing with gold nanohole arrays. *Nano Letters* **2014,** 14, (4), 2006.

41. Ruan, C.; Wang, H.; Li, Y., A bienzyme electrochemical biosensor coupled with immunomagnetic separation for rapid detection of Escherichia coli O15 : H7 in food samples. *Transactions of the ASAE* **2002**, 45, (1), 249.

42. Pamme, N.; Wilhelm, C., Continuous sorting of magnetic cells via on-chip free-flow magnetophoresis. *Lab on a Chip* **2006,** 6, (8), 974-80.

43. Jun, B. H.; Noh, M. S.; Kim, G.; Kang, H.; Kim, J. H.; Chung, W. J.; Kim, M. S.; Kim, Y. K.; Cho, M. H.; Jeong, D. H.; Lee, Y. S., Protein separation and identification using magnetic beads encoded with surface-enhanced Raman spectroscopy. *Analytical Biochemistry* **2009,** 391, (1), 24-30.

44. Ashkin, A.; Dziedzic, J. M.; Yamane, T., Optical trapping and manipulation of single cells using infrared-laser beams. *Nature* **1987,** 330, (6150), 769.

45. Yang, A. H. J.; Moore, S. D.; Schmidt, B. S.; Klug, M.; Lipson, M.; Erickson, D., Optical manipulation of nanoparticles and biomolecules in sub-wavelength slot waveguides. *Nature* **2009,** 457, (7225), 71.

46. Schena, M.; Shalon, D.; Davis, R. W.; Brown, P. O., Quantitative monitoring of gene expression patterns with a complementary DNA microarray. *Science* **1995,** 270, (5235), 467.

47. MacBeath, G.; Schreiber, S. L., Printing proteins as microarrays for high-throughput function determination. *Science* **2000,** 289, (5485), 1760.

48. Blixt, O.; Head, S.; Mondala, T.; Scanlan, C.; Huflejt, M. E.; Alvarez, R.; Bryan, M. C.; Fazio, F.; Calarese, D.; Stevens, J.; Razi, N.; Stevens, D. J.; Skehel, J. J.; van Die, I.; Burton, D. R.; Wilson, I. A.; Cummings, R.; Bovin, N.; Wong, C. H.;

Paulson, J. C., Printed covalent glycan array for ligand profiling of diverse glycan binding proteins. *Proceedings of the National Academdy of Science U S A* **2004,** 101, (49), 17033.

49. Yamamura, S.; Kishi, H.; Tokimitsu, Y.; Kondo, S.; Honda, R.; Rao, S.; Omori, M.; Tamiya, E.; Muraguchi, A., Single-cell microarray for analyzing cellular response. *Analytical Chemistry* **2005,** 77, (24), 8050.

50. Papp, K.; Szittner, Z.; Prechl, J., Life on a microarray: assessing live cell functions in a microarray format. *Cellular and Molecular Life Sciences* **2012,** 69, (16), 2717.

51. Bruckbauer, A.; Zhou, D.; Kang, D.; Korchev, Y.; Abell, C.; Klenerman, D., An addressable antibody nanoarray produced on a nanostructured surface. *Journal of the American Chemical Society* **2004,** 126, (21), 6508.

52. Sinensky, A.; Belcher, A., Label-free and high-resolution protein/DNA nanoarray analysis using Kelvin probe force microscopy. *Nature Nanotechnology* **2007,** 2, (10), 653.

53. Lee, B.; Lee, H.; Kim, P.; Suh, K.; Kawai, T., Nanoarrays of tethered lipid bilayer rafts on poly(vinyl alcohol) hydrogels. *Lab on a Chip* **2009,** 9, (1), 132.

54. Lee, K. B.; Park, S. J.; Mirkin, C. A.; Smith, J. C.; Mrksich, M., Protein nanoarrays generated by dip-pen nanolithography. *Science* **2002,** 295, (5560), 1702.

55. Wittenberg, N. J.; Im, H.; Johnson, T. W.; Xu, X.; Warrington, A. E.; Rodriguez, M.; Oh, S. H., Facile assembly of micro- and nanoarrays for sensing with natural

cell membranes. *ACS Nano* **2011,** 5, (9), 7555.

56. Zhang, J.; Atay, T.; Nurmikko, A. V., Optical detection of brain cell activity using plasmonic gold nanoparticles. *Nano Letters* **2009,** 9, (2), 519.

57. Cooper, M., Optical biosensors in drug discovery. *Nature Reviews Drug Discovery* **2002,** 1, 515.

58. Danelon, C.; Perez, J.; Santschi, C.; Brugger, J.; Vogel, H., Cell membranes suspended across nanoaperture arrays. *Langmuir* **2006,** 22, (1), 22.

59. Im, H.; Shao, H.; Park, Y. I.; Peterson, V. M.; Castro, C. M.; Weissleder, R.; Lee, H., Label-free detection and molecular profiling of exosomes with a nano-plasmonic sensor. *Nature Biotechnology* **2014,** 32, (5), 490.

60. Yanik, A. A.; Huang, M.; Kamohara, O.; Artar, A.; Geisbert, T. W.; Connor, J. H.; Altug, H., An Optofluidic Nanoplasmonic Biosensor for Direct Detection of Live Viruses from Biological Media. *Nano Letters* **2010,** 10, (12), 4962.

61. Junesch, J.; Emilsson, G.; Xiong, K.; Kumar, S.; Sannomiya, T.; Pace, H.; Vörös, J.; Oh, S. H.; Bally, M.; Dahlin, A. B., Location-specific nanoplasmonic sensing of biomolecular binding to lipid membranes with negative curvature. *Nanoscale* **2015,** 7, (37), 15080.

62. Hatefi, Y., The mitochondrial electron transport and oxidative phosphorylation system. *Annual Review of Biochemistry* **1985,** 54, 1015.

63. Newmeyer, D. D.; Ferguson-Miller, S., Mitochondria: releasing power for life and unleashing the machineries of death. *Cell* **2003,** 112, (4), 481.

64. Balaban, R. S.; Nemoto, S.; Finkel, T., Mitochondria, oxidants, and aging. *Cell* **2005,** 120, (4), 483.

65. Fulda, S.; Galluzzi, L.; Kroemer, G., Targeting mitochondria for cancer therapy. *Nature Reviews Drug Discovery* **2010,** 9, (6), 447.

66. Wasylycia, J.; Sapelnikova, S.; Jeong, H.; Dragoljic, J.; Marcus, S.; Harrison, D., Nano-biopower supplies for biomolecular motors: the use of metabolic pathway-based fuel generating systems in microfluidic devices. *Lab on a Chip* **2008,** 8, (6), 979.

67. Nakayama, S.; Sakuyama, T.; Mitaku, S.; Ohta, Y., Fluorescence imaging of metabolic responses in single mitochondria. *Biochemical and Biophysical Research Communications* **2002,** 290, (1), 23.

68. Quarato, G.; Piccoli, C.; Scrima, R.; Capitanio, N., Functional imaging of membrane potential at the single mitochondrion level: possible application for diagnosis of human diseases. *Mitochondrion* **2011,** 11, (5), 764.

69. Johnson, R.; Navratil, M.; Poe, B.; Xiong, G.; Olson, K.; Ahmadzadeh, H.; Andreyev, D.; Duffy, C.; Arriaga, E., Analysis of mitochondria isolated from single cells. *Analytical and Bioanalytical Chemistry* **2007,** 387, (1), 107.

70. Wolken, G. G.; Kostal, V.; Arriaga, E. A., Capillary isoelectric focusing of individual mitochondria. *Analytical Chemistry* **2011,** 83, (2), 612.

71. Lim, T. S.; Davila, A.; Zand, K.; Wallace, D. C.; Burke, P. J., Wafer-scale mitochondrial membrane potential assays. *Lab on a Chip* **2012,** 12, (15), 2719.

72. Zand, K.; Pham, T.; Davila, A.; Wallace, D. C.; Burke, P. J., Nanofluidic platform for single mitochondria analysis using fluorescence microscopy. *Analytical Chemistry* **2013,** 85, (12), 6018.

73. Luo, J.; Abdallah, B. G.; Wolken, G. G.; Arriaga, E. A.; Ros, A., Insulator-based dielectrophoresis of mitochondria. *Biomicrofluidics* **2014,** 8, (2), 021801.

74. Suraniti, E.; Vajrala, V. S.; Goudeau, B.; Bottari, S. P.; Rigoulet, M.; Devin, A.; Sojic, N.; Arbault, S., Monitoring metabolic responses of single mitochondria within poly(dimethylsiloxane) wells: study of their endogenous reduced nicotinamide adenine dinucleotide evolution. *Analytical Chemistry* **2013,** 85, (10), 5146.

75. Vajrala, V. S.; Suraniti, E.; Garrigue, P.; Goudeau, B.; Rigoulet, M.; Devin, A.; Sojic, N.; Arbault, S., Optical microwell array for large scale studies of single mitochondria metabolic responses. *Analytical and Bioanalytical Chemistry* **2014,** 406, (4), 931.

76. Brolo, A. G.; Gordon, R.; Leathem, B.; Kavanagh, K. L., Surface plasmon sensor based on the enhanced light transmission through arrays of nanoholes in gold films. *Langmuir* **2004,** 20, (12), 4813.

77. Brolo, A. G.; Kwok, S. C.; Moffitt, M. G.; Gordon, R.; Riordon, J.; Kavanagh, K. L., Enhanced fluorescence from arrays of nanoholes in a gold film. *Journal of the American Chemical Society* **2005,** 127, (42), 14936.

78. Levene, M.; Korlach, J.; Turner, S.; Foquet, M.; Craighead, H.; Webb, W., Zero-mode waveguides for single-molecule analysis at high concentrations. *Science* **2003,** 299, (5607), 682.

79. Jackman, J. A.; Linardy, E.; Yoo, D.; Seo, J.; Ng, W. B.; Klemme, D. J.; Wittenberg, N. J.; Oh, S.-H.; Cho, N. J., Plasmonic Nanohole Sensor for Capturing Single Virus-Like Particles toward Virucidal Drug Evaluation. *Small* **2015**, published online, DOI: 10.1002/smll.201501914.

80. Kumar, S.; Wittenberg, N. J.; Oh, S.-H., Nanopore-Induced Spontaneous Concentration for Optofluidic Sensing and Particle Assembly. *Analytical Chemistry* **2012,** 85, (2), 971.

81. Kumar, S.; Cherukulappurath, S.; Johnson, T. W.; Oh, S.-H., Millimeter-sized Suspended Plasmonic Nanohole Arrays for Surface-Tension-Driven Flow-through SERS. *Chemistry of Materials* **2014,** 26, (22), 6523.

82. Wolken, G.; Arriaga, E., Simultaneous Measurement of Individual Mitochondrial Membrane Potential and Electrophoretic Mobility by Capillary Electrophoresis. *Analytical Chemistry* **2014,** 86, (9), 4217.

83. Kostal, V.; Arriaga, E. A., Capillary electrophoretic analysis reveals subcellular binding between individual mitochondria and cytoskeleton. *Analytical Chemistry* **2011,** 83, (5), 1822.

84. Edelstein, A.; Amodaj, N.; Hoover, K.; Vale, R.; Stuurman, N., Computer control of microscopes using μManager. *Current Protocols in Molecular Biology* **2010,** Chapter 14, Unit14.20.

85. Schneider, C.; Rasband, W.; Eliceiri, K., NIH Image to ImageJ: 25 years of image analysis. *Nature Methods* **2012,** 9, (7), 671.

86. Deegan, R.; Bakajin, O.; Dupont, T.; Huber, G.; Nagel, S.; Witten, T., Capillary flow as the cause of ring stains from dried liquid drops. *Nature* **1997,** 389, (6653), 827.

87. Brand, M.; Nicholls, D., Assessing mitochondrial dysfunction in cells. *Biochemical Journal* **2011,** 435, 297.

88. Moore, C.; Pressman, B. C., Mechanism of action of valinomycin on mitochondria. *Biochemical and Biophysical Research Communications* **1964,** 15, (6), 562.

89. Smiley, S. T.; Reers, M.; Mottola-Hartshorn, C.; Lin, M.; Chen, A.; Smith, T. W.; Steele, G. D.; Chen, L. B., Intracellular heterogeneity in mitochondrial membrane potentials revealed by a J-aggregate-forming lipophilic cation JC-1. *Proceedings of Natural Academy of Science U S A* **1991,** 88, (9), 3671.

90. Lindquist, N. C.; Lesuffleur, A.; Im, H.; Oh, S. H., Sub-micron resolution surface plasmon resonance imaging enabled by nanohole arrays with surrounding Bragg mirrors for enhanced sensitivity and isolation. *Lab on a Chip* **2009,** 9, (3), 382.

91. Dahlin, A. B.; Sannomiya, T.; Zahn, R.; Sotiriou, G. A.; Vörös, J., Electrochemical crystallization of plasmonic nanostructures. *Nano Letters* **2011,** 11, (3), 1337.

92. Psaltis, D.; Quake, S.; Yang, C., Developing optofluidic technology through the fusion of microfluidics and optics. *Nature* **2006,** 442, (7101), 381.

93. Monat, C.; Domachuk, P.; Eggleton, B., Integrated optofluidics: A new river of light. *Nature Photonics* **2007,** 1, (2), 106.

94. Erickson, D.; Sinton, D.; Psaltis, D., Optofluidics for energy applications. *Nature Photonics* **2011,** 5, (10), 583.

95. Fan, X.; White, I., Optofluidic microsystems for chemical and biological analysis. *Nature Photonics* **2011,** 5, (10), 591.

96. Fleischmann, M.; Hendra, P. J.; McQuillan, A. J., Raman-spectra of pyridine adsorbed at a silver electrode. *Chemical Physics Letter* **1974,** 26, 163.

97. Ko, H.; Singamaneni, S.; Tsukruk, V. V., Nanostructured surfaces and assemblies as SERS media. *Small* **2008,** 4, (10), 1576.

98. Gordon, R.; Sinton, D.; Kavanagh, K. L.; Brolo, A. G., A new generation of sensors based on extraordinary optical transmission. *Accounts of Chemical Research* **2008,** 41, (8), 1049.

99. Coe, J. V.; Heer, J. M.; Teeters-Kennedy, S.; Tian, H.; Rodriguez, K. R., Extraordinary transmission of metal films with arrays of subwavelength holes. *Annual Review of Physical Chemistry* **2008,** 59, 179.

100. Garcia-Vidal, F. J.; Martin-Moreno, L.; Ebbesen, T. W.; Kuipers, L., Light passing through subwavelength apertures. *Reviews of Modern Physics* **2010,** 82, (1), 729.

101. Lesuffleur, A.; Im, H.; Lindquist, N.; Oh, S.-H., Periodic nanohole arrays with shape-enhanced plasmon resonance as real-time biosensors. *Applied Physics Letters* **2007**, 90, (24), 243110.

102. Sinton, D.; Gordon, R.; Brolo, A., Nanohole arrays in metal films as optofluidic elements: progress and potential. *Microfluidics and Nanofluidics* **2008,** 4, (1-2), 107.

103. Im, H.; Wittenberg, N.; Lesuffleur, A.; Lindquist, N.; Oh, S., Membrane protein biosensing with plasmonic nanopore arrays and pore-spanning lipid membranes. *Chemical Science* **2010,** 1, (6), 688.

104. Yu, Q. M.; Guan, P.; Qin, D.; Golden, G.; Wallace, P. M., Inverted size-dependence of surface-enhanced Raman scattering on gold nanohole and nanodisk arrays. *Nano Letters* **2008,** 8, (7), 1923.

105. Lee, S.; Bantz, K.; Lindquist, N.; Oh, S.; Haynes, C., Self-Assembled Plasmonic Nanohole Arrays. *Langmuir* **2009**, 25, (23), 13685.

106. Yu, Q.; Braswell, S.; Christin, B.; Xu, J.; Wallace, P.; Gong, H.; Kaminsky, D., Surface-enhanced Raman scattering on gold quasi-3D nanostructure and 2D nanohole arrays. *Nanotechnology* **2010,** 21, (35), 355301.

107. Jonsson, M. P.; Dahlin, A. B.; Feuz, L.; Petronis, S.; Höök, F., Locally Functionalized Short-Range Ordered Nanoplasmonic Pores for Bioanalytical Sensing. *Analytical Chemistry* **2010,** 82, (5), 2087.

108. Chou, S. Y.; Krauss, P. R.; Renstrom, P. J., Imprint of sub-25 nm vias and trenches in polymers. *Applied Physics Letters* **1995,** 67, (21), 3114.

109. Guo, L. J., Nanoimprint lithography: Methods and material requirements. *Advanced Materials* **2007,** 19, (4), 495.

110. Im, H.; Lee, S. H.; Wittenberg, N. J.; Johnson, T. W.; Lindquist, N. C.; Nagpal, P.; Norris, D. J.; Oh, S.-H., Template-stripped smooth Ag nanohole arrays with silica shells for surface plasmon resonance biosensing. *ACS Nano* **2011,** 5, (8), 6244.

111. Nabar, B.; Celik-Butler, Z.; Dennis, B.; Billo, R., A nanoporous silicon nitride membrane using a two-step lift-off pattern transfer with thermal nanoimprint lithography. *Journal of Micromechanics and Microengineering* **2012,** 22, (4), 045012.

112. Bantz, K. C.; Haynes, C. L., Surface-Enahnced Raman Scattering Substrates Fabricated using Electroless Plating on Polymer-Templated Nanostructures. *Langmuir* **2008,** 24, (11), 5862.

113. Wan, L. J.; Terashima, M.; Noda, H.; Osawa, M., Molecular orientation and ordered structure of benzenethiol adsorbed on gold(111). *Journal of Physical Chemistry B* **2000,** 104, (15), 3563.

114. Smythe, E. J.; Dickey, M. D.; Bao, J.; Whitesides, G. M.; Capasso, F., Optical antenna arrays on a fiber facet for in situ surface-enhanced Raman scattering detection. *Nano Letters* **2009,** 9, (3), 1132.

115. McFarland, A. D.; Young, M. A.; Dieringer, J. A.; Van Duyne, R. P., Wavelength-scanned surface-enhanced Raman excitation spectroscopy. *Journal of Physical Chemistry B* **2005,** 109, (22), 11279.

116. Shafer-Peltier, K.; Haynes, C.; Glucksberg, M.; Van Duyne, R., Toward a glucose

biosensor based on surface-enhanced Raman scattering. *Journal of the American Chemical Society* **2003,** 125, (2), 588.

117. Krishnan, A.; Thio, T.; Kima, T. J.; Lezec, H. J.; Ebbesen, T. W.; Wolff, P. A.; Pendry, J.; Martin-Moreno, L.; Garcia-Vidal, F. J., Evanescently coupled resonance in surface plasmon enhanced transmission. *Optics Communications* **2001,** 200, (1-6), 1.

118. Bryant, M.; Joa, S.; Pemberton, J., Raman-scattering from monolayer films of Thiophenol and 4-Mercaptopyridine at Pt surfaces. *Langmuir* **1992,** 8, (3), 753.

119. Saboktakin, M.; Ye, X.; Chettiar, U.; Engheta, N.; Murray, C.; Kagan, C., Plasmonic Enhancement of Nanophosphor Upconversion Luminescence in Au Nanohole Arrays. *ACS Nano* **2013,** 7, (8), 7186.

120. Guo, P.; Hall, E.; Schirhagl, R.; Mukaibo, H.; Martin, C.; Zare, R., Microfluidic capture and release of bacteria in a conical nanopore array. *Lab on a Chip* **2012,** 12, (3), 558.

121. Hennesthal, C.; Steinem, C., Pore-spanning lipid bilayers visualized by scanning force microscopy. *Journal of the American Chemical Society* **2000,** 122, (33), 8085.

122. Dahlin, A.; Zäch, M.; Rindzevicius, T.; Käll, M.; Sutherland, D. S.; Höök, F., Localized surface plasmon resonance sensing of lipid-membrane-mediated biorecognition events. *Journal of the American Chemical Society* **2005,** 127, (14), 5043.

123. Tiefenauer, L.; Studer, A., Nano for bio: Nanopore arrays for stable and functional lipid bilayer membranes (Mini Review). *Biointerphases* **2008,** 3, (2), FA74.

124. Maier, S. A., *Plasmonics: fundamentals and applications*. Springer Science and Buisness Media, 2007.

125. Halas, N. J.; Lal, S.; Chang, W. S.; Link, S.; Nordlander, P., Plasmons in strongly coupled metallic nanostructures. *Chemical Reviews* **2011,** 111, (6), 3913.

126. Jackson, J. D., *Classical Electrodynamics*. Wiley: New York: 3rd ed., **1998**.

127. Stockman, M. I., Nanofocusing of optical energy in tapered plasmonic waveguides. *Physical Review Letters* **2004,** 93, (13), 137404.

128. Gramotnev, D.; Bozhevolnyi, S., Plasmonics beyond the diffraction limit. *Nature Photonics* **2010,** 4, 83.

129. Van Bladel, J., Field singularities at the tip of a cone. *Proceedings of the IEEE* **1983,** 71, (7), 901.

130. Feuz, L.; Jönsson, P.; Jonsson, M. P.; Höök, F., Improving the limit of detection of nanoscale sensors by directed binding to high-sensitivity areas. *ACS Nano* **2010,** 4, (4), 2167.

131. Kumar, S.; Wittenberg, N. J.; Oh, S.-H., Nanopore-induced spontaneous concentration for optofluidic sensing and particle assembly. *Analytical Chemistry* **2013,** 85, (2), 971.

132. Kumar, S.; Cherukulappurath, S.; Johnson, T. W.; Oh, S.-H., Millimeter-sized

suspended plasmonic nanohole arrays for surface-tension-driven flow-through SERS. *Chemistry of Materials* **2014,** 26, (22), 6523.

133. Barik, A.; Otto, L. M.; Yoo, D.; Jose, J.; Johnson, T. W.; Oh, S.-H., Dielectrophoresis-enhanced plasmonic sensing with gold nanohole arrays. *Nano Letters* **2014,** 14, (4), 2006.

134. Soelberg, S. D.; Stevens, R. C.; Limaye, A. P.; Furlong, C. E., Surface plasmon resonance detection using antibody-linked magnetic nanoparticles for analyte capture, purification, concentration, and signal amplification. *Analytical Chemistry* **2009,** 81, (6), 2357.

135. Deng, T.; Prentiss, M.; Whitesides, G., Fabrication of magnetic microfiltration systems using soft lithography. *Applied Physics Letters* **2002,** 80, (3), 461.

136. Lou, X.; Qian, J.; Xiao, Y.; Viel, L.; Gerdon, A. E.; Lagally, E. T.; Atzberger, P.; Tarasow, T. M.; Heeger, A. J.; Soh, H. T., Micromagnetic selection of aptamers in microfluidic channels. *Proceedings of Natural Academy of Science U S A* **2009,** 106, (9), 2989.

137. Futamoto, M.; Hagami, T.; Ishihara, S.; Soneta, K.; Ohtake, M., Improvement of magnetic force microscope resolution and application to high-density recording media. *IEEE Transactions on Magnetics* **2013,** 49, (6), 2748.

138. Henzie, J.; Kwak, E. S.; Odom, T. W., Mesoscale metallic pyramids with nanoscale tips. **2005**, 5, (7), 1199.

139. Nagpal, P.; Lindquist, N. C.; Oh, S.-H.; Norris, D. J., Ultrasmooth patterned metals for plasmonics and metamaterials. *Science* **2009,** 325, (5940), 594.

140. Johnson, T. W.; Lapin, Z. J.; Beams, R.; Lindquist, N. C.; Rodrigo, S. G.; Novotny, L.; Oh, S.-H., Highly reproducible near-field optical imaging with sub-20-nm resolution based on template-stripped gold pyramids. *ACS Nano* **2012,** 6, (10), 9168.

141. Lindquist, N.; Nagpal, P.; McPeak, K.; Norris, D.; Oh, S.-H., Engineering metallic nanostructures for plasmonics and nanophotonics. *Reports on Progress in Physics* **2012,** 75, (3), 036501.

142. Park, J. H.; Nagpal, P.; McPeak, K. M.; Lindquist, N. C.; Oh, S.-H.; Norris, D. J., Fabrication of smooth patterned structures of refractory metals, semiconductors, and oxides via template stripping. *ACS Applied Materials and Interfaces* **2013,** 5, (19), 9701.

143. Lee, J.; Hasan, W.; Lee, M.; Odom, T., Optical properties and magnetic manipulation of bimaterial nanopyramids. *Advanced Materials* **2007,** 19, (24), 4387.

144. Im, H.; Oh, S.-H., Oxidation sharpening, template stripping, and passivation of ultra-sharp metallic pyramids and wedges. *Small* **2014,** 10, (4), 680.

145. Ward, D. R.; Grady, N. K.; Levin, C. S.; Halas, N. J.; Wu, Y. P.; Nordlander, P.; Natelson, D., Electromigrated nanoscale gaps for surface-enhanced Raman spectroscopy. *Nano Letters* **2007,** 7, (5), 1396.

146. Novotny, L.; Hecht, B., *Principles of Nano-optics*. 2006.

147. Cherukulappurath, S.; Johnson, T. W.; Lindquist, N. C.; Oh, S.-H., Template-

stripped asymmetric metallic pyramids for tunable plasmonic nanofocusing. *Nano Letters* **2013,** 13, (11), 5635.

148. Grancharov, S.; Zeng, H.; Sun, S.; Wang, S.; O'Brien, S.; Murray, C.; Kirtley, J.; Held, G., Bio-functionalization of monodisperse magnetic nanoparticles and their use as biomolecular labels in a magnetic tunnel junction based sensor. *Journal of Physical Chemistry B* **2005,** 109, (26), 13030.

149. Tanase, M.; Felton, E. J.; Gray, D. S.; Hultgren, A.; Chen, C. S.; Reich, D. H., Assembly of multicellular constructs and microarrays of cells using magnetic nanowires. *Lab Chip* **2005,** 5, (6), 598.

150. Chen, G.; Alberts, C.; Rodriguez, W.; Toner, M., Concentration and purification of human immunodeficiency virus type 1 virions by microfluidic separation of superparamagnetic nanoparticles. *Analytical Chemistry* **2010,** 82, (2), 723.

151. Ye, X.; Chen, J.; Diroll, B.; Murray, C., Tunable plasmonic coupling in self-assembled binary nanocrystal super lattices studied by correlated optical microspectrophotometry and electron microscopy. *Nano Letters* **2013,** 13, (3), 1291.

152. Dahlin, A. B.; Dielacher, B.; Rajendran, P.; Sugihara, K.; Sannomiya, T.; Zenobi-Wong, M.; Vörös, J., Electrochemical plasmonic sensors. *Analytical and Bioanalytical Chemistry* **2012,** 402, (5), 1773.

153. Yoon, T.; Jeong, C.; Lee, S.; Kim, J.; Choi, M.; Kim, S.; Kim, M.; Lee, S., Topographic control of lipid-raft reconstitution in model membranes. *Nature Materials* **2006**, 5(4), 281-285.

154. Ryu, Y. S.; Lee, I. H.; Suh, J. H.; Park, S. C.; Oh, S.; Jordan, L. R.; Wittenberg, N. J.; Oh, S.-H.; Jeon, N. L.; Lee, B.; Parikh, A. N.; Lee, S. D., Reconstituting ring-rafts in bud-mimicking topography of model membranes. *Nature Communications* **2014,** 5, 4507.

155. Schonherr, H.; Johnson, J. M.; Lenz, P.; Frank, C. W.; Boxer, S. G., Vesicle adsorption and lipid bilayer formation on glass studied by atomic force microscopy. *Langmuir* **2004,** 20, (26), 11600.

156. Shanmukh, S.; Jones, L.; Driskell, J.; Zhao, Y. P.; Dluhy, R.; Tripp, R. A., Rapid and sensitive detection of respiratory virus molecular signatures using a silver nanorod array SERS substrate. *Nano Letters* **2006,** 6, (11), 2630.

157. Branagan, S. P.; Contento, N. M.; Bohn, P. W., Enhanced mass transport of electroactive species to annular nanoband electrodes embedded in nanocapillary array membranes. *Journal of the American Chemical Society* **2012,** 134, (20), 8617.

Appendix A

Fabrication of suspended nanohole arrays in silicon nitride membranes using nanoimprint lithography.

1) Deposit 200 nm low-stress silicon nitride on (100) silicon wafers using low-pressure chemical vapor deposition (LPCVD).
2) Spincoat front side of the wafer with S1818 photoresist at 3000 rpm for 30s, and bake for 1 min on the hotplate at 105 $^{\circ}$C. This resist layer protects the smooth top surface of the wafer during the following fabrication steps.
3) Repeat step 2 on the backside of the wafer using S1813 photoresist.
4) Expose the resist on the back of the wafer to ultraviolet light through a chrome-on soda-lime photomask for 7 sec in hard contact mode.
5) Bake the wafer on a hotplate (105 $^{\circ}$C) for 1 min.
6) Develop the wafer for 30 sec using 351 developer diluted 5 times with water.
7) Wash the wafer and dry it.
8) Remove residual resist for 15 sec using plasma etching: recipe name O2CLEAN in STS etcher (100 sccm of O_2 at 50 W). Remove all the nitride from exposed regions on the back of the wafer using the NIT1 recipe (40 sccm of CF_4 and 4 sccm of O_2 at 100 W) for 4 mins.
9) Strip away the photoresist washing the wafers with acetone and piranha (1:1 H_2SO_4:H_2O_2) for 10 mins each.
10) Spincoat thermal nanoimprint resist (NXR 1025) on the smooth top surface of the wafer at 3000 rpm for 30s.

11) Bake the wafer at 155 °C for 1 min.

12) Break the wafer into chips, with dimensions less than 3 inches, so that they can fit in the nanoimprinter. Chips used during the fabrication were approximately 1 inch × 1 inch in dimension.

13) Imprint nanohole array patterns into the thermal resist layer using molds (Lightsmyth Inc.) with pressure 350 psi, at 130 °C for 2 minutes (Nanoimprinter recipe name: 350_130_2).

14) Place two chips in the STS etcher at a time with nanoimprinted side facing up. Remove residual resist for 15 secs using plasma etching: STS etcher, recipe name O2CLEAN (100 sccm of O_2 at 50 W).

15) Etch nitride from exposed regions for 6 mins 30 secs using PJSOXIDE recipe on the STS etcher (50 sccm of Ar, 50 sccm of CHF3, 25 sccm of CF4 at 150 W). The number of chips in the etcher can affect the etching rate. The objective is to transfer the nanohole patterns by etching two-thirds of the way into the nitride layer, leaving sufficient nitride at the bottom of the nanoholes for protection of silicon during the subsequent KOH etching step.

16) Strip away the thermal resist washing the wafers with acetone (10 mins) and in piranha solution (1:1 H_2SO_4:H_2O_2) for 30 mins.

17) Place the chips in KOH bath at 85 °C for about 4 hours 30 mins to etch silicon from the exposed areas and obtain suspended nitride membranes.

18) Carefully clean the chips in DI water for 10 mins. These chips should be handled gently avoiding direct pressure on the freely-hanging nitride region.

19) Rinse the chips with isopropanol and dry using N_2 gun and hot plate.

20) Place the chips in STS etcher (two at a time) with the backside facing up. Remove any remaining nitride from inside the nanoimprinted nanoholes using plasma etching: STS etcher, recipe name NIT2 (40 sccm CF4 and 4 sccm O2 at 50 W) for 3 mins 30 secs.

21) Check if the holes have been fabricated well and are open on both sides of the nitride membrane using SEM imaging. Place the chips in the SEM backside facing up to identify if the holes are clearly visible. In case the holes are not visible further etching of the nitride is needed.

22) Metal and other materials can be coated as desired on the chips after they have been characterized.